# HIGH-EFFICIENCY SWITCHED-MODE MICROWAVE CIRCUITS

by

ERIC BRYERTON

M.S., University of Colorado, 1997

B.S., University of Illinois, 1995

A thesis submitted to the

Faculty of the Graduate School of the

University of Colorado in partial fulfillment

of the requirements for the degree of

Doctor of Philosophy

Department of Electrical and Computer Engineering

1999

This thesis entitled:

High-Efficiency Switched-Mode Microwave Circuits

written by Eric Bryerton

has been approved for the Department of Electrical and Computer Engineering

Zoya Popović

K. C. Gupta

Date

The final copy of this thesis has been examined by the signators, and we find that both the content and the form meet acceptable presentation standards of scholarly work in the above mentioned discipline.

Bryerton, Eric (Ph.D., Electrical Engineering)

High-Efficiency Switched-Mode Microwave Circuits

Thesis directed by Associate Professor Zoya Popović

Switched-mode techniques have been applied extensivley to rf power amplifiers. Recent rapid advances in semiconductor device technology allow these design methodologies to now be applied to microwave amplifiers. These switched-mode power amplifiers have efficiencies greater than their linear counterparts. High efficiency is important at microwave frequencies for issues of reliability, heat dissipation, and battery lifetime.

In this thesis, an overview is given of switched-mode amplifier topologies and their application to microwave frequencies. Several experimental examples are described from UHF to X-Band, including power, efficiency, linearity, and time-domain waveform measurements. The incorporation and measurement of switched-mode design into microwave oscillators and freqeuncy doublers is also described. These circuits can be effective alternatives to low-power oscillator/power amplifier or passive multiplier/power amplifier combinations.

In addition, the integration of a X-band switched-mode class-F amplifier in spatial power combining arrays is also described. Feed loss, EIRP, effective transmitter power, radiation patterns, and combining efficiency are measured. Based on these measurements, spatial power combining is shown to be an attractive alternative to circuit combining for large numbers of elements. The effectiveness of a constrained lens feed for power amplifier spatial combiners is also addressed.

DEDICATION

To Jennifer and Zoltar

# ACKNOWLEDGMENTS

The friendship, support, and guidance of many people have contributed to the presentation of this thesis. First of all, I wish to thank my parents, brothers, and sister, whose love, nurture, and guidance allowed me to get to this point. The love and support of my wife, Jennifer, made my years in graduate school the most enjoyable of my life. I truly appreciate her patience while I worked on this thesis.

Most of all, I would like to thank my thesis advisor, Professor Zoya Popović, for her support, kindness, and guidance during my studies. Not only did she provide all my needs as a researcher, but she also went out of her way to ensure that Jen and I were happy.

I would also like to thank the past and present members of the Active Antennas Research Group for their friendship and support. It was a great experience to continue and build upon the work by Tom Mader, Jon Schoenberg, Wayne Shiroma, Jon Dixon, Milica Marković, and Stein Hollung. The present group members: Joe Tustin, Todd Marshall, Michael Forman, Jim Vian, Manoja Weiss, Jan Peetersweem, and Slavko Djukić have all made the group a great place to work. Special thanks go to Manoja Weiss, for measurements and ideas contributed to this thesis, and Michael Forman, for selflessly ensuring that the computers in the lab ran efficiently. I also thank Jaap Bregman for helpful discussions while visiting our group and also for the opportunity to work in the Netherlands for a summer.

Finally, I would like to thank our administrative assistant Helen Frey, who often went out of her way to make sure my circuit components would be there on time, and that our day-to-day operations ran smoothly.

CONTENTS

CHAPTER

1 INTRODUCTION AND BACKGROUND . . . . . 1

1.1 Introduction . . . . . 1

1.2 Solid-State Device Capabilities . . . . . 2

1.3 Organization of the Thesis . . . . . 4

2 COMPARISON OF SWITCHED-MODE POWER AMPLIFIER TOPOLOGIES . . . . . 5

2.1 Introduction . . . . . 5

2.2 Switched-Mode Topologies . . . . . 5

2.2.1 Class-D . . . . . 5

2.2.2 Class-E . . . . . 7

2.2.3 Class-F . . . . . 10

2.3 Modeling of Switched-Mode Amplifiers . . . . . 12

2.4 Examples . . . . . 13

2.4.1 Definitions of Efficiency . . . . . 13

2.4.2 500-MHz Power Amplifiers . . . . . 14

2.4.3 2.5-GHz Class-E Amplifier . . . . . 15

2.4.4 8-GHz Power Amplifiers . . . . . 20

2.4.5 10-GHz Class-E Amplifier . . . . . 21

3 TIME-DOMAIN MEASUREMENTS OF SWITCHED-MODE MICROWAVE POWER AMPLIFIERS . . . . . 25

3.1 Introduction . . . . . 25

3.2 Photoconductive Sampling Technique . . . . . 26

3.3 Time-Domain Measurements . . . . . 27
3.3.1 Class-F Amplifier . . . . . 28
3.3.2 Class-E Amplifier . . . . . 31
3.4 Conclusion . . . . . 34
4 SPATIAL COMBINING OF HIGH-EFFICIENCY POWER AMPLIFIERS . . . . . 35
4.1 Introduction . . . . . 35
4.2 Methods of Power Combining . . . . . 35
4.2.1 Chip-Level Power Combining . . . . . 36
4.2.2 Circuit Level Power Combining . . . . . 37
4.2.3 Spatial Power Combining . . . . . 37
4.3 Definition of Power Combining Efficiency . . . . . 41
4.4 Feeding of Spatial Combiner . . . . . 42
4.5 X-Band Spatial Power Combiners . . . . . 44
4.5.1 Antenna Design . . . . . 44
4.5.2 Array Design . . . . . 44
4.5.3 Amplifier Repeatability . . . . . 46
4.5.4 Via Repeatability . . . . . 46
4.5.5 Passive 9-Element Array . . . . . 49
4.5.6 Active 9-Element Array . . . . . 53
4.5.7 Active 36-Element array . . . . . 58
4.6 Comparison, Analysis, and Conclusions . . . . . 63
5 CLASS-E OSCILLATORS . . . . . 66
5.1 Introduction . . . . . 66
5.2 5-GHz Microstrip Class-E Oscillator . . . . . 67
5.2.1 Amplifier Design . . . . . 68
5.2.2 Coupler Design . . . . . 68

5.2.3 Oscillator Design . . . . . 69
5.2.4 Measurements . . . . . 71
5.3 A Class-E Oscillator Array . . . . . 74
5.3.1 Feedback Design . . . . . 74
5.3.2 Measurements . . . . . 75
5.3.3 Determining Efficiency Through Heat Measurements . . 78
5.4 Conclusion . . . . . 82
6 CLASS-E MULTIPLIERS . . . . . 83
6.1 Introduction . . . . . 83
6.2 Class-E Multiplier Design . . . . . 84
6.3 1-GHz Doubler . . . . . 85
6.4 5-GHz Doubler . . . . . 88
6.5 Conclusions . . . . . 89
7 CONCLUSIONS AND FUTURE WORK . . . . . 91
7.1 Conclusions . . . . . 91
7.2 Future Work . . . . . 93
7.2.1 Ka-Band Switched-Mode Circuits . . . . . 93
7.2.2 Mutual Coupling in Antenna Arrays . . . . . 93
7.2.3 High-Efficiency Amplifiers for Digital Communications . 94
BIBLIOGRAPHY . . . . . 95

# TABLES

TABLE

4.1 Summary of measurements for the class-F power amplifier using the FLK052 and the class-E power amplifier using the four-times larger FLK202. $P_{heat}$ is the power dissipated as heat. . . . . 37

4.2 This table compares, for the same input power (8 W), chip-level combining versus circuit combining for a corporate combiner with 0.2 dB loss per stage. $\eta_{amp}$ is the overall efficiency of the amplifier, $PCE_{ckt}$ is the power-combining efficiency of the corporate network, and $\eta$ is the overall efficiency of the entire system. $P_{heat}$ is the total power dissipated as heat in the system. . . . . 38

4.3 This table compares, for the same input power (8 W), the spatial power combining of 16 FLK202 amplifiers and 64 FLK052 amplifiers. The area assumes a unit cell size of 0.8λ x 0.8λ. The directivity, D, assumes an effective area equal to the physical area. $P_{heat}$ is the total power dissipated as heat in the system. . . . . 40

4.4 Calculated feed loss of patch antenna constrained lens arrays with a F/D of 0.87 and a unitcell spacing of 0.85 λ x 0.85 λ. . . . . 64

5.1 Comparison between class-E amplifier and class-E oscillator. Second row shows ideal oscillator performance based on amplfier measurements. Third row shows measured oscillator data. . . . . 74

# FIGURES

FIGURE


2.1 A common configuration for a class-D amplifier is shown in (a). The equivalent circuit is shown in (b), where the devices are replaced by a SPDT switch. . . . . 6

2.2 Class-E amplifier showing output of transistor represented as a switch with the parasitics, $C_s$ and $L_s$, deembedded and included as part of the tuned circuit. . . . . 7

2.3 Ideal class-E amplifier voltage (solid line) and current (dashed line) waveforms at switch. . . . . 9

2.4 Class-E amplifier with transmission line tuned circuit. . . . . 10

2.5 Ideal switch voltage and current waveforms for the class-F amplifier. 11

2.6 Simulated loadlines for a heavily driven MESFET with no output match (solid line), a second harmonic short at the output (dashed line), and a class-E output match (dot-dashed line). . . . . 13

2.7 Measured drain (solid line), power-added (dashed line), and overall (dotted line) efficiency for the 8.4 GHz class-E amplifier. . . . . 14

2.8 Measured output power and power-added efficiency as a function of input power for the 500-MHz class A, E, and F power amplifiers using the same device. . . . . 16

2.9 Measured output power and power-added efficiency as a function of frequency for the 500-MHz class A, E, and F power amplifiers using the same device. . . . . 17

2.10 Measured output power as a function of drain efficiency for the 500-MHz class A, E, and F power amplifiers using the same device. 17

2.11 Measured output power of the fundamental tones and third-order intermodulation products for the 500-MHz class-E (solid line) and class-F (dashed line) amplifiers using the same device. . . . . 18

2.12 Microstrip layout of the 2.5-GHz class-E amplifier. The substrate is Rogers RT5880 Duroid ($\epsilon_r = 2.2$ and $h = 0.508$ mm). Dimensions are given in mm. All lines are 1.6 mm wide for a characteristic impedance of 50 $\Omega$. . . . . 18

2.13 Measured (solid line) and simulated (dashed line) output power and power-added efficiency for the 2.5-GHz class-E amplifier. . . . . 19

2.14 Measured output power (solid line) and power-added efficiency (dashed line) as a function of drain bias voltage, $V_{DS}$, for the 2.5-GHz class-E amplifier. . . . . 19

2.15 Microstrip layout of the class-F amplifier using the FLK052 (a) and the class-E amplifier using the FLK202 (b). The substrate is 0.508-mm thick RT5880 Duroid ($\epsilon_r$=2.2) All dimensions are given in mm. . . . . 20

2.16 Output power and overall efficiency versus frequency for the FLK052 class-F amplifier (solid line) and the FLK202 class-E amplifier (dashed line). The input power is 20 dBm for the FLK052 class-F amplifier and 26 dBm for the FLK202 class-E amplifier. $V_{DS}$=7.0 V and $V_{GS}$=-0.9 V. . . . . 21

2.17 Output power and overall efficiency versus input power for the FLK052 class-F amplifier (solid line) and the FLK202 class-E amplifier (dashed line). The frequency is 8.4 GHz for the FLK052 amplifier and 8.35 GHz for the FLK202 amplifier. $V_{DS}$=7.0 V and $V_{GS}$=-0.9 V. . . . . 22

2.18 Layout of the 10-GHz CPW class-E amplifier. The substrate is Rogers RT6010 duroid ($\epsilon_r$=10.2 and h=1.27 mm). All lines have a characteristic impedance of 50 Ω (w=0.4 mm and w+2s=0.8 mm). . 23

2.19 Measured output power and power-added efficiency as a function of frequency for the 10-GHz class-E (solid line) and class-A (dashed line) power amplifiers. . . . . 23

2.20 Measured output power and power-added efficiency as a function of input power for the 10-GHz class-E (solid line) and class-A (dashed line) power amplifiers. . . . . 24

3.1 Photoconductive sampling measurement setup. . . . . 27

3.2 General outline of class-E and F amplifiers showing locations of photoconductive probing. . . . . 28

3.3 Measured waveform at point **A** in the class-F amplifier. . . . . 29

3.4 Measured waveform at point **B** in the class-F amplifier. . . . . 30

3.5 Measured waveform at point **C** in the class-F amplifier. . . . . 30

3.6 Measured waveform at point **D** in the class-F amplifier. . . . . 31

3.7 Measured waveform at point **E** in the class-F amplifier. . . . . 32

3.8 Measured waveform at point **B** in the class-E amplifier. . . . . 33

3.9 Simulated voltage (solid line) and current (dashed line) waveforms of a 500-MHz class-E amplifier using a Materka-Kacprzak nonlinear model for the Siemens CLY5 MESFET. . . . . 33

3.10 Measured waveform at point **E** in the class-E amplifier. . . . . 34

4.1 A circuit corporate power combiner. The output of an amplifier is connected to each circle. . . . . 38

4.2 A spatial power combiner. The output of an amplifier is connected to each circle. . . . . 39

4.3 Layout of patch antenna for arrays. Substrate is Rogers RT5880 ($\epsilon_r$=2.2 and h=0.508 mm). The feed line has a characteristic impedance of 50 $\Omega$ (w=1.6 mm). . . . . 45

4.4 Measured (solid line) and simulated (dashed line) return loss versus frequency for the patch antenna used in the arrays. Simulation is performed using *Zeland*. . . . . 45

4.5 Calculated input power distribution across the surface of the 9-element(a) and 36-element (b) arrays (F/D=0.87). The feed is a E-plane horn antenna. Numbers are given in dB relative to power received at center of array. . . . . 47

4.6 Drawing of receive (dashed line) and transmit (solid line) sides of active unitcell. . . . . 48

4.7 Output power and phase versus input power for identical amplifiers using three Fujitsu FLK052WG MESFETs with different serial numbers. . . . . 48

4.8 Magnitude and phase of $S_{21}$ for three vias identically made. . . . . 49

4.9 Picture of the feed side (a) and transmit side (b) of the 9-element passive array. . . . . 50

4.10 Recevied power versus feed distance for the 9-element passive array for both feeding with E-plane horn (solid line) and patch (dashed line). . . . . 51

4.11 Measured copolarized (solid line), calculated copolarized (dashed line), and measured cross-polarized (dotted line) radiation patterns for the E-plane (a) and H-plane (b) of the 9-element passive array. 52
4.12 Picture of the transmit side of the 9-element active array. . . . . 53
4.13 Normalized EIRP versus feed distance for the 9-element active (solid line) and passive (dashed line) arrays. The feed is a E-plane horn antenna. . . . . 54
4.14 Measured active copolarized (solid line), passive copolarized (dashed line), and active cross-polarized (dotted line) for the E-plane (a) and H-plane (b) radiation patterns of the 9-element active array. . . 55
4.15 Copolarized E-plane (a) and H-plane (b) radiation patterns of the 9-element active array for the measured saturated (solid line) and small-signal (dashed line) array. Also shown are the calculated patterns assuming uniform amplitude distribution (dotted line) and amplitude distribution from Fig. 4.5(a) (dot-dashed line). . . . . 56
4.16 Picture of the feed side (a) and transmit side (b) of the 36-element active array. . . . . 59
4.17 Normalized received power versus feed distance for the 36-element active array. The feed is a E-plane horn antenna. . . . . 60
4.18 Measured copolarized (solid line) and cross-polarized (dotted line) for the E-plane (a) and H-plane (b) radiation patterns of the 36-element active array. . . . . 61
4.19 Copolarized E-plane (a) and H-plane (b) radiation patterns of the 36-element active array for the measured saturated (solid line) and small-signal (dashed line) array. Also shown are the calculated patterns assuming uniform amplitude distribution (dotted line) and the amplitude distribution from Fig. 4.5(b) (dot-dashed line). . . . 62

4.20 Frequency sweep of the active unitcell (solid line), passive 9-element array (dashed line), 9-element active array (dotted line), and 36-element active array (dot-dashed line). . . . . 63
5.1 Layout of 5-GHz microstrip class-E oscillator. . . . . 67
5.2 5-GHz class-E amplifier in microstrip. . . . . 68
5.3 Measured output power (solid line) and power-added efficiency (dashed line) of the 5-GHz class-E amplifier. . . . . 69
5.4 Microstrip layout of the branch-line coupler used in the 5-GHz class-E oscillator. . . . . 69
5.5 Simulated response of asymmetric branch-line coupler. . . . . 70
5.6 Simulated circular function for the unsaturated class-E oscillator. The dashed line shows an oscillation near 600 MHz and solid line shows an oscillation near 5 GHz. . . . . 71
5.7 Measured spectrum of the 600-MHz (a) and 5-GHz (b) modes of the class-E oscillator. . . . . 72
5.8 Output power and conversion efficiency versus drain current, $I_{DS}$, with $V_{DS} = 6.5\,V$ (solid line), $V_{DS} = 8\,V$ (dashed line) and $V_{DS} = 9.5\,V$ (dotted line) for the 5-GHz class-E oscillator. . . . . 73
5.9 The class-E power amplifier antenna array. This 4-element power-combiner demonstrates 2.4 W of output power at 5.05 GHz with 8.8 dB compressed gain, 74% drain efficiency, and 64% power-added efficiency. . . . . 75
5.10 The class-E external feedback oscillator array. . . . . 76
5.11 Measured oscillation frequency and recived radiated power as a function of the distance from amplifier array to twist reflector for the array back side (circles) and front side (crosses) facing reflector. 77

5.12 Measured recived radiated power as a function of angle of twist reflector with respect to output antennas for the array back side (circles) and front side (crosses) facing reflector. . . . . 77

5.13 Measured recived radiated power of the free-space oscillator array as a function of drain current for array back side (a) and front side (b) facing reflector. (a) is measured at an array-reflector distance of 87 mm. (b) is measured at an array-reflector distance of 42 mm. $V_{DS}$ is 6.5 V (solid line), 8.0 V (dashed line), and 9.5 V (dotted line). 78

5.14 Measured E-plane (a) and H-plane (b) radiation patterns for co-polarized (solid line) and cross-polarized (dashed line) radiation. . . 80

5.15 Calculated array factor for E- and H-planes (solid line), and the two 45° planes (dashed and dotted lines). . . . . 81

6.1 General layout of frequency doublers showing locations of photoconductive probing. . . . . 84

6.2 Measured output power at the fundamental and first three harmonics versus input frequency for the 1-GHz doubler ($P_{\text{in}}$=15 dBm, $V_{DS}$=5 V, and $I_{DS}$=110 mA). . . . . 85

6.3 Measured second-harmonic drain, power-added, and overall efficiencies versus input frequency for the 1-GHz doubler ($P_{\text{in}}$=15 dBm, $V_{DS}$=5 V, and $I_{DS}$=110 mA). Efficiencies are defined in terms of the output power at the second harmonic. . . . . 86

6.4 Simulated drain voltage (solid line) and current (dashed line) waveforms for the 1-GHz doubler. . . . . 87

6.5 Measurements of the time-domain waveforms at points **A**-**D** in the 500 MHz to 1 GHz doubler. . . . . 87

6.6 Measured output power at the fundamental (2.5 GHz) and first three harmonics versus input power for the 5-GHz doubler ($V_{DS}$=8 V and $I_{DS}$=100 mA). . . . . 88

6.7 Measured second-harmonic (5.0 GHz) drain, power-added, and overall efficiencies versus input power for the 5-GHz doubler ($V_{DS}$=8 V and $I_{DS}$=100 mA). Efficiencies are defined in terms of output power at the second harmonic. . . . . 89

6.8 Measured time-domain waveforms at points **A**-**D** in the 2.5 GHz to 5.0 GHz doubler. . . . . 90

# CHAPTER 1

# INTRODUCTION AND BACKGROUND

## 1.1 Introduction

Crowding of the spectrum and the need for more bandwidth have pushed communication applications into the upper microwave and millimeter-wave frequency range. Military applications, including ground- or ship-based radar, missile seekers, and short range battlefield communications operate at frequencies up to 94 GHz with required power levels ranging from tens to hundreds of watts. This has greatly increased the need for medium-to-high level power sources at these frequencies. Traditionally this need has been met by vacuum-tube devices, such as klystrons and travelling wave tubes (TWTs). These devices are bulky, expensive, and have limited lifetimes. Solid-state devices offer a cheap and lightweight alternative. For very high millimeter-wave powers (above a few tens of watts), vacuum-tube devices are necessary. But for the medium power levels required in most modern communication systems, solid-state devices are an attractive option.

An important figure of merit when comparing vacuum-tube power sources to solid-state power sources is cost per Watt. A Ka band TWT recently ordered from Litton that produces 10-20 W output power with less than 10% efficiency costs $55,000 and had a delivery time of 20 months. This works out to roughly $4,000 per watt, illustrating the need for low-cost sources of millimeter-wave power.

Low cost, light weight, and good reliability are the key factors in the development of solid-state sources. For reliability and weight issues, high efficiency is a

prime concern. Higher efficiency results in increased battery lifetimes, higher reliability, and lower heat sinking requirements. To address high efficiency in this thesis, switched-mode amplifier techniques are employed. As opposed to linear classes of operation, switched-mode operation requires the amplifier to be driven into saturation and harmonic tuning.

Individual solid-state devices are incapable of producing large amounts of power at millimeter-wave frequencies. The output power from a single device drops off as one over frequency squared due to reduced heat sinking capability and impedance matching considerations. Therefore, to obtain tens of watts of output power, several soild state devices must be combined. Many circuit-based power combining techniques have been devised, but these suffer from higher transmission losses at millimeter-wave frequencies. Spatial power combining, a good overview of which is given in [1], offers an attractive option for combinining hundreds of devices and is investigated in this thesis as it relates to high efficiency.

Switched-mode techniques have been applied extensively to rf frequencies and most recently to microwaves by Mader [2]--[4]. Mader designed, built, and characterized class-E amplifiers at 0.5, 1, 2, and 5 GHz, as well as demonstrated a 5-GHz 4-element spatial power combiner using class-E amplifiers. The intent of this thesis is to build upon this work, comparing switched-mode class-E and class-F amplifiers up to 10 GHz, applying switched-mode design techniques to other microwave circuits (oscillators and multipliers), and investigating further the spatial power combining of high-efficiency amplifiers.

## 1.2 Solid-State Device Capabilities

It is instructive to look at the state-of-the-art in power device technology. It should be noted that these are all devices out of research labs and not commercially available. The work done in this thesis is with commercially available devices and

therefore only goes up to X band, so the results reported below and the results reported in this thesis are difficult to compare.

GaAs MESFETs have traditionally been the semiconductor device of choice for microwave power amplifiers and are the devices used for the work in this thesis. As possible replacements at microwave frequencies for MESFETs, there has been extensive work investigating heterojunction bipolar transistors (HBTs). Recent results include a AlGaAs/GaAs HBT with 2.09 W output power, 62.2% power-added efficiency (PAE), and 7.13 dB gain at 10 GHz [5] and a GaInP/GaAs HBT power amplifier with 9 W output power and 42% PAE at 10 GHz [6]. At 18 GHz, a AlInAs/InGaAs/InP double HBT (DHBT) produced 1.17 W output power operating in class B mode with 54% PAE and 7.3 dB gain [7]. At 30 GHz, an InP DHBT obtained 19.1mW output power with 35.5% PAE and 5.3 dB gain [8].

Heterojunction FETs (HFETs), also called HEMTs (high electron mobility transistors), are the devices being investigated for frequencies greater than 30 GHz. Recent examples include a 60 GHz GaInP/InGaAs/GaAs pseudomorphic HEMT (pHEMT) with 17.5 dBm output power, 22.5% PAE, and 4.6 dB gain from a single device [9]. In [10], a 2-stage 60-GHz pHEMT power amplifier was made with 272 mW output power, 24% PAE, and 9.4 dB gain. W-band examples include a 95-GHz 2-stage MMIC amplifier with 427 mW output power, 19% PAE, and 8.8 dB gain [11]. A single InP HEMT device achieved 58 mW output power with 33% PAE and 6.4 dB gain at 94 GHz [12]. This device had a $f_{max}$ of 600 GHz.

Device technology has been improving at a rapid pace. The intent of this work is to demonstrate how to utilize these new devices to produce low-cost, reliable, and efficient sources of microwave and millimter-wave power. Using the high-freqeuncy HEMTs described above, these techniques can be applied to frequencies above that of the work presented in this thesis.

## 1.3 Organization of the Thesis

This thesis is concerned with the generation of medium levels of output power (tens of watts) at microwave and millimeter-wave frequencies in an efficient manner using switched-mode operation of solid-state devices.

Chapter 2 presents an overview of switched-mode techniques and their application to microwave frequencies. Several experimental examples are given from 500 MHz to 10 GHz with measurements of power and efficiency.

In chapter 3, a technique is described for measuring the time-domain measurements of microwave circuits using a photoconductive sampling probe. Waveform measurements are presented for X-band class-E and class-F amplifiers and compared to the ideal waveforms.

The problem of combining solid-state devices is addressed in chapter 4. Methods of power combining are compared using experimental data from the X-band amplifiers described earlier. Several spatial power combining arrays are presented with measurements of equivalent isotropic radiated power (EIRP), effective transmitter power, radiation patterns, and combining efficiency. Feeding of these power arrays is also discussed.

The switched-mode approach can also be applied to other types of circuits, not just power amplifiers. Chapter 5 presents work done in using the class-E amplifier as a feedback oscillator. A microstrip class-E oscillator and a 4-element free-space class-E oscillator array using global feedback are presented.

High-efficiency multipliers are presented in chapter 6. Design and measurements of two class-E multupliers are presented including time-domain waveform measurements.

Finally, chapter 7 gives a summary of the thesis and some suggestions for future work in this area.

# CHAPTER 2

# COMPARISON OF SWITCHED-MODE POWER AMPLIFIER TOPOLOGIES

## 2.1 Introduction

Improving the output power and efficiency of microwave amplifiers requires investigation of power amplifier modes beyond the standard classes A-C. In classes A-C, the transistor is driven to act like a current or saturated current source. In the power amplifier topologies discussed here (classes D, E, and F), the transistor is driven with a large input signal, so the transistor acts like a switch. These amplifiers are typically called switched-mode amplifiers. They can have very high efficiency since the switching action allows the voltage and current to be out of phase at the output of the device. Therefore, no power is dissipated in the device. Class-D amplifiers employ two transistors in push-pull to act like a SPDT switch. Class E and F amplifiers use a single transistor to act like a switch. They are therefore called *single-ended* switched-mode amplifiers. This chapter briefly describes the operation of class D, E, and F amplifiers, discusses modeling issues, and presents experimental examples of several class-E and F microwave amplifiers for comparison.

## 2.2 Switched-Mode Topologies

**2.2.1 Class-D** In the class-D power amplifier [13], the common configuration is to drive two transistors in push-pull, as shown in Fig. 2.1(a). Since the two devices are driven 180° out of phase with one another, they effectively switch back and forth between the drain (or collector) voltage and ground, as shown in

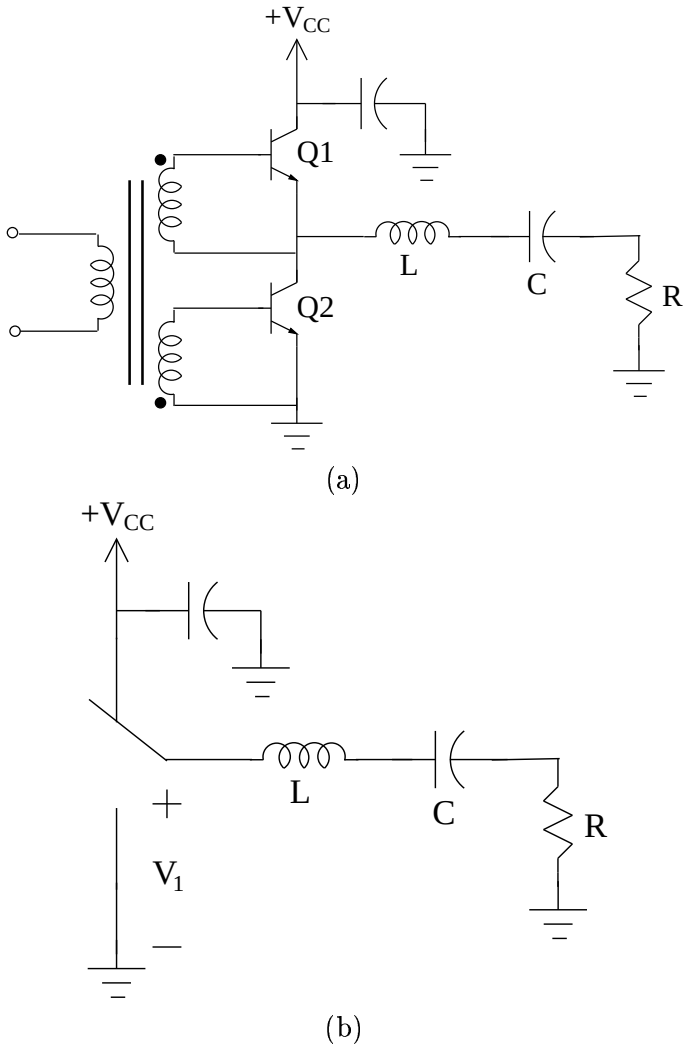


Figure 2.1. A common configuration for a class-D amplifier is shown in (a). The equivalent circuit is shown in (b), where the devices are replaced by a SPDT switch.

Fig. 2.1(b), resulting in a square wave. The resonant LC circuit filters out the desired harmonic into the load. Since the active devices are ideally acting like a lossless SPDT switch, no power is dissipated in the devices.

However, such a configuration cannot be used at microwave frequencies since devices have significant parastics, especially capacitance across the output terminals, which limit their switching times. In [14], the losses due to finite switching times at rf frequencies are described and calculated.

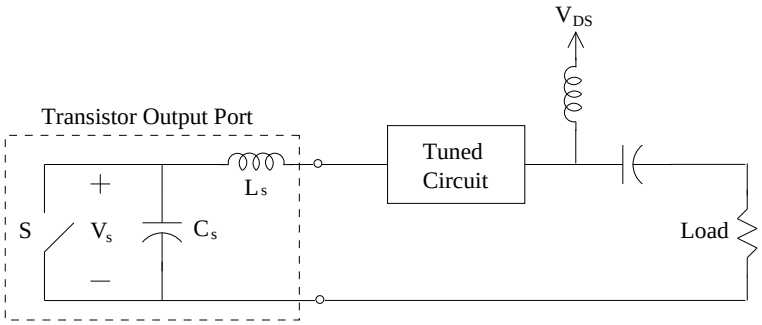


Figure 2.2. Class-E amplifier showing output of transistor represented as a switch with the parasitics, $C_s$ and $L_s$, deembedded and included as part of the tuned circuit.

**2.2.2 Class-E** The class-E amplifier is a single-ended switched-mode amplifier. Ideally, the product of the switch voltage and current is zero, resulting in 100% efficiency. In practice, the efficiency is limited by the drain-to-source saturation resistance and finite switching time of the transistor. The transistor is driven to act like a switch and the surrounding circuitry is designed to give class-E operation. Device parasitic reactances are included in the tuned circuit design, as shown in Fig. 2.2. Switching losses are minimized by applying three boundary conditions to the switch voltage and current waveforms:

- Voltage is zero when switch turns off.
- Voltage is zero when switch turns on.
- Derivative of voltage is zero when switch turns on.

The final condition ensures that a jump in current is not required when the switch turns on. However, a jump in current *is* required when the switch turns off.

The class-E amplifier was introduced by Sokal [15], [16] in 1975. Raab [17] expanded upon this work by deriving the basic equations governing class-E operation using Fourier series analysis and a high-Q load network assumption. Raab also investigated the effects of nonideal components on the performance of the class-E amplifier [18]. Mader [2]--[4] rederived design equations using a transmission-line topology. The analysis is briefly outlined here for completeness.

A high-Q tuned circuit is assumed so that only a single frequency component is present at the load. When the switch is turned off, only a dc and fundamental frequency component of current is flowing through the capacitor:

$$C_s \frac{dv_s}{dt} = I_{DS}(1 - a\sin(\omega_s t + \phi)). \tag{2.1}$$

The switch voltage, $v_s$, is calculated by applying the first boundary condition ($v_s(0) = 0$):

$$v_s(t) = \frac{I_{DS}}{C_s}\int_0^t (1 - a\sin(\omega_s t' + \phi))dt' \tag{2.2}$$

$$v_s(t) = \frac{I_{DS}}{\omega_s C_s}(\omega_s t + a(\cos(\omega_s t + \phi) - \cos\phi)) \tag{2.3}$$

To calculate the two unknown constants, $a$ and $\phi$, the last two boundary conditions are applied ($v_s(\pi) = 0$ and $\frac{dv_s}{dt}(\pi) = 0$):

$$a = \sqrt{1 + \frac{\pi^2}{4}} \approx 1.862 \tag{2.4}$$

$$\phi = -\arctan\frac{2}{\pi} \approx -32.48°. \tag{2.5}$$

The resulting switch voltage and current waveforms for ideal class-E operation are shown in Fig. 2.3. As shown, a jump in current is required at switch-off ($\omega_s t = 2\pi$).

Using Fourier series analysis, the fundamental frequency components of switch voltage and current can be found and used to calculate the impedance that needs to be seen by the switch at that frequency:

$$Z_{net} \approx \frac{0.28015}{\omega_s C_s} e^{j49.0524°}. \tag{2.6}$$

If the dc components of switch voltage and current are calculated, an equation for maximum frequency of ideal class-E operation can be found for a given $V_{DS}$, $C_s$, and $I_{DSS}$ (maximum allowable drain current):

$$f_{max} \approx \frac{I_{DSS}}{56.5 C_s V_{DS}}. \tag{2.7}$$

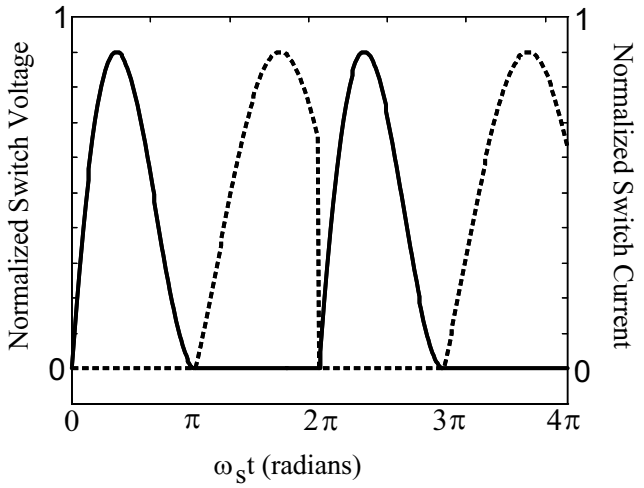


Figure 2.3. Ideal class-E amplifier voltage (solid line) and current (dashed line) waveforms at switch.

This frequency is significantly less than the $f_T$ or $f_{max}$ of the device (typically at least three times less). Above this maximum frequency, the class-E amplifier operates in "suboptimum" mode [19], although it can still have relatively high efficiency.

The previous analysis assumes a large impedance at the higher harmonics. It can be shown [4] that the second harmonic is important for the switch voltage waveform. The impedance at higher harmonics is not as relevant, especially considering that transistors at microwave freqeuncies do not have much gain beyond the second harmonic. In Fig. 2.4, an example is shown of a transmission-line tuned circuit design that meets the impedance condition at the fundamental and second harmonic. $l_2$ is $\frac{\lambda}{4}$ at the second harmonic so that an open is transformed to a short at plane aa'. $l_1$ plus the equivalent length of $L_s$ and $C_s$ is also $\frac{\lambda}{4}$ at the second harmonic to translate the short back to an open at the switch. The combination of $l_1$-$l_4$ provides the impedance $Z_{net}$ at the fundamental. However, it is commonly the case that a single-stub match will provide both $Z_{net}$ at the fundamental and a large impedance at the second harmonic.

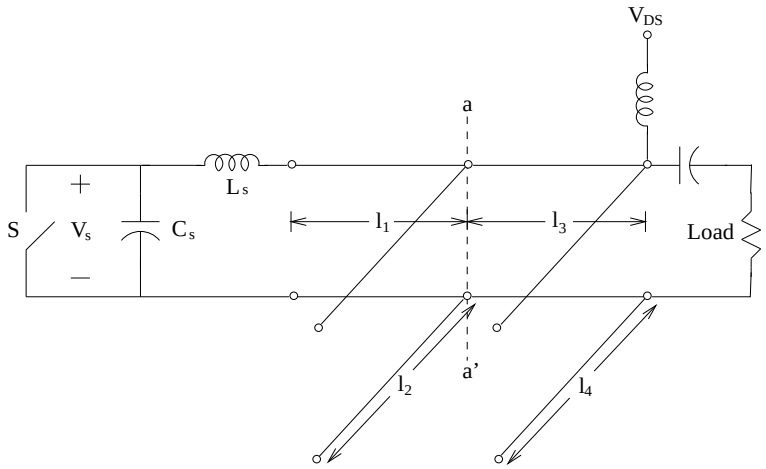


Figure 2.4: Class-E amplifier with transmission line tuned circuit.

An exact analysis can also be done without assuming a high-Q tuned circuit [20] using Laplace transforms. In [21], the analysis is performed without assuming a large Q or a perfect RF choke on the dc feed. Molnar [22] and Kazimierczuk [23] showed that it is impossible to have 100% efficiency and nonzero output power using a single-ended switched-mode (class-E) power amplifier. They show that to have nonzero output power with 100% efficiency requires a jump in current or voltage at switch-off or switch-on. As mentioned earlier, the class-E amplifier described here requires a jump in current at switch-off. Since this is impossible without an ideal switch, a finite amount of power dissipation must occur at this point.

**2.2.3 Class-F** The idea of using harmonic tuning to achieve higher efficiencies through waveshaping goes back to 1958 [24]. Although in a class-F amplifier, the transistor is commonly used as a current or saturating current source [13], here is discussed a switched-mode class-F amplifier where the transistor is driven to act like a switch. Therefore, the model for the output of the class-F amplifier is the same as for the class-E, Fig. 2.2.

In the ideal class-F amplifier, a resonant load network circuit presents a short to all even harmonics and an open to all odd harmonics. Therefore, if the

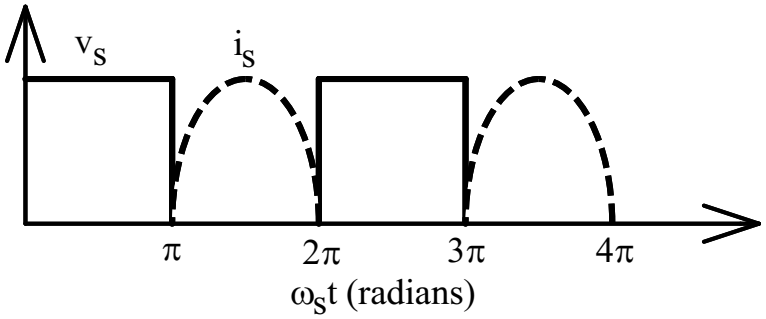


Figure 2.5: Ideal switch voltage and current waveforms for the class-F amplifier.

amplitudes are chosen carefully, the voltage at the drain terminal is a square wave and the current is a half-sinusoid out of phase with the voltage, as shown in Fig. 2.5. Therefore, there is no voltage-current product at the switch and no power dissipated in the device.

At microwave frequencies, transmission lines are used for the tuned circuit, so all harmonics cannot be controlled. One set of series and stub lines are needed for each harmonic impedance to be controlled. In practice, only up to the second or third harmonic are considered. Also, devices do not have much gain above the third harmonic at these high frequencies. So, as with the class-E transmission-line amplifier, Fig. 2.4, one stub match for the second harmonic short and one for the fundamental impedance are used.

At the fundamental impedance, the device should be matched for maximum power transfer to the load. This impedance is different than that required for maximum gain. For maximum *linear* power (before the gain compresses), it is a well-known result at lower frequencies that the load must be resistive and given by

$$R_{opt} = \frac{2V_{DS}}{I_{DSS}}, \tag{2.8}$$

where $I_{IDSS}$ is the maximum allowable drain current. Cripps [25], [26] demonstrated that the match for maximum linear power corresponds to the match for maximum saturated power. Like the class-E amplifier, the parasitics $C_s$ and $L_s$ are included

as part of the tuned circuit.

## 2.3 Modeling of Switched-Mode Amplifiers

Modeling of switched-mode amplifiers requires transistor models that are accurate at high drive levels. These are difficult to obtain. Some success has been achieved using the Materka-Kacprzak model [27] for the Siemens CLY5 MESFET with Ansoft's *Serenade* harmonic balance simulator from 500 MHz to 2 GHz [3]. Above these frequencies, it is very difficult to accurately extract all the necessary parameters to model switched-mode operation. Nonlinear modeling of microwave transistors is an area of intense current research. Sokal proposed using a fairly simple switch model [28]. This works reasonably well as a starting point for design, but does not represent actual performance very well over a wide range of drive levels and frequencies and does not model input matching.

Fig. 2.6 shows simulated loadlines (using *Serenade*) for a few different output matches. When there is no output matching circuit (solid line), the loadline is a straight line. When a second harmonic short is added (dashed line), one portion of the loadline bows in toward the axes. This results in higher efficiency, since the total voltage-current product is less. When a class-E match is used (dot-dashed line), including a high impedance at the second harmonic, the loadline also moves toward the axes. It should also be noted that only one portion of the loadline approaches the axes, while the other remains straight. This is a consequence of the previously mentioned fact that it is impossible to have 100% efficiency and nonzero output power. There must either be loss at switch-on or switch-off. Here, there is loss at switch off, represented by the straight portion of the loadline, which is in the region of high power dissipation.

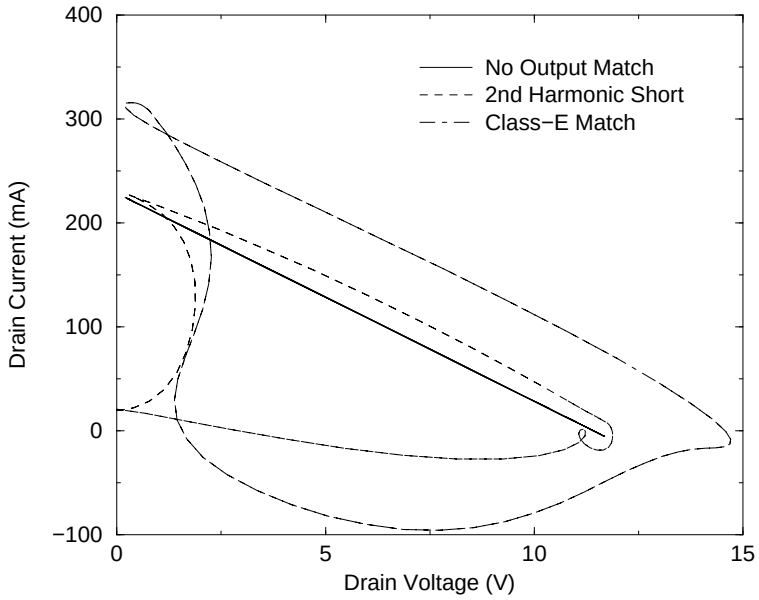


Figure 2.6. Simulated loadlines for a heavily driven MESFET with no output match (solid line), a second harmonic short at the output (dashed line), and a class-E output match (dot-dashed line).

## 2.4 Examples

**2.4.1 Definitions of Efficiency** There are a few different ways to define efficiency for an amplifier and each definition has a particular usefulness. The first definition is called drain efficiency (or collector efficiency). This is simply the rf output power over the dc power supplied to the drain (or collector),

$$\eta_D = \frac{P_{\text{out}}}{P_{\text{dc}}}. \tag{2.9}$$

This is the conversion efficiency of dc to rf at the drain. It does not, however, include gain. It is therefore possible to have an amplifier with 100% drain efficeincy, but zero or negative gain.

A second definition, power-added efficiency, takes into account the gain of the amplifier, and is therefore more indicative of the quality of amplifier. It is defined as the rf output power minus the rf input power, all over the supplied dc power,

$$PAE = \frac{P_{\text{out}} - P_{\text{in}}}{P_{\text{dc}}}. \tag{2.10}$$

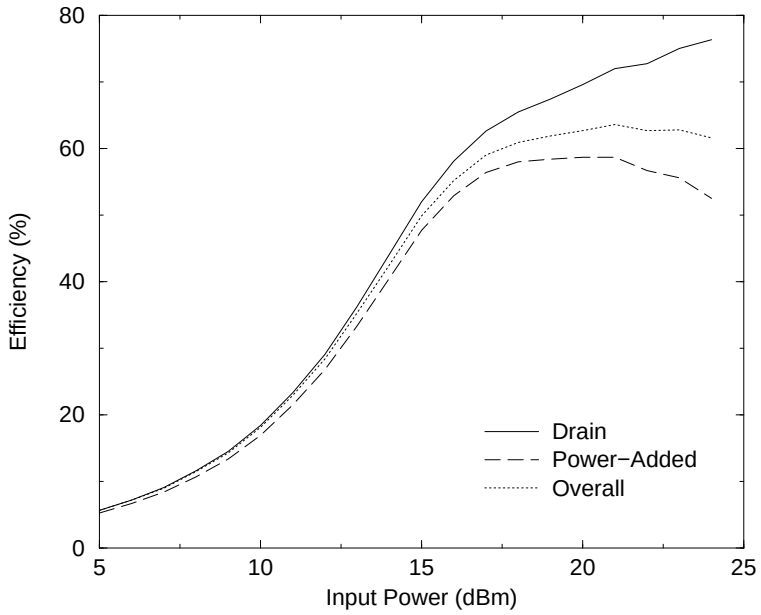


Figure 2.7. Measured drain (solid line), power-added (dashed line), and overall (dotted line) efficiency for the 8.4 GHz class-E amplifier.

This definition is useful when looking at feedback oscillators, since the power-added efficiency is the same as the conversion efficiency for an oscillator using the previous amplifier in a feedback loop.

The last definition is called overall efficiency. This defintion is most relavant to heat dissipation since it defines the total output power (rf) over the total input power (dc + rf),

$$\eta = \frac{P_{\text{out}}}{P_{\text{dc}} + P_{\text{in}}}. \tag{2.11}$$

To illustrate the differences, Fig. 2.7 shows the measured drain, power-added, and overall efficiency for the 8.4 GHz class-E amplfiier described in section 2.4.3.

**2.4.2 500-MHz Power Amplifiers** In [2], three experimental class-E circuits are presented using the Siemens CLY5 MESFET at 0.5, 1, and 2 GHz. To compare the class-E amplifier with other topologies, a class-A and a class-F amplifer were designed and built at 500 MHz using the same transistor and substrate as

the class-E amplifier designed by Mader [3]. The class-A and class-F amplifiers are designed using the values for $C_s$ and $L_s$ obtained when designing the class-E amplifier.

The output power and power-added efficiency are measured as a function of input power level and frequency for both the class-A and class-F amplifers and plotted together with the results for the 500-MHz class-E amplifer. The power sweep is plotted in Fig. 2.8 and the frequency sweep is plotted in Fig. 2.9. As the device is driven into saturation, the class-A amplifier is no longer operating in class A, but rather class AB. It is interesting to note that the gain of the class-E amplifier compresses at a lower input power level than the gain of the class F. This is because the class-F amplifier is matched at the fundamental for maximum linear power delivered to the load. While the class-E amplifer yields the highest efficiency, Fig. 2.10 shows that for a given efficiency, the class-F amplifier generates more output power.

Another consequence of the class-F amplifier being matched for maximum linear power delivered to the load can be seen in Fig. 2.11. For approximately the same maximum output power, the third-order intermodulation products are 10 dB lower for the class-F amplifier. The interpolated intercept point, however, occurs at the same input power level.

**2.4.3 2.5-GHz Class-E Amplifier** In order to test the accuracy of the nonlinear model for the FLK052 MESFET at higher frequencies, a class-E amplifier was designed and fabricated to work at 2.5 GHz using the Fujitsu FLK052 MESFET. The purpose of this design was twofold. First of all, it was of interest to see if *Serenade* could somewhat accurately predict frequency response. The original purpose of this amplifier was to serve as a driver for an electrooptic modulator. It therefore needed to have high efficiency while providing relatively low output power. Therefore, measurements were needed to verify that this could be done by simply

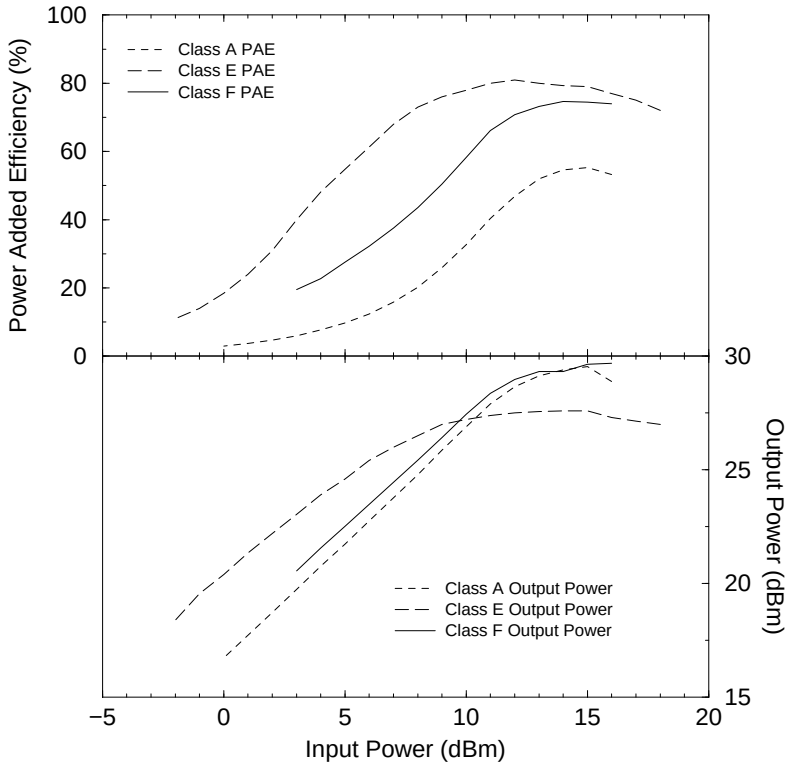


Figure 2.8. Measured output power and power-added efficiency as a function of input power for the 500-MHz class A, E, and F power amplifiers using the same device.

lowering the drain bias voltage, $V_{DS}$.

Fig. 2.12 shows the layout of the fabricated amplifier in microstrip. Fig. 2.13 shows a comparison between the harmonic balance simulation results and actual measured results. As the figure shows, the maxima differ slightly and the measured frequency response is more wideband, but this still shows that the harmonic balance simulator can be used to predict the center frequency of operation, if not the bandwidth.

Fig. 2.14 shows the measured output power and power-added efficiency as a function of drain voltage. Even though the output power drops, the efficiency remains above 70% for $V_{DS}$ above 1 V.

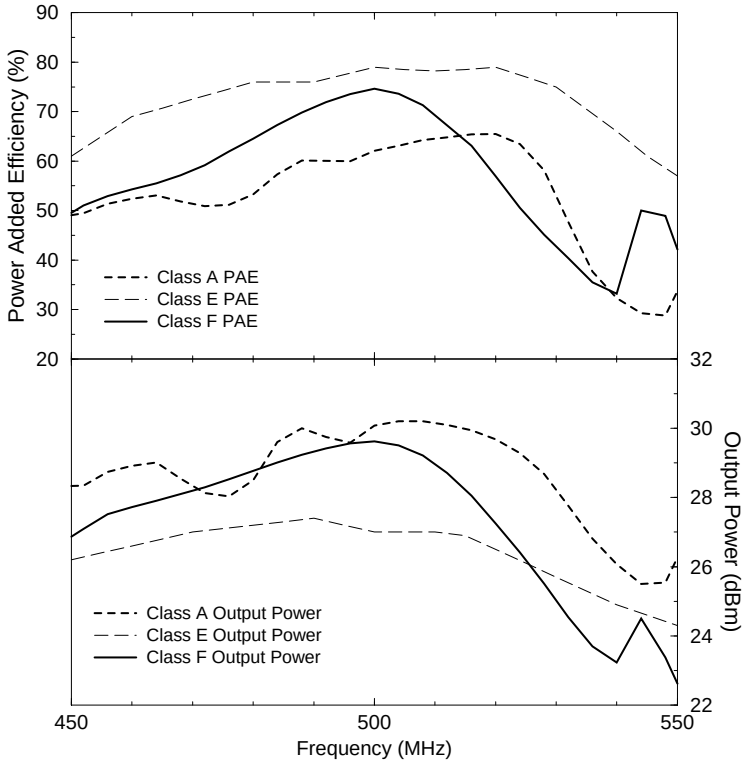


Figure 2.9. Measured output power and power-added efficiency as a function of frequency for the 500-MHz class A, E, and F power amplifiers using the same device.

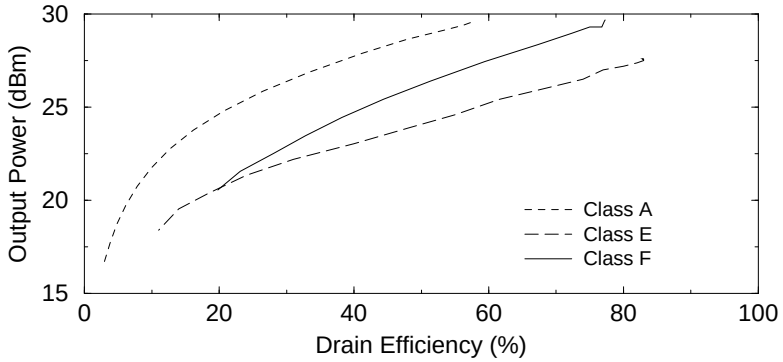


Figure 2.10. Measured output power as a function of drain efficiency for the 500-MHz class A, E, and F power amplifiers using the same device.

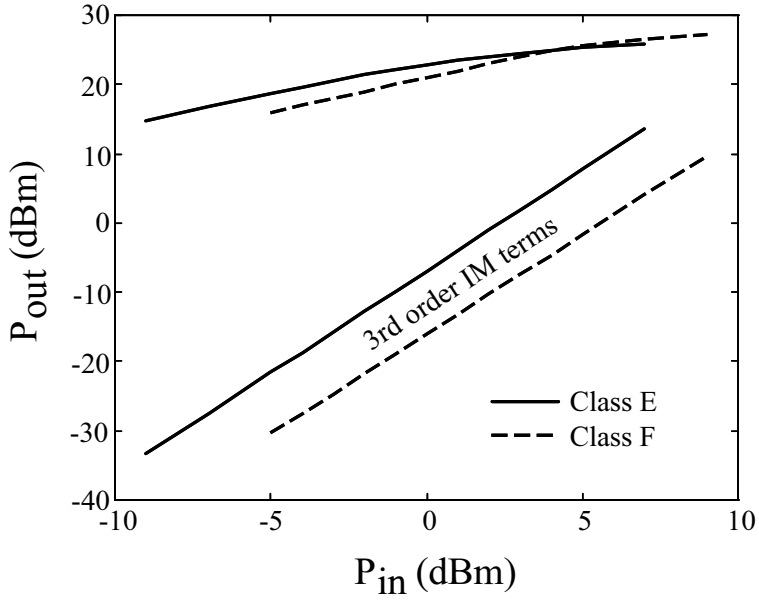


Figure 2.11. Measured output power of the fundamental tones and third-order intermodulation products for the 500-MHz class-E (solid line) and class-F (dashed line) amplifiers using the same device.

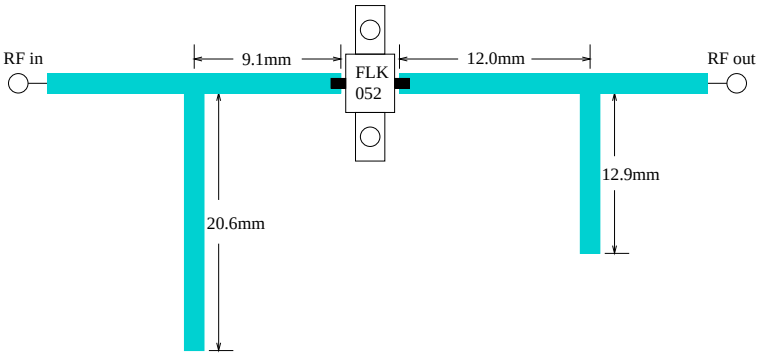


Figure 2.12. Microstrip layout of the 2.5-GHz class-E amplifier. The substrate is Rogers RT5880 Duroid ($\epsilon_r = 2.2$ and $h = 0.508\,\text{mm}$). Dimensions are given in mm. All lines are 1.6 mm wide for a characteristic impedance of $50\,\Omega$.

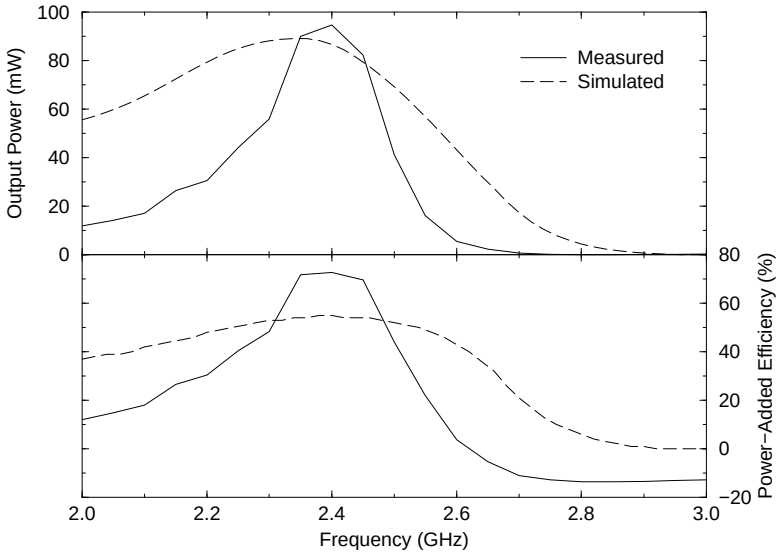


Figure 2.13. Measured (solid line) and simulated (dashed line) output power and power-added efficiency for the 2.5-GHz class-E amplifier.

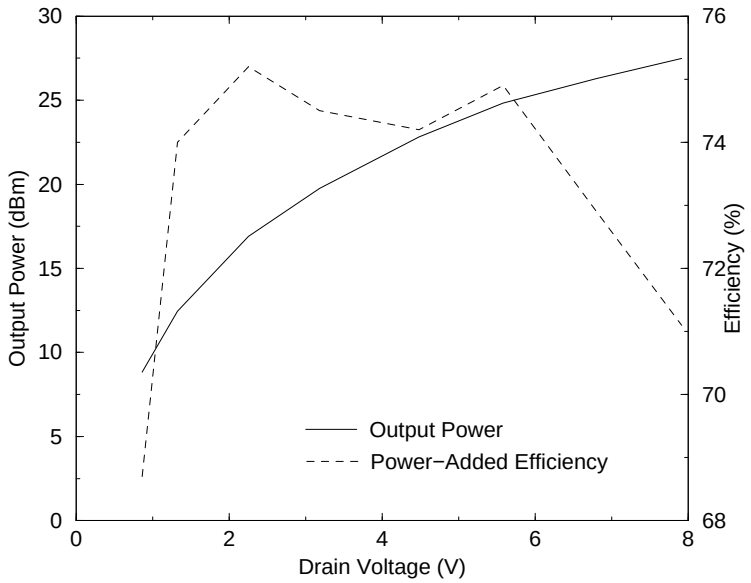


Figure 2.14. Measured output power (solid line) and power-added efficiency (dashed line) as a function of drain bias voltage, $V_{DS}$, for the 2.5-GHz class-E amplifier.

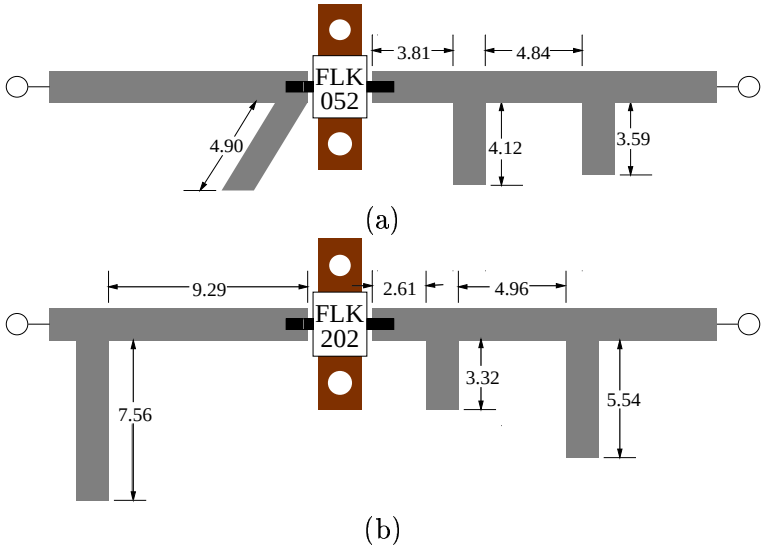


Figure 2.15. Microstrip layout of the class-F amplifier using the FLK052 (a) and the class-E amplifier using the FLK202 (b). The substrate is 0.508-mm thick RT5880 Duroid ($\epsilon_r$=2.2) All dimensions are given in mm.

**2.4.4 8-GHz Power Amplifiers** A switched-mode class-F amplifier using the FLK052 and a class-E amplifier using the four-times larger FLK202 were designed on 0.508-mm Rogers Duroid RT5880 ($\epsilon_r$=2.2). The layout of each amplifier is shown in Fig. 2.15. The class-F amplifier is shown in (a). The 3.81 mm line and 4.12 mm open stub provide the second harmonic short. This in combination with the 4.84 mm line and the 3.59 mm open stub provide the fundamental match. The class-E amplifier is shown in (b). The second harmonic is terminated in an open circuit, provided by the 2.61 mm line and 3.32 mm stub. The 4.96 mm line and 5.54 mm stub in combination with the second harmonic circuitry provide the class-E impedance at the fundamental. Time-domain waveform measurements of these amplifiers are shown in the next chapter.

The output power and efficiency for each amplifier were measured as a function of frequency and input power. Fig. 2.16 shows the output power and overall efficiency versus frequency for the FLK052 class-F and the FLK202 class-E amplifiers. Fig. 2.17 shows the output power and overall efficiency versus input power for the

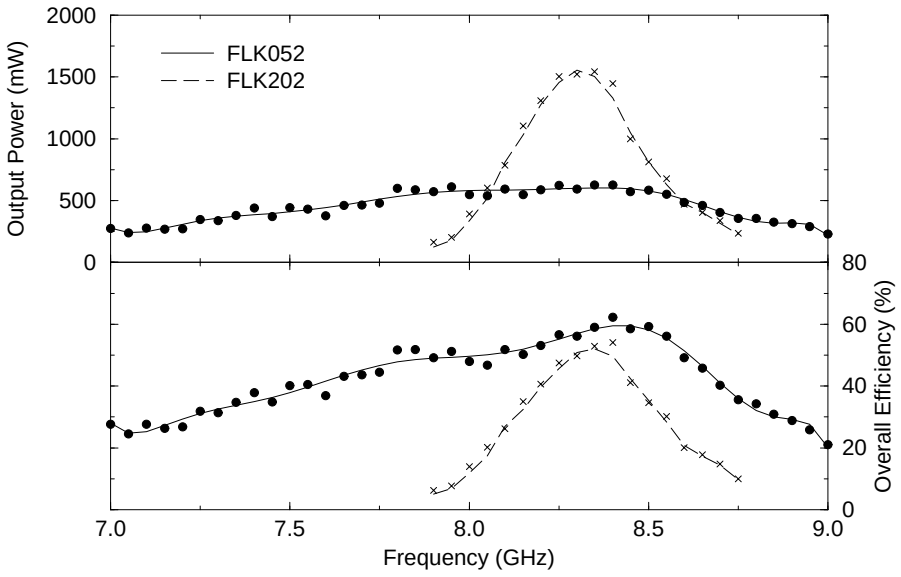


Figure 2.16. Output power and overall efficiency versus frequency for the FLK052 class-F amplifier (solid line) and the FLK202 class-E amplifier (dashed line). The input power is 20 dBm for the FLK052 class-F amplifier and 26 dBm for the FLK202 class-E amplifier. $V_{DS}$=7.0 V and $V_{GS}$=-0.9 V.

FLK052 amplifier and the FLK202 amplifier. The FLK052 class-F amplifier has a high overall efficiency at 8.4 GHz of 64% with 685 mW output power. The FLK202 class-E amplifier has a high overall efficiency at 8.35 GHz of 57% with 1.7 W output power.

**2.4.5 10-GHz Class-E Amplifier** To achieve class-E operation at higher frequencies, transistors with lower values of $C_s$ need to be used. Since the package contributes a significant amount of parasitic capacitance, unpackaged chip devices will need to be used for switched-mode amplifier at millimeter-wave frequencies. As a precursor to millimeter-wave designs, a 10-GHz class-E amplifier was designed, fabricated, and measured using an Alpha AFM08-P2 chip MESFET. These devices have appreciable gain up to and including Ka-band. However, their maximum frequency of ideal class-E operation is only 6 GHz. Coplanar Waveguide (CPW) was chosen as the guiding medium due to its amenability with chip devices. The source (which is connected through an on-chip via to the back of the chip) can

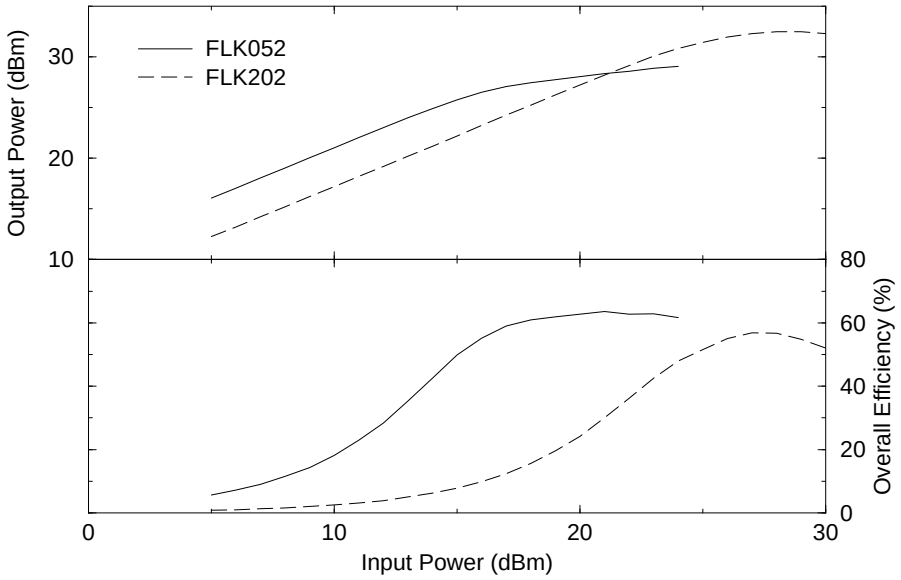


Figure 2.17. Output power and overall efficiency versus input power for the FLK052 class-F amplifier (solid line) and the FLK202 class-E amplifier (dashed line). The frequency is 8.4 GHz for the FLK052 amplifier and 8.35 GHz for the FLK202 amplifier. $V_{DS}$=7.0 V and $V_{GS}$=-0.9 V.

be connected directly to the ground plane of the CPW using silver epoxy. Fig. 2.18 shows the layout of the CPW 10-GHz class-E amplifier.

This class-E amplifier produced 275 mW output power with 48% power-added efficiency and 6.4 dB gain at 10 GHz. A class-A amplifier was also fabricated using this same device. Measurements showing a comparison between these two amplifers are shown in Fig. 2.19 and Fig. 2.20.

A driver stage was designed and fabricated for this class-E amplifer using the Alpha AFM04P2 MESFET, which has a gate periphery half the size of the AFM08P2. The resulting two-stage amplifier produced 210 mW output power with 37% power-added efficiency and 13.2 dB gain. The goal of this work was to use this two-stage amplifier in a spatial power-combining array [29], but the slotline mode of the CPW lines proved too difficult to suppress to a level sufficiently low to prevent instabilities in the array.

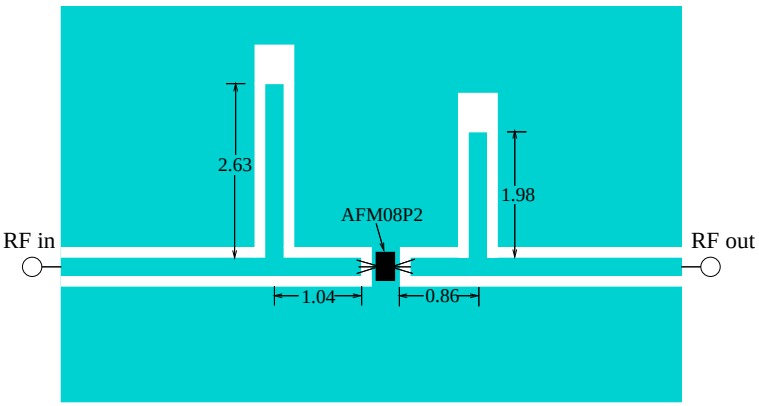


Figure 2.18. Layout of the 10-GHz CPW class-E amplifier. The substrate is Rogers RT6010 duroid ($\epsilon_r$=10.2 and h=1.27 mm). All lines have a characteristic impedance of 50 Ω (w=0.4 mm and w+2s=0.8 mm).

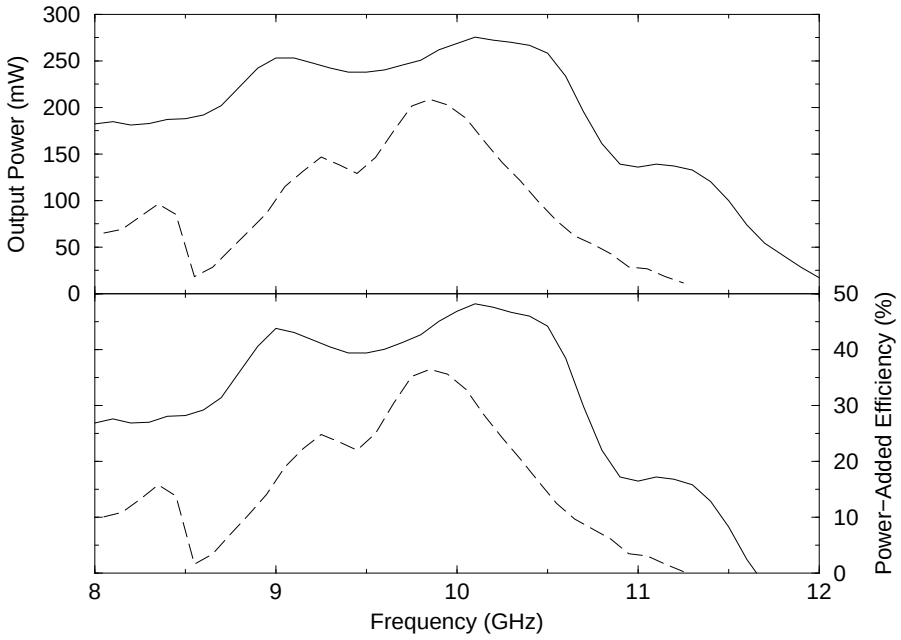


Figure 2.19. Measured output power and power-added efficiency as a function of frequency for the 10-GHz class-E (solid line) and class-A (dashed line) power amplifiers.

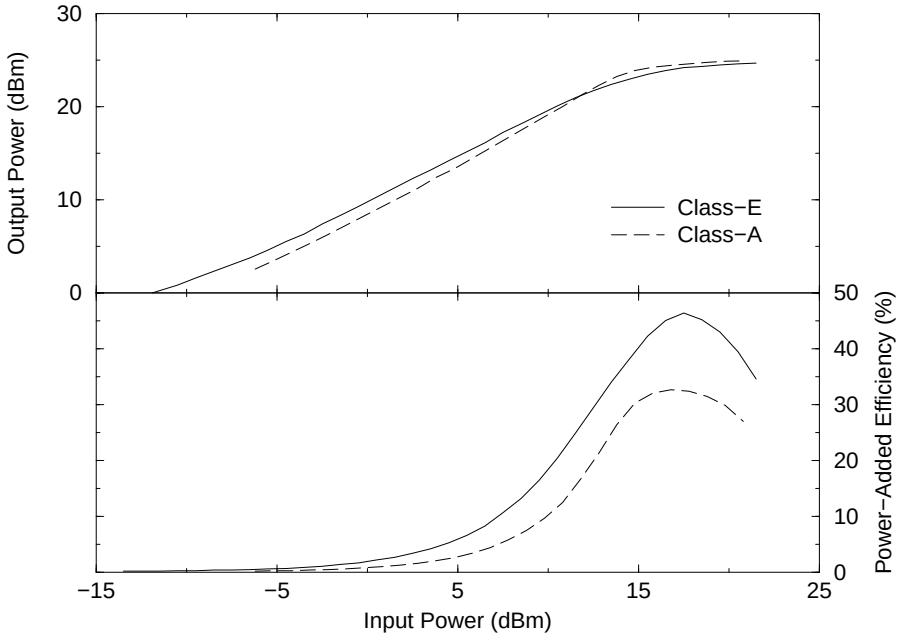


Figure 2.20. Measured output power and power-added efficiency as a function of input power for the 10-GHz class-E (solid line) and class-A (dashed line) power amplifiers.

# CHAPTER 3

# TIME-DOMAIN MEASUREMENTS OF SWITCHED-MODE MICROWAVE POWER AMPLIFIERS

## 3.1 Introduction

The ideal waveforms for class-E and class-F operation were shown in Chapter 2. In order to verify class-E and class-F operation in an actual amplifier, it would be useful to measure the waveforms at the switch and compare them to the ideal case. At low frequencies (up to about 500 MHz), these switch waveforms can be measured by introducing a large resistor between the drain and source and measuring the voltage across this resistor using an oscilloscope [4]. At higher frequencies it is not possible to measure these waveforms due to the difficulty in making high-impedance probes at these frequencies.

Another possibility is to use a nonlinear device model with a harmonic balance simulator to simulate the waveforms at the switch. This is in fact done here at 500 MHz using a Materka-Kacprzak model for the Siemens CLY5 MESFET. However, it has proven very difficult to obtain nonlinear transistor models that accurately characterize switched-mode operation at higher frequencies.

One verification of class-E or class-F performance is simply obtaining high efficiency. This, however, leaves an ambiguity in the proper operation of the circuit. Recent advancements in photoconductive probing of microwave circuits [30, 31] have paved a way to make such measurements up to very high frequencies.

Power and efficiency measurements of a 8.4-GHz class-F and a 8.35-GHz

class-E amplifier were presented in Section 2.4.4. In addition to power and efficiency measurements, these amplifiers were sent to the University of Michigan where photoconductive probing was done to look at the time-domain waveforms at key points in the circuit to verify class of operation.

## 3.2 Photoconductive Sampling Technique

The photoconductive probe utilized in the time-domain measurement of the high-efficiency amplifier response is a micromachined, optical-fiber-coupled, optoelectronic sampling head. It can sense the charge on an exposed interconnect or the field associated with a buried interconnect, acting as a 4-ps-resolution sampling gate and converting current signals into voltage signals.

The current to voltage conversion is accomplished by a JFET source follower circuit with an input resistance of 1 T$\Omega$ and an input capacitance of 3 pF. This high input resistance avoids charge drainage from the DUT so that measurement with minimal invasiveness is achieved. Due to the small amount of charge necessary to load the source follower input, the actual voltage level is built up in a short time, allowing a higher modulation bandwidth and the ability to measure absolute voltage levels. In addition, the high input resistance of the source follower allows the instantaneous dc voltage at the probe node to be determined at the output of the source follower, and thus both ac and dc signals can be measured simultaneously.

In this measurement system, shown in Fig. 3.1, the probe is illuminated by a train of femtosecond-duration laser pulses, and the output voltage is recorded on a low-frequency oscilloscope. The output voltage is a down-converted replica of the unknown microwave signal. If a frequency-domain output is required, a lock-in amplifier or a spectrum analyzer can be used in place of the oscilloscope. For an unknown microwave signal with frequency $f_m$, heterodyne mixing and equivalent time-sampling dictate that the following relationship between the microwave

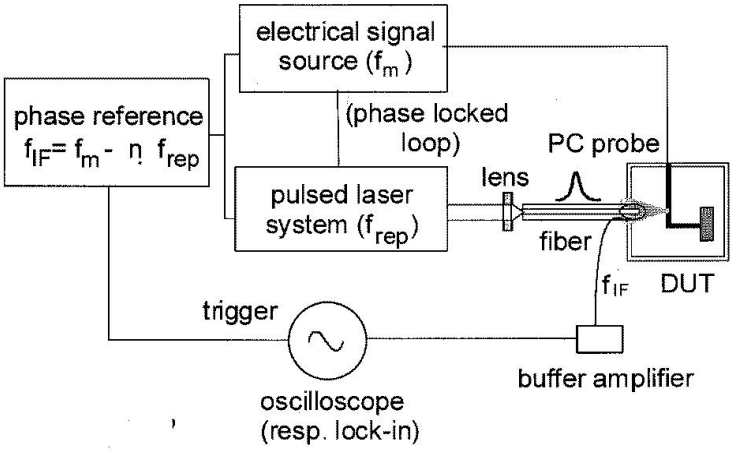


Figure 3.1: Photoconductive sampling measurement setup.

frequency and the intermediate frequency be fulfilled:

$$f_m = n f_{rep} \pm f_{IF}, \tag{3.1}$$

where $n$ is an integer and $f_{rep} = 80\,\text{MHz}$ is the laser pulse repetition frequency. The intermediate frequency $f_{IF}$ is typically in the kHz range and provides a replica of the unknown microwave signal. The Ti:sapphire laser used in this system is phase locked to the microwave source so that the in-circuit electrical signal can be determined in amplitude and phase. The probe has a 3.5 ps time response, which relates to a bandwidth over 100 GHz. Therefore, the probe should exhibit a frequency response which extends into the mm-wave region. [32]

### 3.3 Time-Domain Measurements

The two amplifiers are built on Rogers RT5880 Duroid substrates with $\epsilon_r = 2.2$ and 0.508 mm thickness. The general outline of the two amplifiers is shown in Fig. 3.2. The points at which the circuit is probed are shown as **A**, **B**, **C**, **D**, and **E** in this figure and correspond to the plots shown later in this chapter. The gate

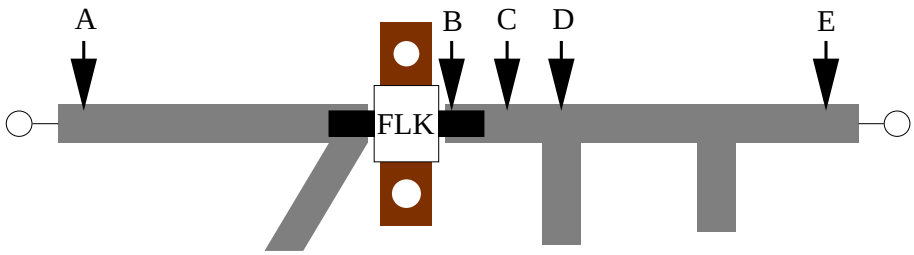


Figure 3.2. General outline of class-E and F amplifiers showing locations of photoconductive probing.

and drain gold leads were soldered to the rest of the circuit in such a manner as to leave an exposed gold area for the probe to make contact with.

**3.3.1 Class-F Amplifier** The switched-mode class-F amplifier was described in Chapter 2. The voltage waveform at the switch of an ideal class-F amplifier is a square wave. The voltage at the switch of this class-F amplifier should approach a square wave because the voltage contains negligible second harmonic content but significant third harmonic contribution. Higher-order harmonics were not considered in the design. Electrical measurements at 8.0 GHz show a drain efficiency of 73%, a power-added efficiency (PAE) of 61%, and 28.6 dBm output power. The input power was 22 dBm. Measurements as a function of frequency and input power are presented in Section 2.4.4. Harmonic balance simulations of the waveforms were not possible because a large-signal model for this transistor is not accurate at this freqeuncy.

The input waveform measured at point **A** in Fig. 3.2 is a sine wave biased at about -1.0 V, as is shown in Fig. 3.3. These waveforms cannot be used to calculate power since the local impedance is unknown. However, they are very useful in analyzing which harmonic components are contained in the waveform.

Fig. 3.4 shows the voltage waveform at point **B** in Fig. 3.2. The probe was placed on the gold output lead of the of the transistor, as close to the transistor as possible. Therefore, this waveform can be considered as the switch voltage variation

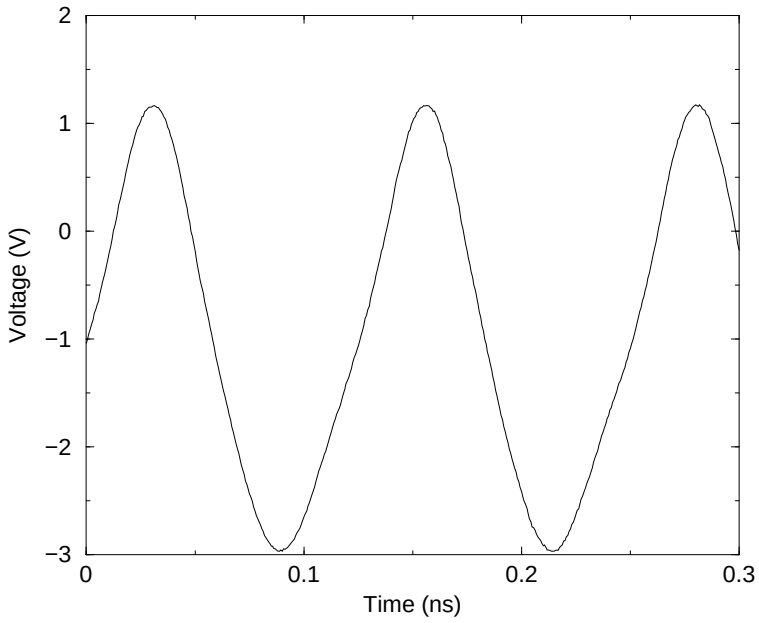


Figure 3.3: Measured waveform at point **A** in the class-F amplifier.

with time. Although the gold lead acts as a small inductance in series the switch, it is not significant enough to drastically change the switch waveform. Fig. 3.4 shows the square shape of the switch voltage, which is consistent with class-F operation. The two peaks in the waveform are due to the fundamental frequency and the third harmonic, as is evidenced by the spacing between peaks. The second harmonic does not appear in this waveform since it is presented with a short at the output. Higher harmonics are not clearly seen since the transistor does not have appreciable gain at these frequencies.

However, in Fig. 3.5, it is evident that there is a significant second harmonic contribution at point **C**. This is due to the standing wave between the transistor output and the first stub, which provides the second harmonic short.

As shown in Fig. 3.6, the second harmonic is not seen in the waveform at point **D**, since the open stub presents a short to the second harmonic here. The distortion in the waveform indicates that there is some third harmonic leakage beyond the first stub, which is to be expected since the third harmonic open was not explicitly

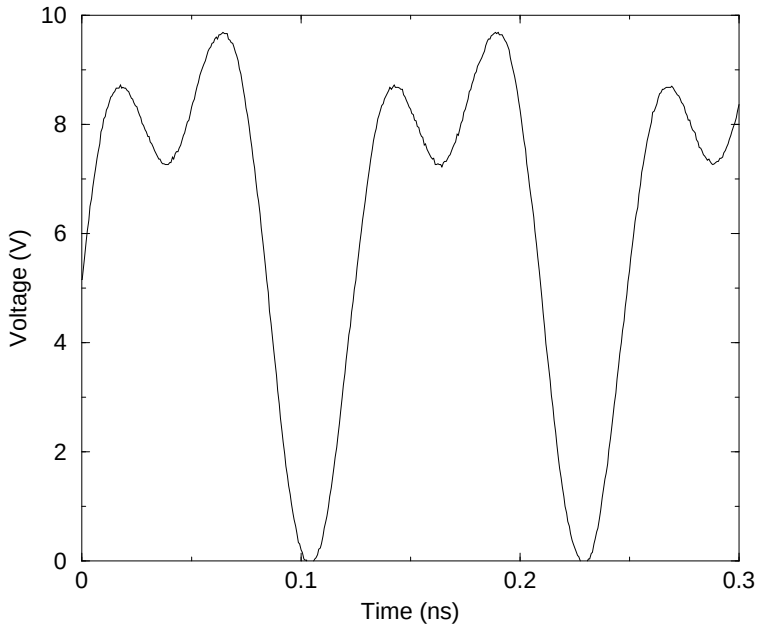


Figure 3.4: Measured waveform at point **B** in the class-F amplifier.

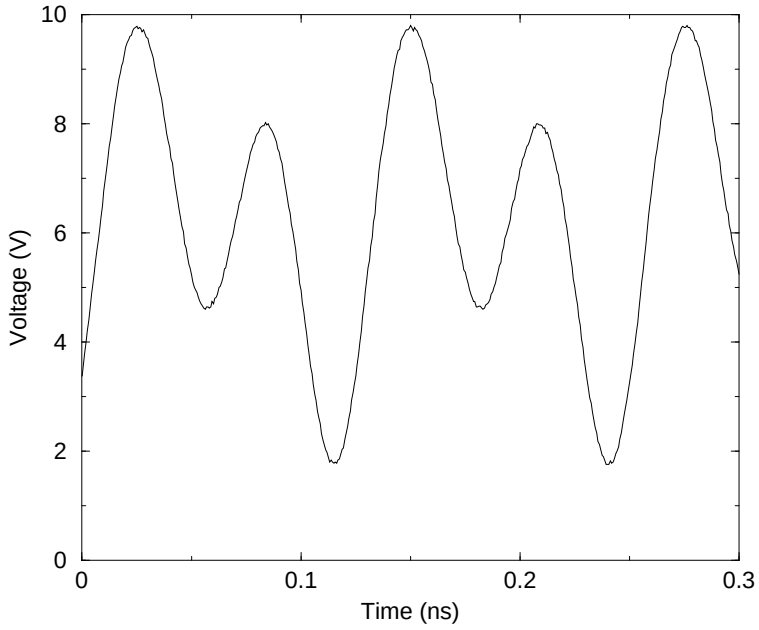


Figure 3.5: Measured waveform at point **C** in the class-F amplifier.

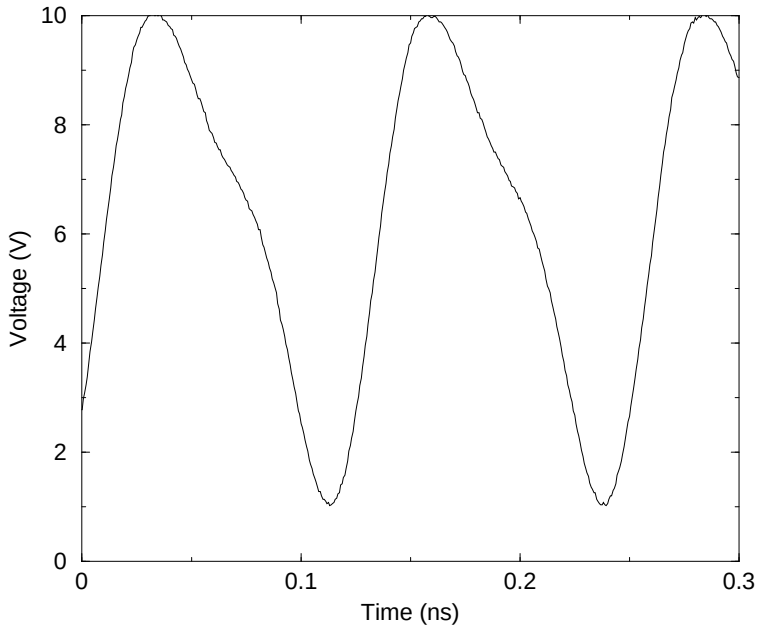


Figure 3.6: Measured waveform at point **D** in the class-F amplifier.

enforced.

Beyond the second output stub, at point **E**, the output waveform is sinusoidal. This is shown in Fig. 3.7. This verifies that by this point, the harmonics in the switch waveform have been filtered out.

**3.3.2 Class-E Amplifier** The switched-mode class-E amplifier was described in chapter 2. The lack of a large signal model for the FLK202 MESFET prohibits waveform simulations which would aid in the design of these circuits.

Electrical measurements indicate a drain efficiency of 64%, PAE of 48%, and 31.5 dBm output power at 8.35 GHz. Measurements as a function of frequency and input power were presented in Section 2.4.4. The photoconductive measurements were made at 8.32 GHz, since the microwave frequency must be a multiple of the laser repetition frequency of 80 MHz according to Eq. 3.1.

For the class-E circuit, only voltages at points **B** and **E** in Fig. 3.2 are shown, since they give the most insight into the operation of this amplifier. Fig. 3.8

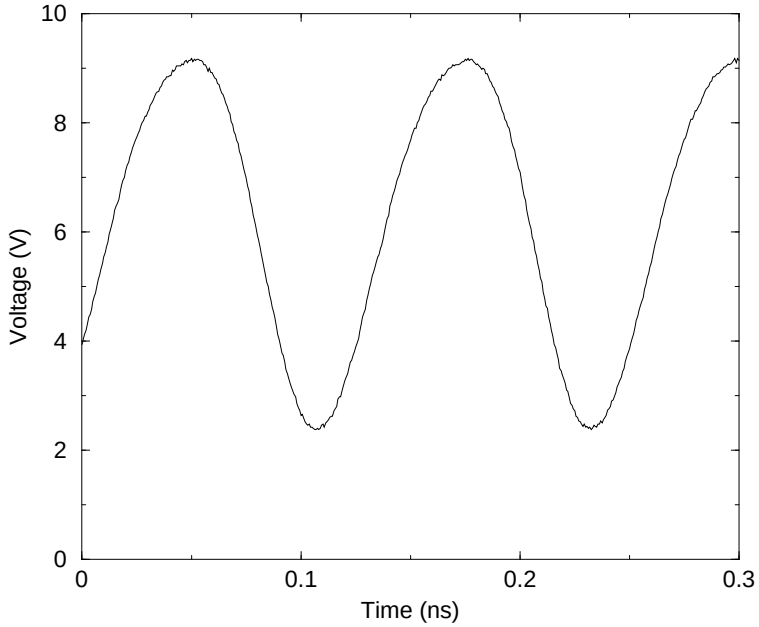


Figure 3.7: Measured waveform at point **E** in the class-F amplifier.

shows the voltage at point **B**, which is the voltage waveform across the switch. For comparison, a harmonic balance simulation at 500 MHz for a different class-E amplifier [3] is shown in Fig. 3.9. A suitable nonlinear model was available for this MESFET (Siemens CLY5). The switch voltage waveform in this case is not square, but a left-skewed raised cosine. The simulated voltage is close to zero for nearly half of the period, approaching ideal class-E operation. The measured voltage, however, is not flat in this half of the period, resulting in a higher voltage-current product (dissipated power) at the device. This is consistent with nonoptimal class-E operation, since the amplifier is operated above the critical frequency for class-E operation, about 1.5 GHz in this case. The measured waveform in Fig. 3.8 does have the same basic class-E shape of a left-skewed raised cosine. The measured class-E waveform is very different from the class-F switch voltage in Fig. 3.4 which depicts an approximate square wave.

At point **E**, the filtered output waveform is sinusoidal, as shown in Fig. 3.10.

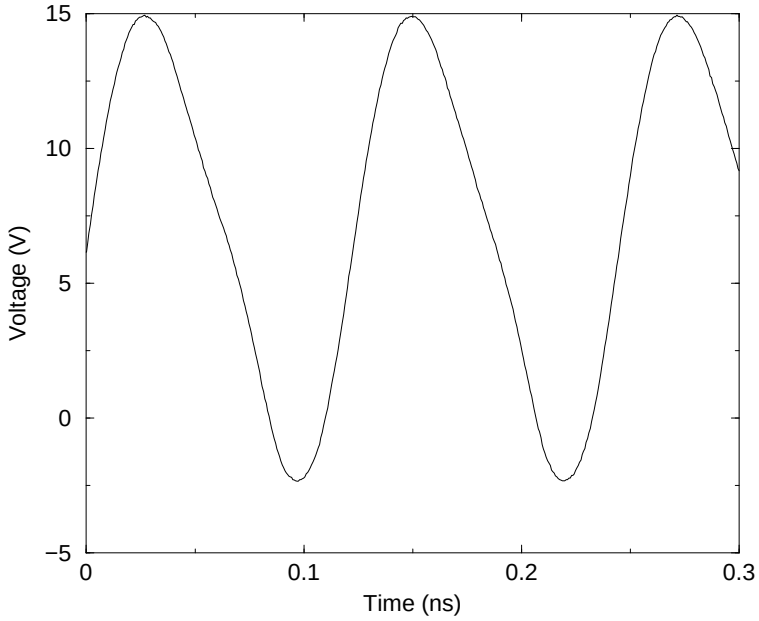


Figure 3.8: Measured waveform at point **B** in the class-E amplifier.

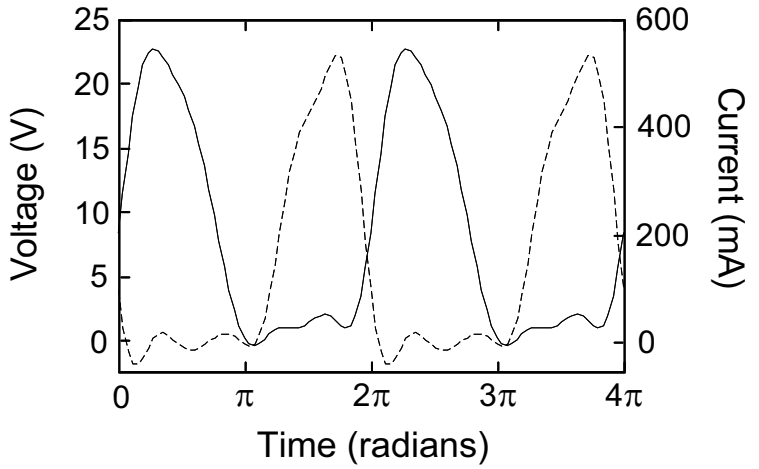


Figure 3.9. Simulated voltage (solid line) and current (dashed line) waveforms of a 500-MHz class-E amplifier using a Materka-Kacprzak nonlinear model for the Siemens CLY5 MESFET.

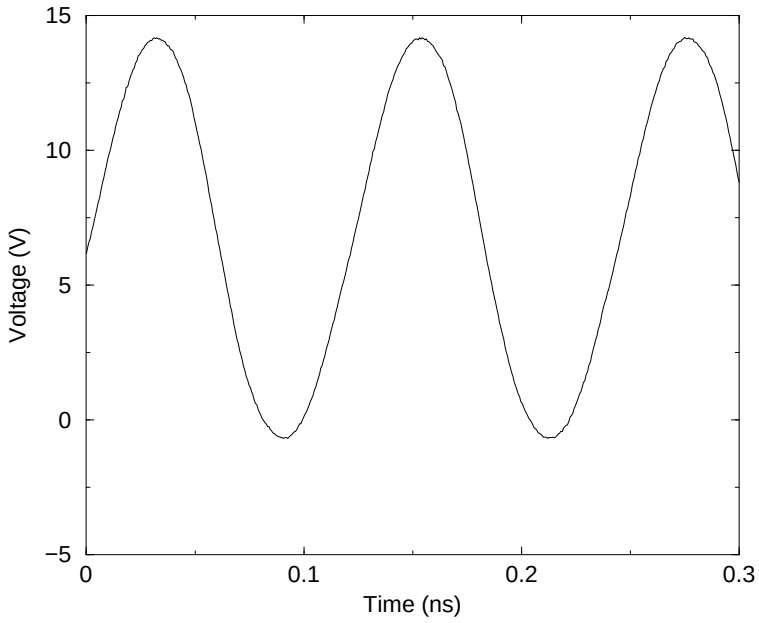


Figure 3.10: Measured waveform at point **E** in the class-E amplifier.

This shows that the harmonics of the switch waveform have been filtered out and the output is close to a pure sine wave.

## 3.4 Conclusion

Time-domain measurements of the 8.4-GHz class-F amplifier at the output of the MESFET show the approximation of a square wave predicted by the shorting of the second harmonic. Time-domain measurements of the 8.35-GHz class-E amplifier show a waveform at the MESFET output indicative of class-E operation.

The photoconductive probing technique described in this chapter was shown to be an effective tool for measuring the time-domain waveforms of microwave power amplifiers at various points in the circuit. This is important for verifying correct operation of switched-mode amplifiers. It also allows the designer to determine places where further harmonic tuning might be of the most benefit.

# CHAPTER 4

# SPATIAL COMBINING OF HIGH-EFFICIENCY POWER AMPLIFIERS

## 4.1 Introduction

In order to obtain the necessary power levels (tens of watts) for many commercial and military millimeter-wave applications, the powers of several solid-state devices must be efficiently combined. At millimeter-waves, circuit based combining schemes [33] suffer from higher transmission losses which increase with the number of elements. Spatial power combining promises the low-loss combining of hundreds or more elements.

In this chapter, X-band class-F power amplifiers presented in Chapter 2 are incorporated into spatial power combiners. First, a comparison of power combining methods is given. The definition of power combining efficiency is then discussed, especially as it applies to spatial power combiners. Feeding of spatial combiners is also discussed. Design, measurement, and analysis are then described for a 9-element passive, 9-element active, and a 36-element active X-band spatial power combiner.

## 4.2 Methods of Power Combining

There are two basic methods of power combining: internal (or chip-level) and external. The latter includes methods such as circuit corporate and spatial power combiners. At the device level, the gate periphery can be enlarged to increase the power potential of the individual device at the expense of gain and efficiency. Alternatively, smaller and more efficient amplifiers can be combined externally (off-chip).

Both internal and external power combining can be used together. For instance, ten 1-mm MESFETs can be circuit combined instead of twenty 0.5-mm devices for the same output power.

Design and measurements of a 8.4-GHz class-F amplifier using the Fujitsu FLK052WG MESFET and a 8.4-GHz class-E amplifier using the Fujitsu FLK202 MESFET were described in Section 2.4.4. These measurements are used in this section for a comparison of power combining techniques. The FLK052 and the FLK202 have the same intrinsic structure, but the periphery of the FLK202 is four times larger [34]. They are both packaged devices.

**4.2.1 Chip-Level Power Combining** Considering that the FLK202 is physically four times larger than the FLK052, the output power might be expected to be four times larger as well. However, in the most efficient amplifier, the supplied dc power is not necessarily four times larger for the FLK202. It is therefore more appropiate to define the chip-level power-combining efficiency ($\mathrm{PCE_{chip}}$) as the ratio of the *overall efficiency* of the FLK202 amplifier to that of the FLK052 amplifier,

$$\mathrm{PCE_{chip}} = \frac{\eta_{\mathrm{amp,202}}}{\eta_{\mathrm{amp,052}}}, \tag{4.1}$$

In order to accurately calculate $\mathrm{PCE_{chip}}$ for the FLK202 MESFET, both devices should be used in a power amplifier that yields the highest possible efficiency at a given frequency and bias point. It was found experimentally that, around 8 GHz, the FLK052 gave the best overall efficiency in a class-F amplifier and the FLK202 gave the best overall efficiency in a class-E amplifier, while maintaining high output power.

Frequency and power sweep measurements of these amplifiers are given in Section 2.4.4. Table 4.1 shows the best performance of each amplifier. The FLK052 class-F amplifier has a high overall efficiency at 8.4 GHz of 64% with 685 mW output power. The FLK202 class-E amplifier has a high overall efficiency at 8.35 GHz of

| Device | $P_{in}$ | $P_{out}$ | Gain | $\eta_{amp}$ | $P_{heat}$ |
|---|---|---|---|---|---|
| FLK202 | 500 mW | 1.700 W | 5.3 dB | 57% | 1.300 W |
| FLK052 | 125 mW | 685 mW | 7.4 dB | 64% | 391 mW |

Table 4.1. Summary of measurements for the class-F power amplifier using the FLK052 and the class-E power amplifier using the four-times larger FLK202. $P_{heat}$ is the power dissipated as heat.

57% with 1.7 W output power. From Eq. 4.1, the chip-level PCE of the FLK202 is 89%.

There is, however, a limit to the size of the chip. As the gate periphery increases, the input impedance decreases, making the device more difficult to match and decreasing the bandwidth. The largest MESFET that Fujitsu makes in this series is only 25% larger than the FLK202.

**4.2.2 Circuit Level Power Combining** In a circuit corporate combiner, shown in Fig. 4.1, the outputs from each amplifier are successively combined using two-way adders such as Wilkinson combiners. Table 4.2 shows a comparison, for the same input power, between the circuit corporate combining of four FLK202 amplifiers and sixteen FLK052 amplifiers for 0.2 dB loss per stage. To find the overall efficiency of the entire system ($\eta$), the overall efficiency of the amplifier ($\eta_{amp}$) is multiplied by the power-combining efficiency of the combining network ($PCE_{ckt}$), given by

$$PCE_{ckt} = 10^{-n\frac{L}{10}}, \tag{4.2}$$

where L is the loss per stage in dB and n is the number of stages. The total number of elements, N, is $2^n$. Even for a low-loss combiner (0.2 dB loss), the overall efficiencies are approximately equal, but it would be less complex and use less space to combine the four larger FLK202 amplifiers.

**4.2.3 Spatial Power Combining** Spatial, or *quasi-optical*, power combining, shown in Fig. 4.2, eliminates the need for complicated and lossy corporate networks. In this approach, the output of each amplifier is connected to an antenna.

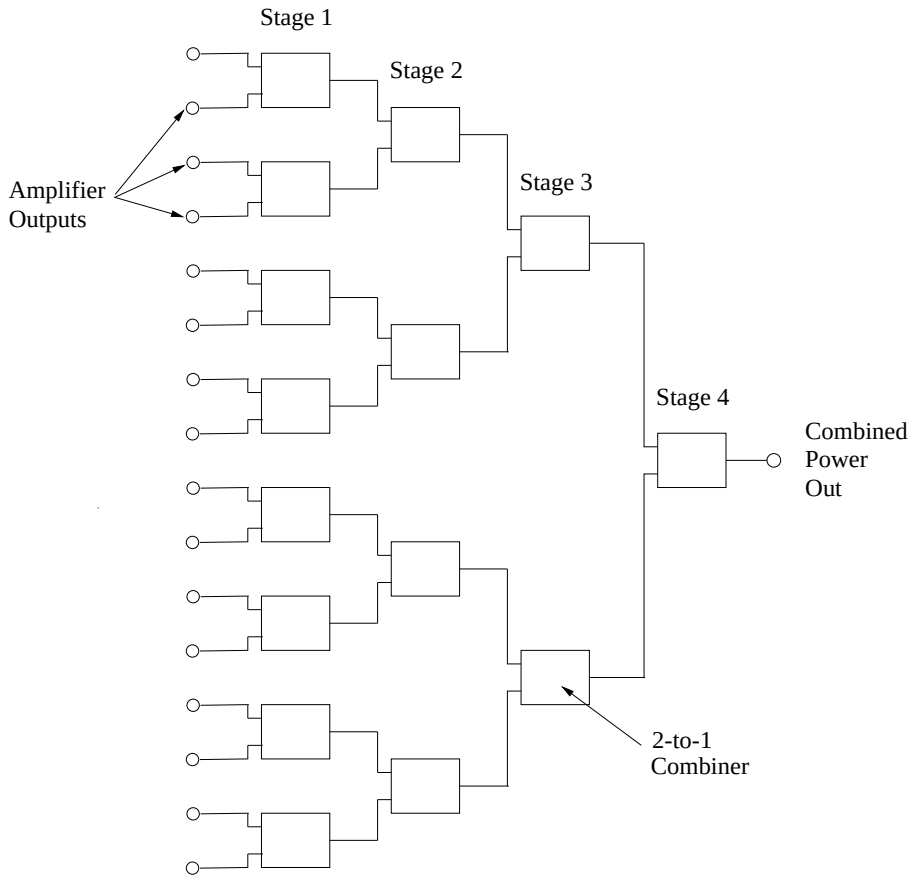


Figure 4.1. A circuit corporate power combiner. The output of an amplifier is connected to each circle.

| Device | N | $\eta_{amp}$ | Stages | $PCE_{ckt}$ | $P_{out}$ | $\eta$ | $P_{heat}$ |
|---|---|---|---|---|---|---|---|
| FLK202 | 16 | 57% | 4 | 83% | 22.6 W | 47% | 25.5 W |
| FLK052 | 64 | 64% | 6 | 76% | 33.3 W | 49% | 34.7 W |

Table 4.2. This table compares, for the same input power (8 W), chip-level combining versus circuit combining for a corporate combiner with 0.2 dB loss per stage. $\eta_{amp}$ is the overall efficiency of the amplifier, $PCE_{ckt}$ is the power-combining efficiency of the corporate network, and $\eta$ is the overall efficiency of the entire system. $P_{heat}$ is the total power dissipated as heat in the system.

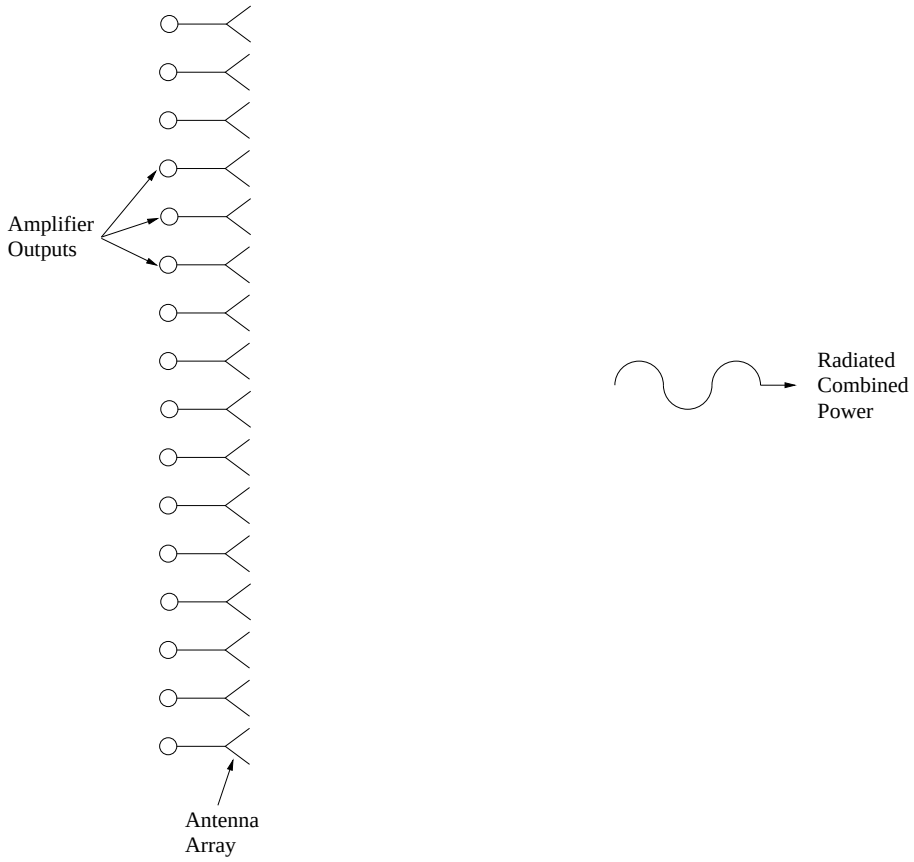


Figure 4.2. A spatial power combiner. The output of an amplifier is connected to each circle.

The powers from all the devices are thus coherently combined in free space in a single stage. The power-combining efficiency should therefore be independent of the number of elements.

This approach was first demonstrated in 1968 with a 100-element array at 410 MHz [35]. Other examples include a 8-element 20-Watt spatial combiner with 50% combining efficiency using a waveguide-based spatial combiner [36], a Ka-Band free-space power combiner with 0.7 W output power [37], a monolithic 112-element Ka-Band quasi-optic amplifier [38], and a 45-GHz circuit-fed spatial combiner with 48.3 dBm EIRP and 46% combining efficiency [39]. A survey of spatial power combining techniques can be found in [1].

| Device | N | $\eta_{AMP}$ | $P_{out}$ | $\eta$ | $P_{heat}$ | Area | Heat Flux | D | EIRP |
|---|---|---|---|---|---|---|---|---|---|
| FLK202 | 16 | 57% | 20.4 W | 43% | 27.0 W | 131 $cm^2$ | 207 $\frac{mW}{cm^2}$ | 21.1 dB | 2.63 kW |
| FLK052 | 64 | 64% | 32.9 W | 48% | 35.6 W | 522.4 $cm^2$ | 68 $\frac{mW}{cm^2}$ | 27.1 dB | 16.9 kW |

Table 4.3. This table compares, for the same input power (8 W), the spatial power combining of 16 FLK202 amplifiers and 64 FLK052 amplifiers. The area assumes a unit cell size of 0.8$\lambda$ x 0.8$\lambda$. The directivity, D, assumes an effective area equal to the physical area. $P_{heat}$ is the total power dissipated as heat in the system.

Table 4.3 shows a comparison between spatially combining four FLK202 amplifiers and sixteen FLK052 amplifiers. The overall efficiency of the entire system is $\eta_{amp}$ times the PCE of the spatial combiner ($PCE_{spc}$). A value of 75% is assumed for $PCE_{spc}$. This includes the radiation efficiency of the antennas. $P_{out}$ is equal to the output power from each amplifier multiplied by $N \cdot PCE_{spc}$. The area of the combining array assumes a unit cell size of 0.8$\lambda$ x 0.8$\lambda$, and is therefore equal to $0.64 \cdot N\lambda^2$. The directivity, D, assumes an effective area equal to the physical area and is therefore equal to $\frac{4\pi}{\lambda^2} \cdot$Area. The effective isotropic radiated power (EIRP) is the directivity multiplied by $P_{out}$.

Since the power-combining efficiency is independent of the number of elements, it is more efficient in a spatial combiner to use a larger number of smaller amplifiers, if space is not an issue. In addition, a larger array has a higher directivity, so the effective isotropic radiated power (EIRP) is also higher. Thermal management also becomes easier if a larger numbers of smaller devices are used, since the heat flux is much less.

In order to compare circuit to spatial combining, an antenna should be placed at the output of the circuit combiner. Assuming that the choice of antenna is not constrained by size or substrate considerations, unlike the spatial combiner, this antenna can be close to 100% efficient. A comparison of circuit combining to spatial combining shows that for 0.2 dB loss per stage, a circuit combiner with more than six stages (64 elements) will have a lower PCE than the 75% spatial combiner.

## 4.3 Definition of Power Combining Efficiency

There has been a tendency in the literature regarding quasioptic power amplifiers to use different definitions for output power and combining efficiency. This makes comparison of results very difficult. Gouker has proposed standard definitions of figures of merit for quasioptic amplifiers [40].

The only unambiguous figure for a spatial power combiner is the effective isotropic radiated power (EIRP), since it depends only on the recieved power, $P_r$, the gain of the receive antenna, $G_r$, and the distance from the array to the receive antenna, R:

$$EIRP = P_t G_t = \frac{P_r}{G_r}(\frac{4\pi R}{\lambda})^2 \tag{4.3}$$

However, determining the transmitted power, $P_t$, requires knowledge of the antenna gain for the array, $G_t$. The antenna gain for the array, unfortunately, is difficult to determine, without knowing the antenna losses and integrating several cuts of both the measured copolarized and cross-polarized radiation patterns. Gouker proposed an alternative figure, the *effective transmitter power* ($P_{eff}$), defined as

$$P_{eff} = \frac{EIRP}{D_t}, \tag{4.4}$$

where $D_t$ is the directivity assuming a lossless array, i.e.

$$D_t = \frac{4\pi A}{\lambda^2}, \tag{4.5}$$

where A is the physical area of the array. This definition accounts for all losses in the antenna and losses due to nonuniform phase and amplitude distribution across the surface of the array.

The combining efficiency is based on this effective transmitter power:

$$PCE = \frac{P_{eff}}{\sum_{i=1}^{n} P_{i,avail}} \tag{4.6}$$

$P_{i,avail}$ is the maximum available power from the $i^{th}$ active device when presented with its optimum load impedance. However, the point of maximum power does not

correspond to the point of maximum efficiency. So the definition of $P_{i,avail}$ could be amended to be the output power when the device is operating at maximum efficiency. However, as will be shown later, if a constrained lens feed is used, not all of the elements are equally saturated, and therefore at the point of highest efficiency. An alternative definition is to use the maximum available power for each element based on its predicted input power. This still does not take into account changes in bias due to mutual coupling of array elements for instance, or as with the comparison made in Section 4.2.1, different classes of operation.

To include the effect of different bias conditions, PCE can be defined in terms of overall efficiency:

$$\mathrm{PCE} = \frac{\eta}{\eta_{\mathrm{amp}}}, \tag{4.7}$$

where $\eta_{\mathrm{amp}}$ is the maximum overall efficiency of a single element. To calibrate out the effect of a nonuniform input power distribution, $\eta_{\mathrm{amp}}$ can be defined as the average overall efficiency of each element at the input power it is operating at in the array.

## 4.4 Feeding of Spatial Combiner

Just as there can be circuit or spatial combining, there can be circuit or spatial feeding. A corporate feeding structure like the combining structure in Fig. 4.1 can be used for the feed. This is the approach taken for the 45-GHz spatial combiner in [39]. Like circuit combining, this approach has the same problem that loss increases with number of elements. The advantage of a spatial feed over a circuit feed is that the feed loss should be independent of the number of elements.

A spatial feed can be realized in a few different ways. The feed antenna can simply be placed in the far field of the array, so the array is presented with a plane wave [41], [42], [37], [3]. However, this results in a large fraction of the power being diffracted over the edges of the array. The feed antenna can be moved closer to the array and dielectric lenses used to create a gaussian beam [43]. The array is

placed at the beamwaist, giving a uniform phase distribution. Also, a "hard horn" feed can be used where a horn antenna is designed using dielectric inserts to have a near uniform aperture field distribution [44]. A hard-horn feed was used at Ka-band in [45] with less than 2 dB feed loss for 138 elements. This is roughly equivalent to a circuit corporate feed with less than 0.3 dB per stage.

The approach used in this chapter is to design the array to be a constrained lens. The constrained lens is based on the Rotman lens [46]. A planar constrained lens design using microstrip transmission lines was suggested by McGrath [47]. A thorough treatment of the history and application of constrained lenses, along with design equations, is given in [48]. Hollung [49] calulated the feed loss as a function of the *f*-number (F/D) for feed antennas of different directivities using both geometric optics and Friis transmission formula methods.

In a constrained lens, delay lines for each element convert an incident spherical phasefront to a uniform phase distribution at the output. The design assumes the incident wave has a spherical equiphase surface, i.e. the field is emanating from a point source. Typical feed antennas include horns and patches, neither of which are point sources. But the field can be treated as if it were emanating from a point given by the phase center of the feed antenna.

The E-plane horn antenna is predominately used to feed the arrays in this chapter. The phase center of this antenna occurs somewhere behind the aperture and can be calculated based on the aperture field distribution [50]. However, the phase center is different for the E- and H-planes. And outside a certain angular range, the equiphase surface can no longer be regarded as spherical. Therefore, the best feed position is usually determined experimentally.

The close proximity of the feed results in a nonuniform amplitude distribution at the surface of the array. For low F/D ($<0.4$), this factor dominates the feed loss. (The dominant loss mechanism for large values of F/D is spillover loss.) For

an array of power amplifiers, this nonuniform ampliude distribution results in the center elements being more saturated than the edge elements. The effects of this are described in the next section.

## 4.5 X-Band Spatial Power Combiners

9-element and 36-element spatial power combining arrays were designed, fabricated, and measured to investigate the factors that contribute to combining loss in these arrays. Also, by buiding and testing different sizes of combiners, the assertion that combining efficiency remains constant with number of elements can be verified.

A passive and active 9-element array and a 36-element active array were designed, fabricated, and measured. The active arrays use the 8.4-GHz class-F amplifier described in Section 2.4.4.

**4.5.1 Antenna Design** Microstrip patch antennas were chosen to be the radiating elements. The patch antenna was designed to have a 50-$\Omega$ input impedance at 8.40 GHz to overlap with the optimum frequency of the amplifiers. The layout of the patch is shown in Fig. 4.3. The return loss of the patch was measured versus frequency and compared to the simulated return loss in Fig. 4.4. The simulations, performed using *Zeland*, gave a directivity of 7.6 dB, efficiency of 83%, and gain of 6.8 dB.

**4.5.2 Array Design** The arrays are designed to be constrained lenses and fed from a focal point. Both the 9-element and 36-elements arrays have a F/D ratio of 0.87. As discussed in Section 4.4, the input power distribution across the surface of the array is not uniform. In Fig. 4.5, the input powers to each element are calculated for both the 9-element and 36-element arrays. The input power can vary by almost 6 dB from the center to the corner elements. These numbers were calculated by taking into account path length difference, directivity of feed horn, and

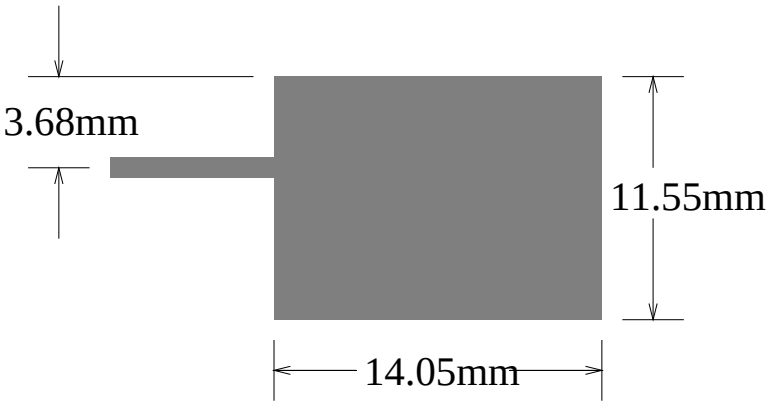


Figure 4.3. Layout of patch antenna for arrays. Substrate is Rogers RT5880 ($\epsilon_r$=2.2 and h=0.508 mm). The feed line has a characteristic impedance of 50 Ω (w=1.6 mm).

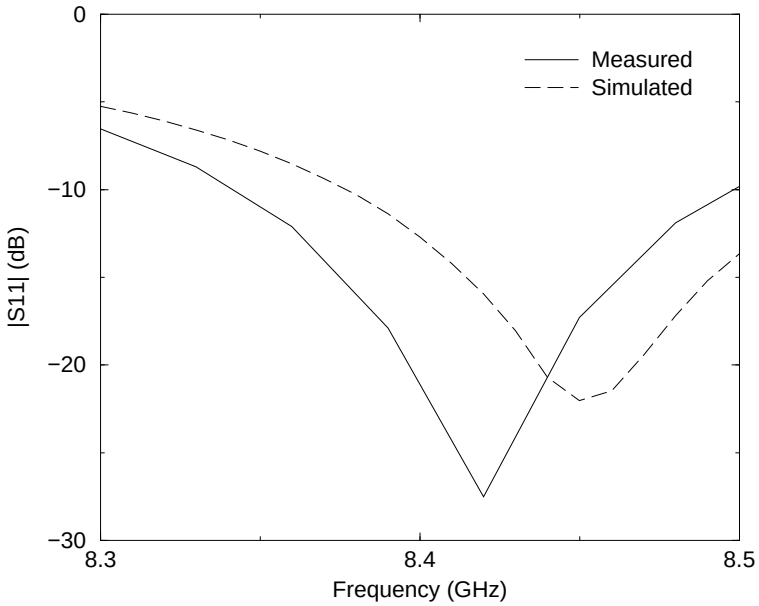


Figure 4.4. Measured (solid line) and simulated (dashed line) return loss versus frequency for the patch antenna used in the arrays. Simulation is performed using *Zeland*.

directivity of patch antenna for the angle from that element to the feed.

The calculated feed loss, summing the power received by each element and comparing to the power transmitted by the feed, is 6.6 dB for the 9-element array and 7.6 dB for the 36-element array. The unit cell spacing for these arrays is 30.35 mm by 30.35 mm square, or $0.85\,\lambda$ by $0.85\,\lambda$. This gives an approximate directivity, assuming uniform amplitude and phase distribution at the output, of 19.12 dB and 25.12 dB for the 9- and 36-element arrays respectively.

The feed and transmit arrays are on separate substrates (both are Rogers RT5880 duroid). These layers are separated by a layer of 62-mil thick FR4 for mechanical stability. Nylon screws spaced a unitcell apart fasten all the layers together. A rectangle is cut out of the FR4 to make room for the MESFETs and their soldering to ground. The vias from the feed side to the transmit side are described in Section 4.5.4. A drawing of the active unitcell is shown in Fig. 4.6.

**4.5.3 Amplifier Repeatability** To maintain uniform phase distribution across the output of the array, it is important that the amplifiers are uniform. The mounting and soldering of the MESFETs needs to be a repeatable process. To test the repeatability of the fabrication procedure and the uniformity of the devices, three 8.4 GHz class-F amplifiers were built using three different devices (two from the same lot, one from another). The measured output power and phase are shown in Fig. 4.7 versus input power. The phases of all three amplifiers remain within 15° of one another in the entire range. As expected for MESFETs, the phase increases as the devices are saturated. It is conceivable to account for the phase change in saturation by adjusting the delay line lengths based on the calculated input power for each element (as shown in Fig. 4.5). The maximum error for this effect is less than 10° and therefore less than fabrication and device tolerances.

**4.5.4 Via Repeatability** The vias are built using 1.6 mm brass rods. The holes for the via are drilled to be 1.5 mm in diameter giving a friction fit. Each

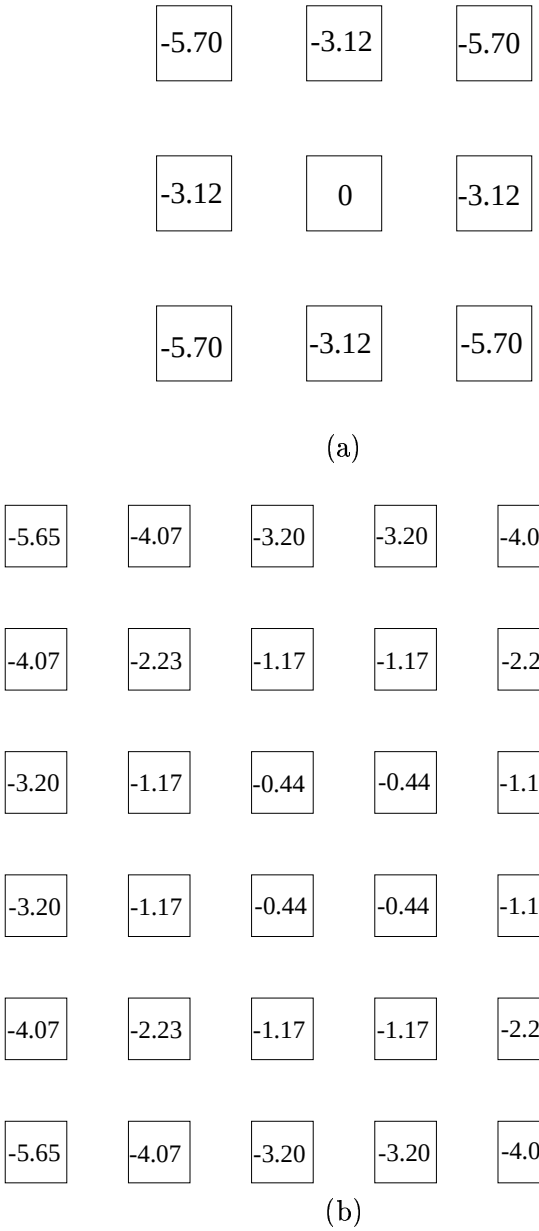


Figure 4.5. Calculated input power distribution across the surface of the 9-element(a) and 36-element (b) arrays (F/D=0.87). The feed is a E-plane horn antenna. Numbers are given in dB relative to power received at center of array.

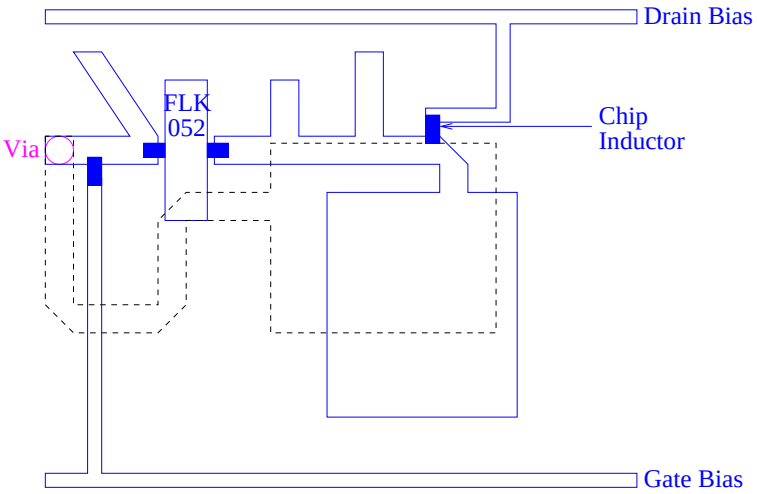


Figure 4.6. Drawing of receive (dashed line) and transmit (solid line) sides of active unitcell.

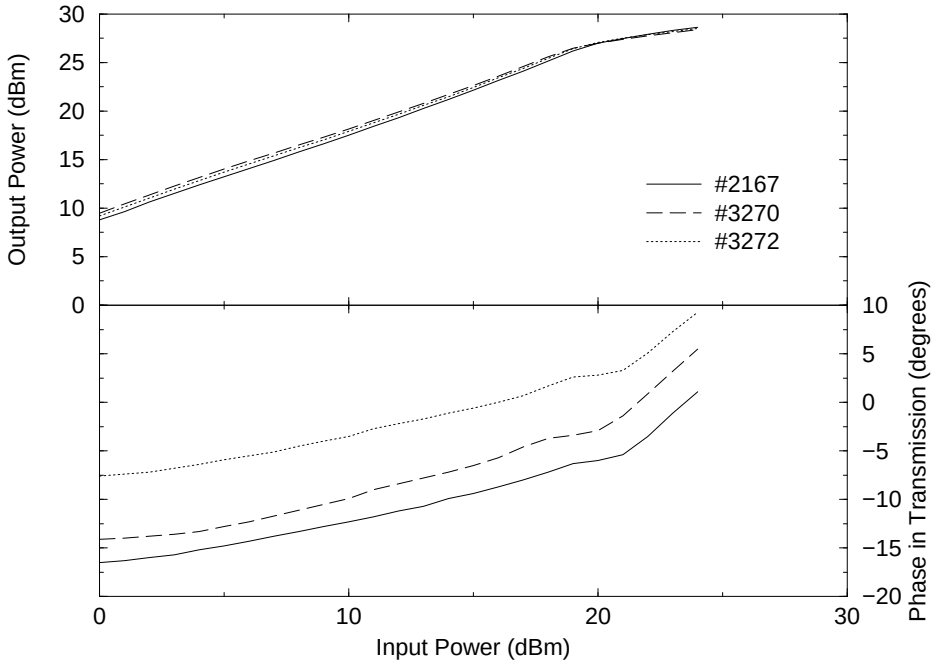


Figure 4.7. Output power and phase versus input power for identical amplifiers using three Fujitsu FLK052WG MESFETs with different serial numbers.

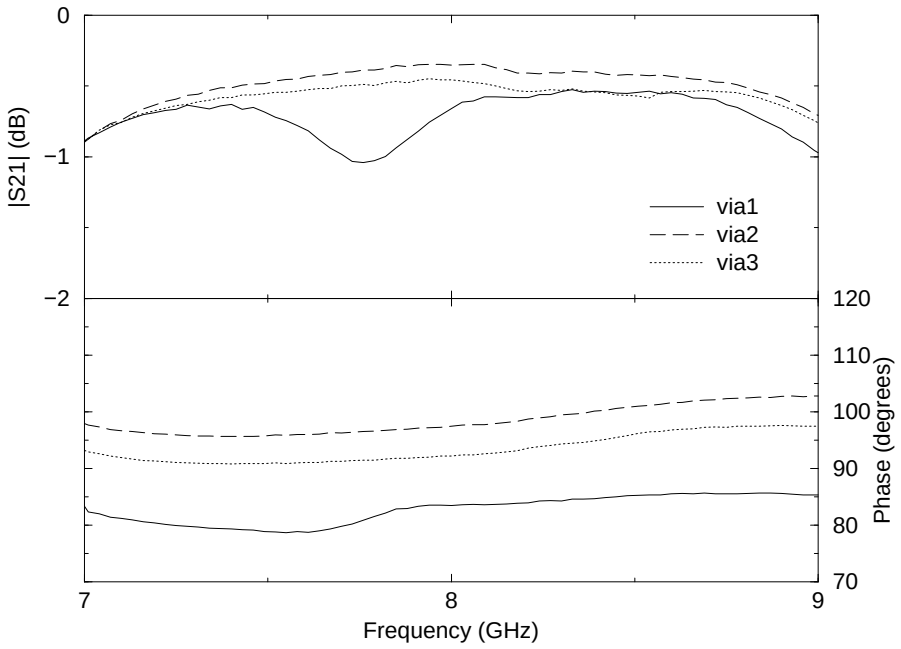


Figure 4.8: Magnitude and phase of $S_{21}$ for three vias identically made.

end of the rod is cut and smoothed off level with the microstrip line, where it is then soldered to the line. A 3 mm x 3 mm square is milled out of the ground plane of both duroid layers to prevent any possibility of shorting the via. A 3 mm-diameter hole is drilled in the FR4 layer for the via to pass through. To test the repeatability of this procedure, especially regarding phase, three identical circuits were made–a line on each side and the aforementioned via connecting each side. Fig. 4.8 shows the measurement of these vias versus frequency. The measured through loss at 8.4 GHz is 0.5 dB and the phase is within 20° of one another.

**4.5.5 Passive 9-Element Array** To verify that the array acts like a constrained lens, a 9-element passive array was built and measured. The feed side is shown in Fig. 4.9(a) and the transmit side is shown in Fig. 4.9(b). The amplifier circuitry is replaced by a microstrip through line. The lens is designed to have a F/D of 0.87 and therefore fed from a focal point 75 mm from the array.

Fig. 4.10 shows the received power in the far field as a function of the

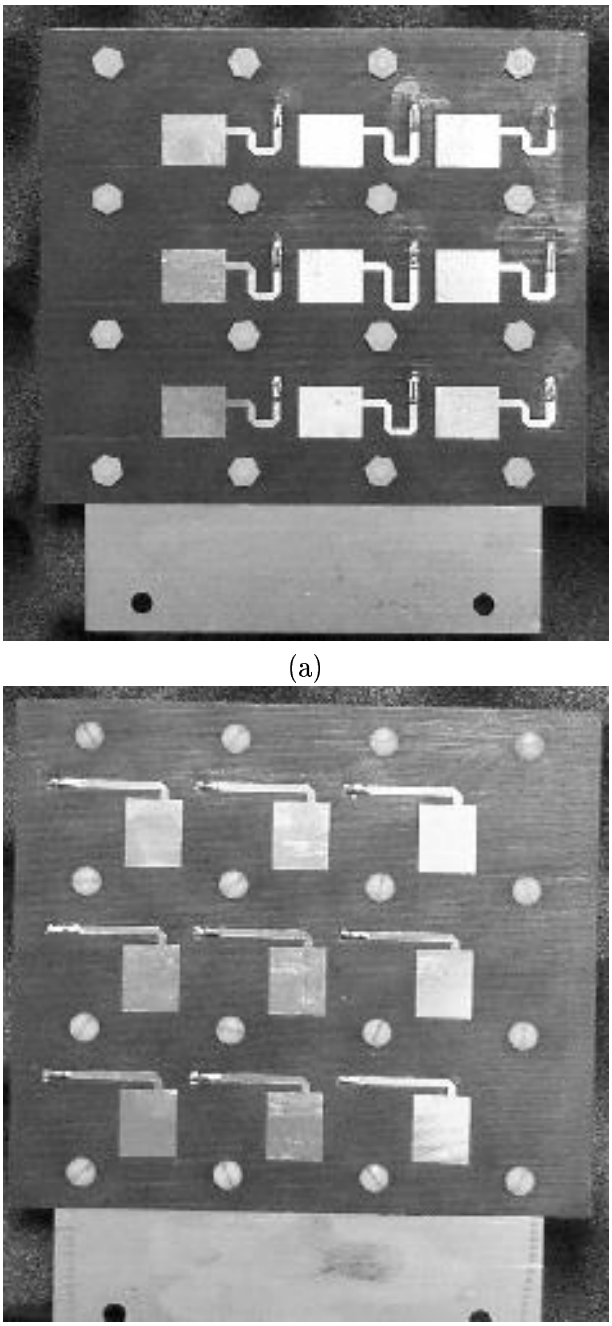

(a)

(b)

Figure 4.9. Picture of the feed side (a) and transmit side (b) of the 9-element passive array.

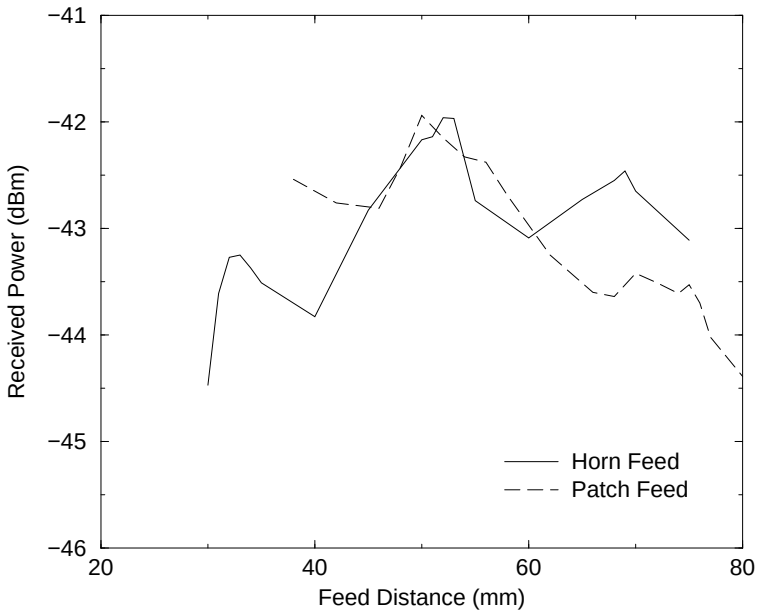


Figure 4.10. Recevied power versus feed distance for the 9-element passive array for both feeding with E-plane horn (solid line) and patch (dashed line).

distance from the feed to the array for both a E-plane horn and patch antenna feed. This distance is measured from the surface of the array to the surface of the patch or in the case of the E-plane horn, to the plane of the aperture. The maximum EIRP occurs at a feed distance of about 50 mm. As mentioned in Section 4.4, the phase center of the E-plane horn is somewhere behind the aperture.

Fig. 4.11 shows the measured co- and cross-polarized radiation patterns for both the E- and H-plane, as well as calculated copolarized patterns. The calculated pattern was found by multiplying the calculated array factor (using the amplitude distribution shown in Fig. 4.5(a)) with the measured pattern of the patch. Larger sidelobes are seen in the meaurement. However, agreement with calculation is close enough to verify that the array is focusing reasonably well. The difference does indicate, though, that there is some possible decrease in directivity from the optimum case assuming 100% aperture efficiency (19.12 dB).

The total loss, defined as the effective transmitter power (Eq. 4.4) divided

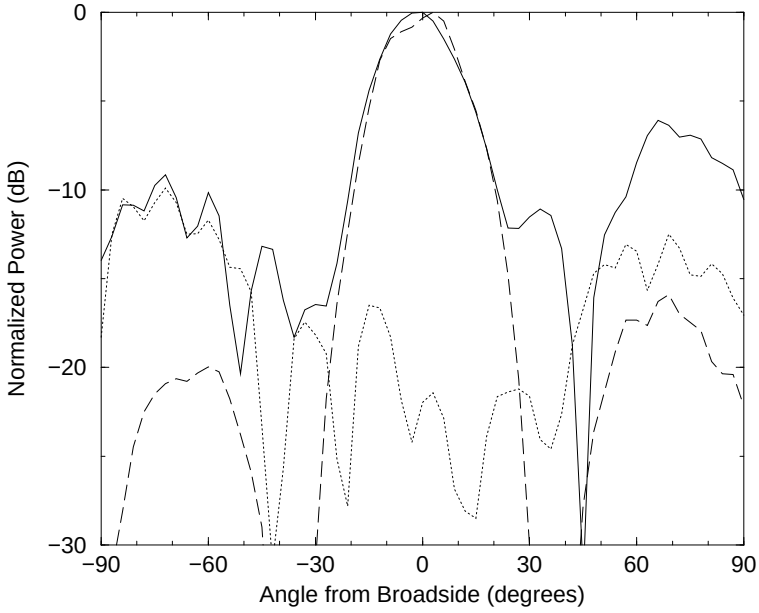


(a)

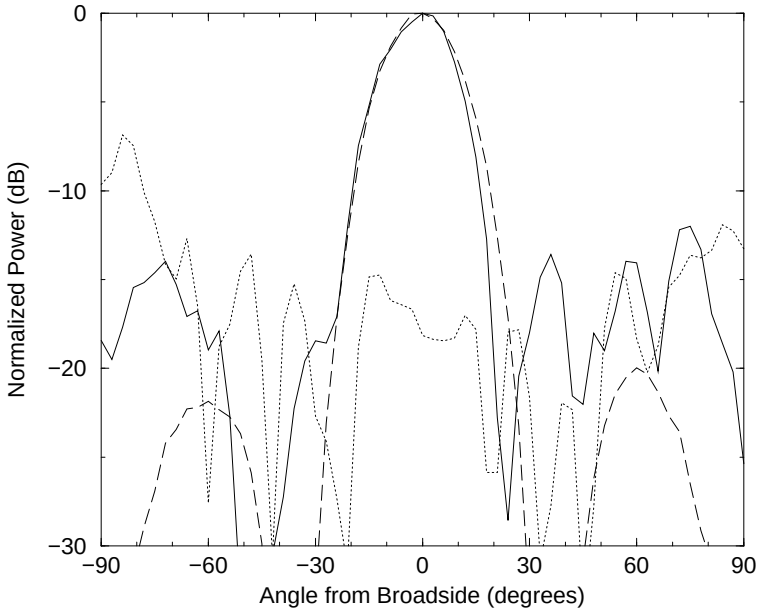


(b)

Figure 4.11. Measured copolarized (solid line), calculated copolarized (dashed line), and measured cross-polarized (dotted line) radiation patterns for the E-plane (a) and H-plane (b) of the 9-element passive array.

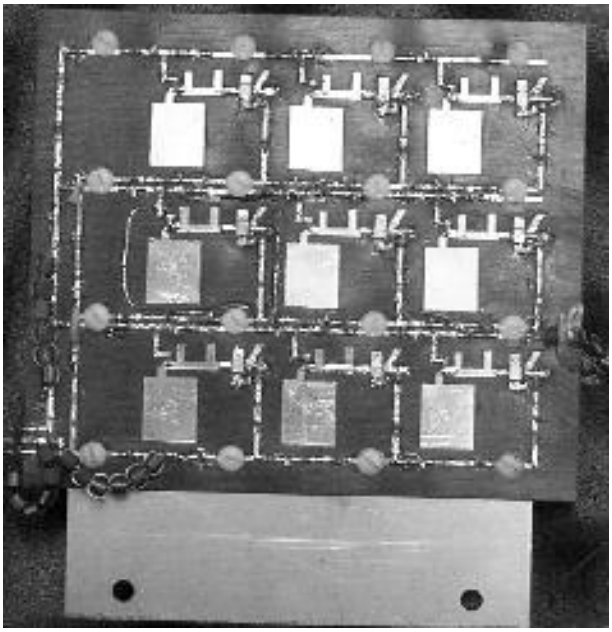

Figure 4.12: Picture of the transmit side of the 9-element active array.

by the power radiated by the feed horn, is 7.5 dB. Of this, 0.8 dB can be attributed to the efficiency of the output antenna and should therefore be considered combining loss. The difference, 6.7 dB, should be considered the feed loss. This agrees well with the 6.6 dB value calculated in Section 4.5.2 based on the Friis transmission formula.

**4.5.6 Active 9-Element Array** An active verson of the 9-element array was fabricated by replacing the through line of the passive array with the amplifier described in Section 2.4.4. The feed side is identical to the passive array and the transmit side is shown in Fig. 4.12. A single active unitcell was first built and measured to test stability. No oscillations occurred in the unitcell. The active array, however, had oscillations in the 1-2 GHz range. A stability network consisting of a 56 pF capacitor in series with a 24 Ω resistor from the gate to source of each MESFET eliminated this problem at the expense of gain and efficiency. The feedback was believed to be occurring through the bias lines.

The normailized measured EIRP is shown in Fig. 4.13 versus feed distance for both the active and passive array. For the active array, the focal point shifted

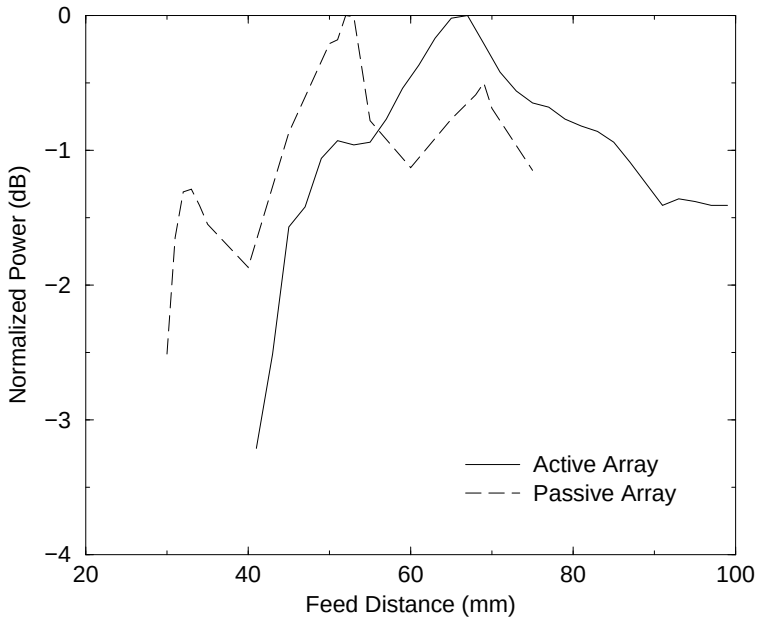


Figure 4.13. Normalized EIRP versus feed distance for the 9-element active (solid line) and passive (dashed line) arrays. The feed is a E-plane horn antenna.

further away from the array. This difference seems to indicate that the phase of the amplifiers is not uniform across the array and is changing the designed focal distance. However, as shown in Fig. 4.14, the radiation patterns are no worse for the active then for the passive array, indicating no loss in directivity. The measured active cross-polarized pattern is also shown here.

Fig. 4.15 compares the E- and H-plane radiation patterns for both a small-signal feed and when the array is heavily saturated. Also shown are the calculated patterns assuming both a uniform amplitude distribution and the amplitude distribution from Fig. 4.5(a). It is expected that when the array saturates, the gain of the center elements compresses more than the outer elements resulting in a more uniform amplitude distribution. This is especially evident in the H-plane by the similarity of the measured saturated pattern to the calculated pattern assuming unifrom amplitude distribution.

The measured maximum EIRP is 53.6 dBm (230 W) at 8.33 GHz. Using the

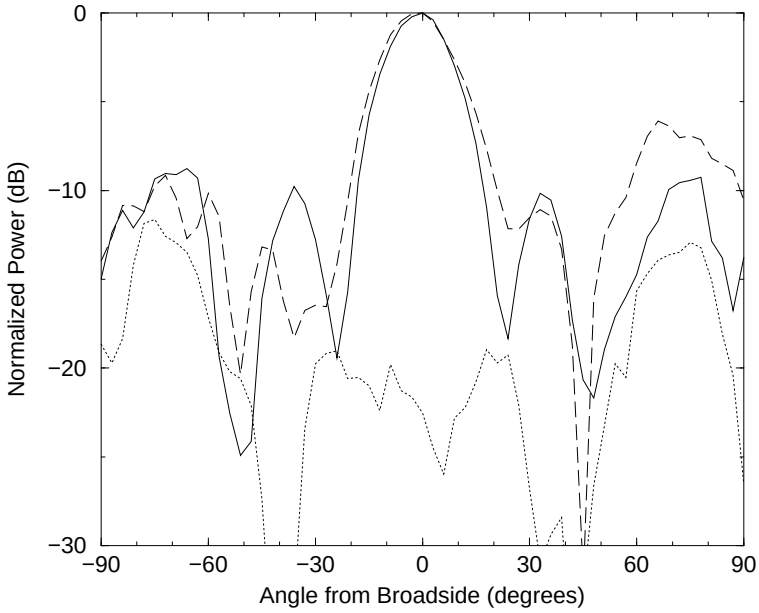


(a)

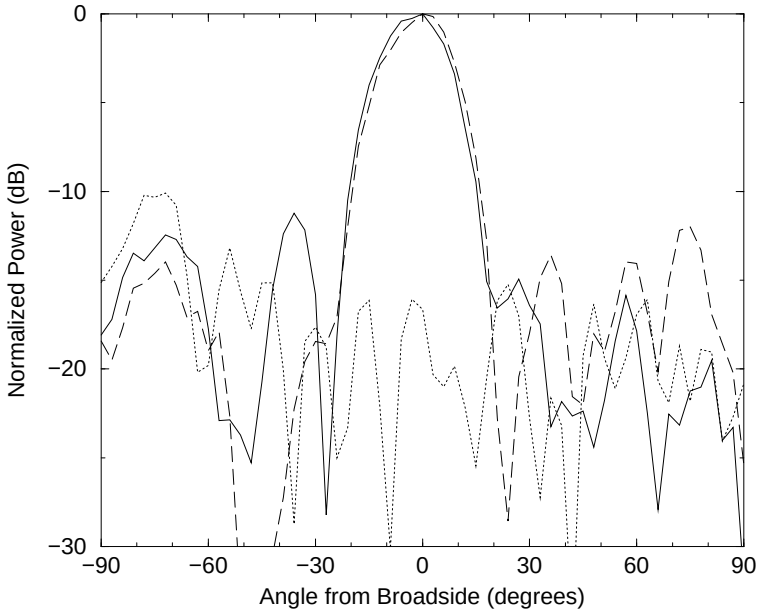


(b)

Figure 4.14. Measured active copolarized (solid line), passive copolarized (dashed line), and active cross-polarized (dotted line) for the E-plane (a) and H-plane (b) radiation patterns of the 9-element active array.

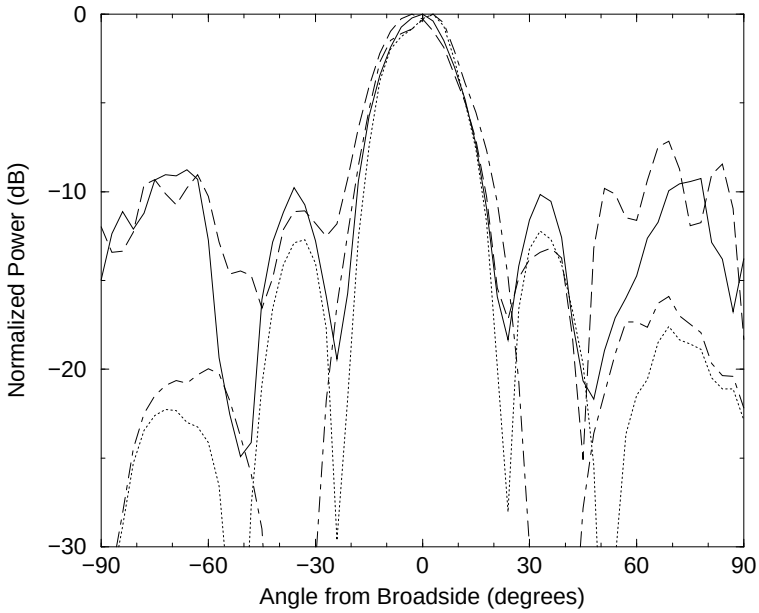


(a)

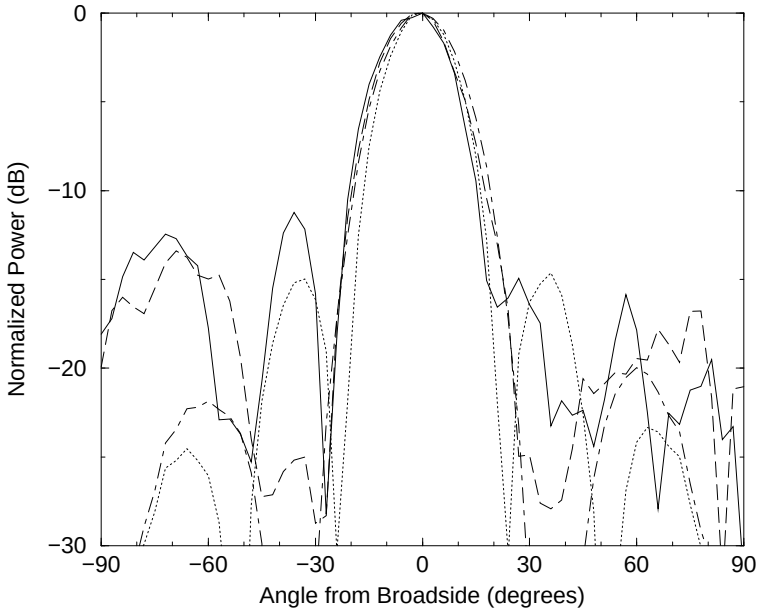


(b)

Figure 4.15. Copolarized E-plane (a) and H-plane (b) radiation patterns of the 9-element active array for the measured saturated (solid line) and small-signal (dashed line) array. Also shown are the calculated patterns assuming uniform amplitude distribution (dotted line) and amplitude distribution from Fig. 4.5(a) (dot-dashed line).

lossless directivity of 19.12 dB, the effective transmitter power is 34.5 dBm (2.8 W). The overall efficiency, based on the effective transmitter power and the predicted input power for each element is 29%. To use Gouker's definition of power combining efficiency, Eq. 4.6, the maximum avaliable power from each element must first be defined. If this is defined as the absolute maximum power that can be obtained when each element is heavily saturated, 710 mW, then the PCE is 41%. However, as indicated in Fig. 4.5, not every device can be optimally saturated. If the maximum available power is defined as the maximum power that each element can produce based on its calculated input power (as determined by individual amplifier measurements in Section 2.4.4), then the PCE is 59%. This figure can be factored further as follows:

- 91% due to stability network
- 83% due to patch radiation efficiency (assuming the efficiency remains the same when the patch is placed in an array)
- 78% due to other effects

However, as mentioned earlier, it is perhaps better to use the definition of PCE based on overall efficiency, Eq. 4.7. As with Gouker's definition, there is still ambiguity as to the value to use for $\eta_{\text{amp}}$. If the maximum measured value of overall efficiency for a single ampifier is used, 58%, then this definition yields a PCE of 51%. If the overall efficiency of each element is based on its predicted input power in the array, then the PCE is 55%. This can also be factored further:

- 86% due to stability network
- 83% due to patch radiation efficeincy
- 78% due to other effects

It is interesting to note that when the loss mechanisms are factored out, both definitions give the same weight, 78%, to other effects. This figure likely consists of losses due to nonuniform phase and amplitude distribution, as well as changes in

antenna impedance due to mutual coupling.

**4.5.7 Active 36-Element array** A 36-element active array was designed using the same unitcell spacing as the 9-element arrays and the same F/D ratio, giving a focal distance of 187 mm. The feed side is shown in Fig. 4.16(a) and the transmit side is shown in Fig. 4.16(b). There are three seperate gate bias lines for this array: one for the center four elements, one for the next ring of 12 elements, and one for the outer ring of 20 elements. It was noticed in the 9-element array that when the center element saturates, rectification of the gate-to-source junction effects the biasing of the other elements on that bias line. This array also required the same stability networks as the 9-element active array.

The normalized measured EIRP is plotted versus feed distance in Fig. 4.17. The feed is a E-plane horn antenna. Maximum EIRP occurs at a feed distance of 176 mm from the horn aperture to the array surface.

Fig. 4.18 compares the measured copolarized and cross-polarized radiation patterns. Cross-polarized radiation is 15 dB below copolarized in both planes.

Fig. 4.19 shows the measured E- and H-plane radiation patterns for the small-signal and saturated cases versus the patterns calculated assuming both a uniform amplitude distribution and the amplitude distribution from Fig. 4.5(b). Because the sidelobes are higher for a uniform amplitude distribution, it would be expected that the saturated pattern would have higher sidelobes than the small-signal pattern. There is no evidence of this, as the saturated and small-signal patterns are virtually identical.

The measured maximum EIRP is 64.2 dBm (2.63 kW) at 8.38 GHz. Using the lossless directivity value of 25.12 dB, the effective transmitter power is 39.1 dBm (8.13 W). The overall efficiency, based on the predicted input power for each element, is 28%. If the maximum saturated power from each device, 710 mW, is used as the maximum avaliable power from each element, then Gouker's definition of power

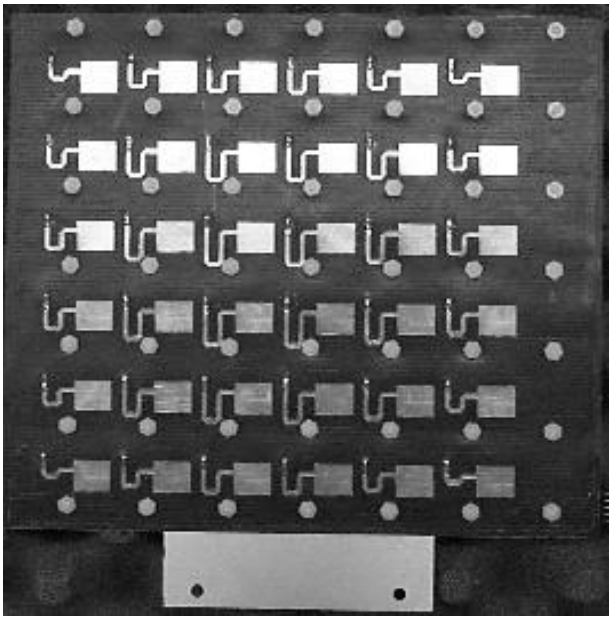

(a)

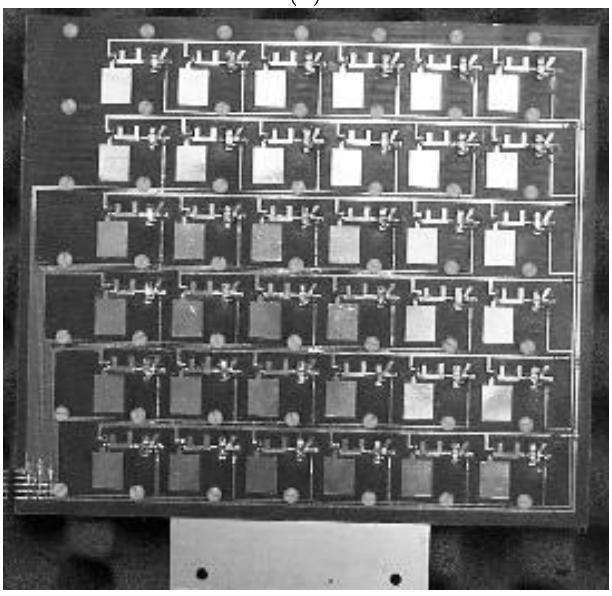

(b)

Figure 4.16. Picture of the feed side (a) and transmit side (b) of the 36-element active array.

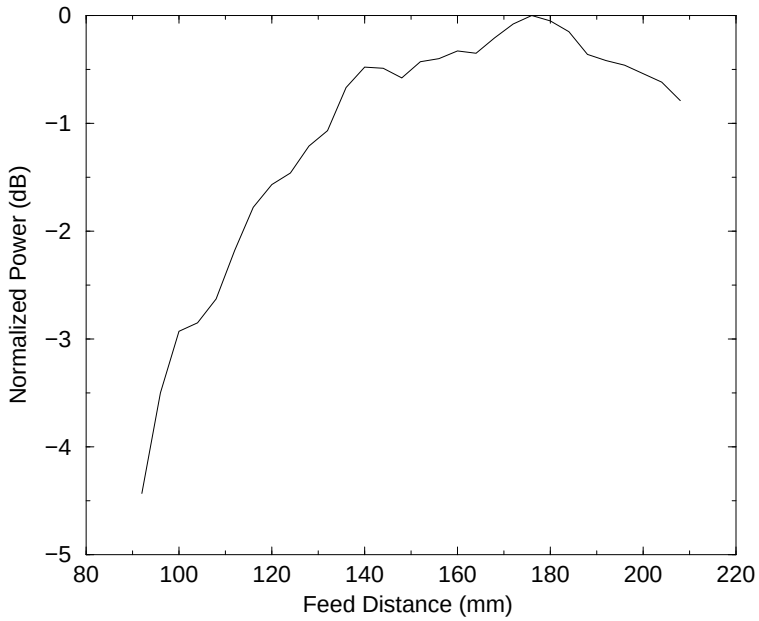


Figure 4.17. Normalized received power versus feed distance for the 36-element active array. The feed is a E-plane horn antenna.

combining efficiency, Eq. 4.6, gives a PCE of 32%. If the maximum available power is defined as the maximum power that each element can produce based on its calculated input power (as determined by individual amplifier measurements in Section 2.4.4), then the PCE is 47%.

The drain current, however, was considerably less than expected based on the expected saturation level of the elements (4.0 A versus 4.7 A). The reason for this is uncertain. But because of this, it is more appropiate to use the definition for PCE based on overall efficiency, Eq. 4.7. This gives a PCE of 49% if $\eta_{\text{amp}}$ is taken to be the maximum overall efficiency in saturation (58%). If the overall efficiency of each element is based on its predicted input power, then the PCE is 52%. This can be factored further as follows:

- 86% due to stability network
- 83% due to patch radiation efficiency
- 73% due to other effects

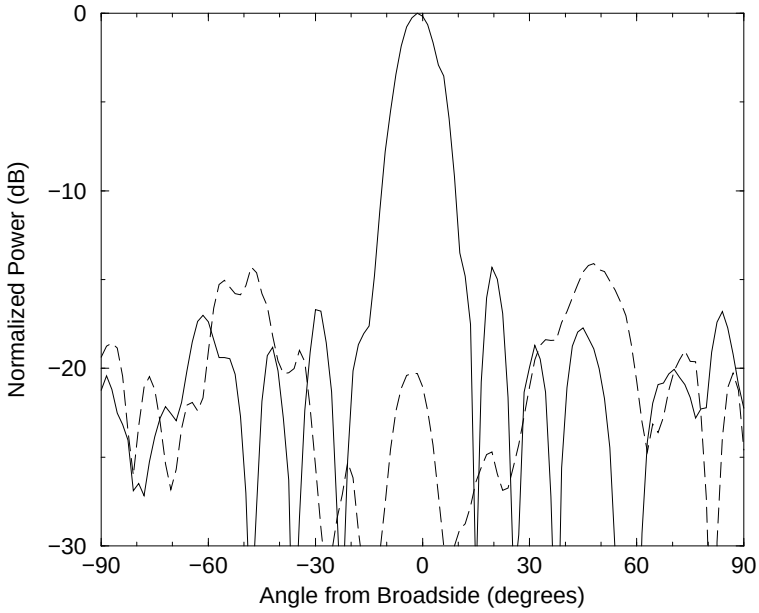


(a)

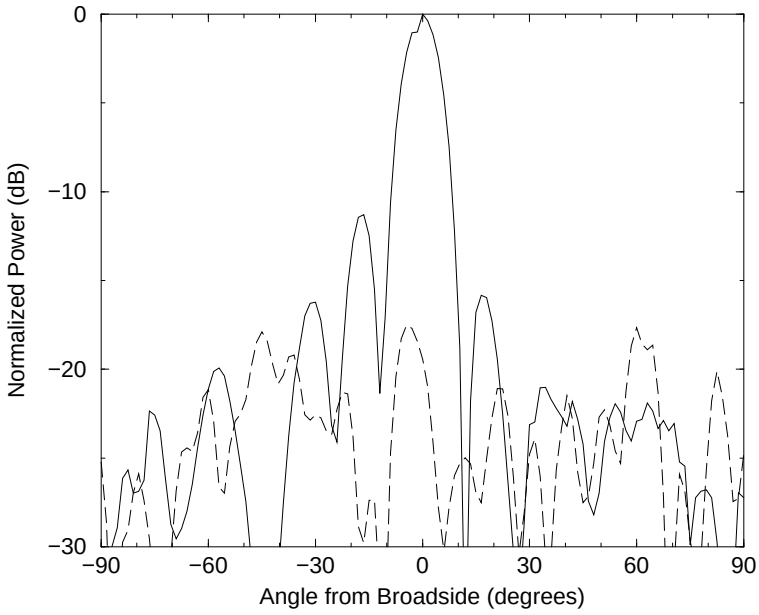


(b)

Figure 4.18. Measured copolarized (solid line) and cross-polarized (dotted line) for the E-plane (a) and H-plane (b) radiation patterns of the 36-element active array.

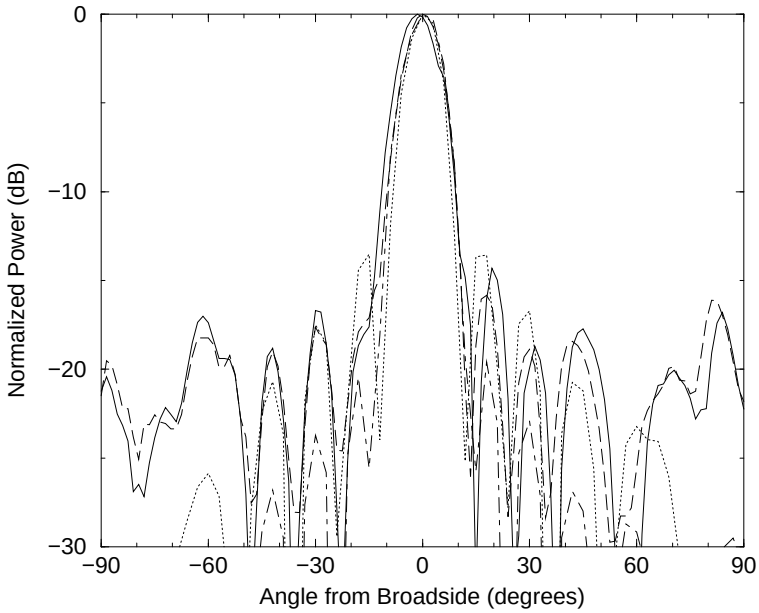


(a)

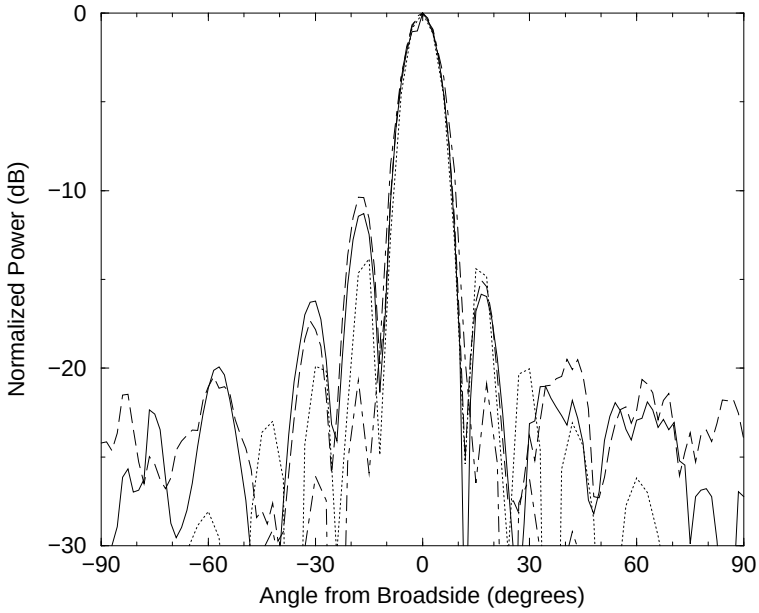


(b)

Figure 4.19. Copolarized E-plane (a) and H-plane (b) radiation patterns of the 36-element active array for the measured saturated (solid line) and small-signal (dashed line) array. Also shown are the calculated patterns assuming uniform amplitude distribution (dotted line) and the amplitude distribution from Fig. 4.5(b) (dot-dashed line).

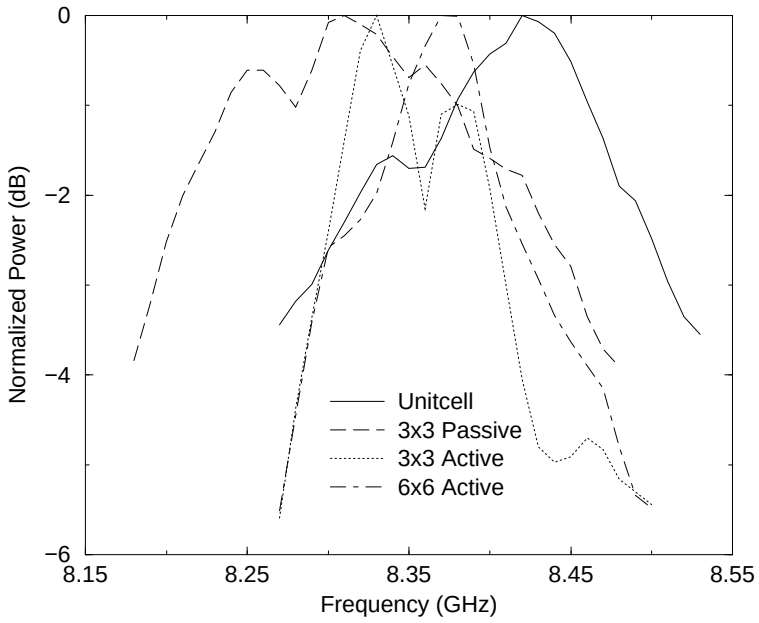


Figure 4.20. Frequency sweep of the active unitcell (solid line), passive 9-element array (dashed line), 9-element active array (dotted line), and 36-element active array (dot-dashed line).

### 4.6 Comparison, Analysis, and Conclusions

It is interesting to compare the response of the arrays as a function of frequency. The normailzed measured EIRP of the active unitcell, passive 9-element array, 9-element active array, and 36-element active array are shown in Fig. 4.20 versus frequency. Recall that the single patch antenna had lowest return loss at 8.42 GHz. This is also where the active unitcell works best. The passive 9-element array, however, has shifted down to 8.31 GHz. The two active arrays do not shift quite as far. This could be due to mutual coupling effects. Since the amplifier works reasonably well over this entire range, this is not a problem unless some patches operate at a different frequency than others.

In Section 4.5.2, it was mentioned that the calculated feed loss of the 9-element and 36-element arrays was 6.6 dB and 7.6 dB respectively. This is contrary to the assertion that for a spatial feed, the feed loss is independent of the number

| Array Size | Calculated Feed Loss |
|---|---|
| 3 x 3 | 6.6 dB |
| 4 x 4 | 6.9 dB |
| 5 x 5 | 7.3 dB |
| 6 x 6 | 7.6 dB |

Table 4.4. Calculated feed loss of patch antenna constrained lens arrays with a F/D of 0.87 and a unitcell spacing of 0.85 $\lambda$ x 0.85 $\lambda$.

of elements. To further investigate this, the feed loss was calculated for 4x4 and 5x5 arrays with the same F/D ratio and unitcell spacing as the arrays in this chapter. Table 4.4 shows the calculated feed loss for all these arrays. The loss clearly increases with number of elements, at the approximate rate of 0.5 dB for each doubling of the number of elements. This indicates that in terms of feed loss, circuit feeding is superior to a constrained lens. However, a constrained lens has certain advantages in terms of functionality, e.g. beamsteering [51] and diversity reception [52], [53]. For a power amplifier transmitting array, however, the hard-horn feed appears to be a more reasonable choice for a spatial feed.

As mentioned earlier, bias lines contribute significantly to feedback and instability. They also complicate array design and decrease power density since more space needs to be allotted for them. An attractive alternative is to move all the bias circuitry to a seperate layer. Vias can then be used to bring the bias up to the rf layer. This would also allow for greater seperation between gate and drain bias lines to decrease coupling leading to feedback. DC losses in the bias lines could also be eliminated, since there would be no pressure to conserve space by using narrow bias lines.

If these steps are taken to ensure greater stability, then the resistive network used in the active arrays would not be necessary. This would result in PCEs of 65% and 61% for the 9-element and 36-element arrays respectively. For the 36-element array, this figure is roughly equivalent to a circuit combiner with 0.4 dB loss per stage. Although two data points are not sufficient for a valid conclusion, the

combining efficiency appears to drop at a rate equivalent to a circuit combiner with 0.13 dB loss per stage. Therefore, for a combiner using hundreds of elements where the desired output is a free-space plane wave, spatial power combining appears to be an attractive option.

# CHAPTER 5

# CLASS-E OSCILLATORS

## 5.1 Introduction

While a great amount of work has been done to improve the efficiency of microwave amplifiers, little has been done to address the same problem in oscillators. Achieving high efficiency in microwave oscillators is important for the same reasons as in amplifiers—increasing the output power, battery lifetime, and reliability of transmitters. Microwave oscillators have demonstrated 67% conversion efficiency with 250 mW of output power at 1.6 GHz using a class-F amplifier in a feedback oscillator [54]. In [55], a 3-port MESFET oscillator operating in class-AB mode was demonstrated with 60% efficiency and 16 mW output power at 14.5 GHz.

In this chapter, feedback is added to a class-E amplifier similar to the one presented in [2]. The oscillator is designed using a quasi-linear approximation of large-signal operation. A hybrid oscillator indicating class-E operation was fabricated and characterized [56],[57]. Also, a 4-element class-E 5-GHz amplifier array was converted into an oscillator by introducing free-space global feedback. To calculate the efficiency of this oscillator array, without depending on accurate 3-D pattern measurements, an equation was derived for efficiency in terms of measured temperature change. The goal of this work is to show that the functions of oscillator and power amplifier can be combined efficiently into a single circuit.

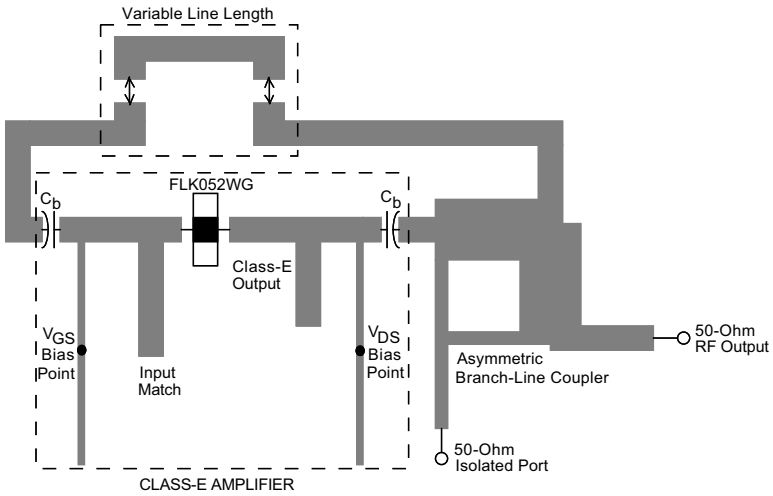


Figure 5.1: Layout of 5-GHz microstrip class-E oscillator.

## 5.2 5-GHz Microstrip Class-E Oscillator

A feedback oscillator configuration with a high-efficiency class-E amplifier is used in the design. The oscillator design approach described in [58] is performed with a linear circuit simulator. The feedback length is adjusted for an oscillation frequency of 5.0 GHz and the amount of coupling is optimized for the correct compression point. An asymmetric microstrip branch-line coupler is used to provide the feedback through a length of microstrip transmission line. The circuit layout is shown in Fig. 5.1.

The circular function [58], $C$, which is similar to the closed-loop gain, is used in the simulations and is given by:

$$C = \frac{s_{11}s'_{11} + s_{21}s'_{12} - (s_{11}s_{22} - s_{12}s_{21})(s'_{11}s'_{22} - s'_{12}s'_{21})}{1 - s_{22}s'_{22} - s_{12}s'_{21}},$$

where $s_{ij}$ are the small-signal $s$-parameters of the class-E amplifier and $s'_{ij}$ are the $s$-parameters of the feedback network. Oscillations occur where the phase of the circular function crosses zero degrees with a magnitude greater than one. The MESFET saturates to the point where $|C|$ is exactly one. Device saturation is simulated by reducing the magnitude of $s_{21}$. This is shown in [59] to be a reasonable approximation

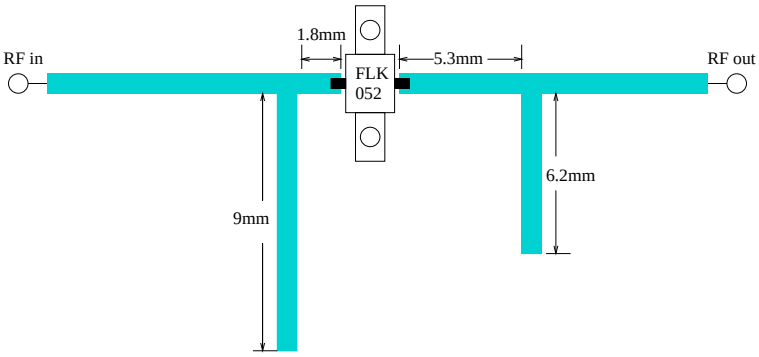


Figure 5.2: 5-GHz class-E amplifier in microstrip.

of the large-signal operation of a FET for small levels of saturation.

**5.2.1 Amplifier Design** The 5-GHz class-E amplifier uses a Fujitsu FLK052 MESFET and is fully characterized in [3] and [4]. The input match is designed for gain by measuring $s_{11}$ in saturation. The output circuit has a fundamental impedance for class-E operation given by Eq. 2.6. The layout of the microstrip amplifier is shown in Fig. 5.2.

Measurements of the saturated output power and efficiency are shown in Fig. 5.3. The feedback should be designed so that the amplifier is operating at the amount of saturation that has the maximum power-added efficiency, since this is equivalent to maximum conversion efficiency for an oscillator.

**5.2.2 Coupler Design** An asymmetric branch-line coupler was designed to couple power back to the amplifier to satisfy the oscillation condition. The coupler was designed using MDS by setting the electrical length of all the lines equal to 90° and optimizing the characteristic impedance of each line to get the correct amount of feedback.

Two couplers were designed and built. The first one did not couple enough power to the feedback loop, resulting in a relatively low-power oscillator. A second coupler was designed to couple -6.5 dB back to the amplifier and -1.1 dB to the load. This is the coupler shown in Fig. 5.4 and which was used in the final oscillator

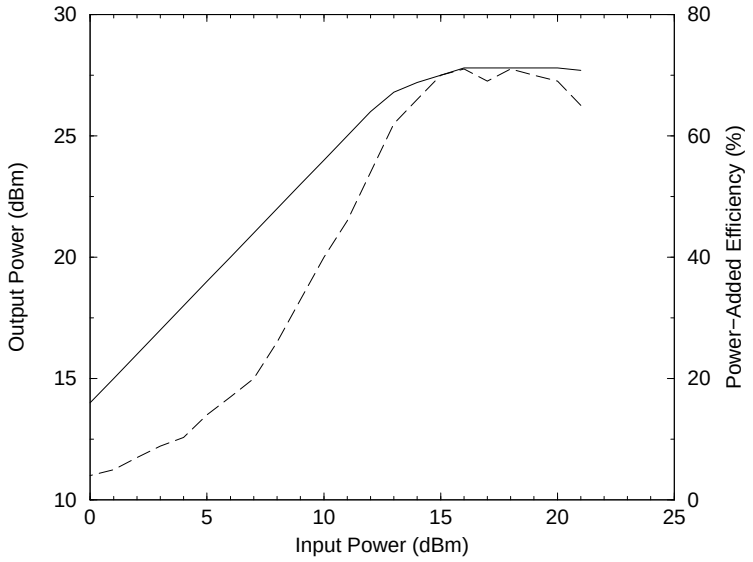


Figure 5.3. Measured output power (solid line) and power-added efficiency (dashed line) of the 5-GHz class-E amplifier.

design. A 50-Ω load was placed at the isolated port. Simulated S11-S41 are shown in Fig. 5.5.

**5.2.3 Oscillator Design** The class-E amplifier achieves maximum power-added efficiency when it is operating approximately 4 dB into compression (Fig. 5.3). The amount of coupling is adjusted in the simulations so that 4 dB of compression reduces $|C|$ to unity at 5.0 GHz. The feedback length is then adjusted

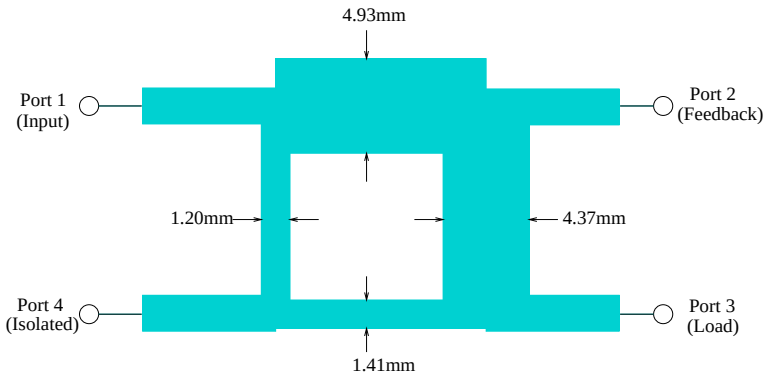


Figure 5.4. Microstrip layout of the branch-line coupler used in the 5-GHz class-E oscillator.

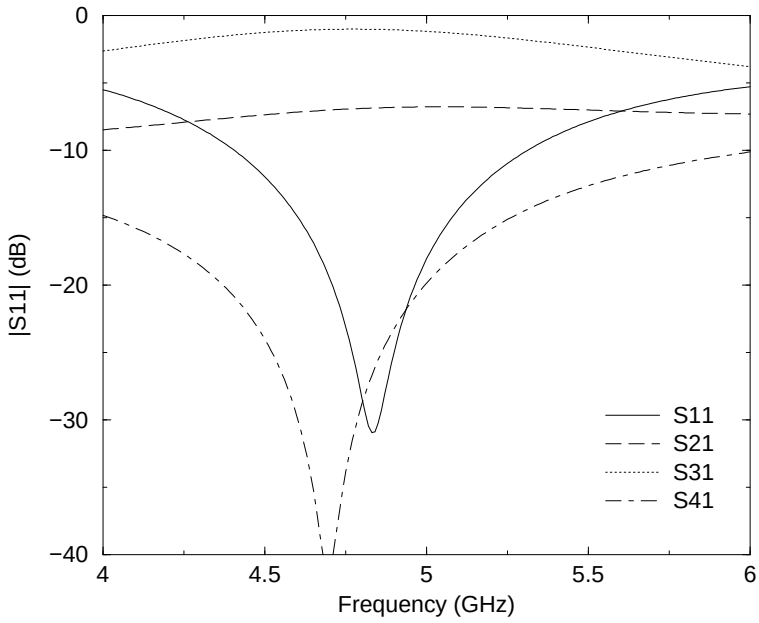


Figure 5.5: Simulated response of asymmetric branch-line coupler.

to make $\angle C$ equal to zero degrees at 5.0 GHz. Since these simulations are based on small-signal $s$-parameters, the feedback line length is made to be tunable.

After fabrication, the feedback length is experimentally tuned to produce an oscillation at exactly 5.0 GHz. The first design was intended to couple -5.7 dB of the amplifier output power to the feedback loop and -1.4 dB to the load. This oscillator achieved an output power of 210 mW with 43% conversion efficiency and was operating too far into compression. It is likely that too much coupling was predicted in the simulation because the effects of large-signal operation on the input and output match are ignored. Nonlinear simulations show that in some cases when $|s_{21}|$ compresses by 25%, $|s_{11}|$ decreases by 33%. A second oscillator was designed and fabricated with reduced coupling in order to increase the power and efficiency. The second design couples -6.5 dB of the output power to the feedback loop and -1.1 dB to the load. Experimental results for this design are presented in the following section.

Fig. 5.6 shows the simulated circular function for this oscillator with no

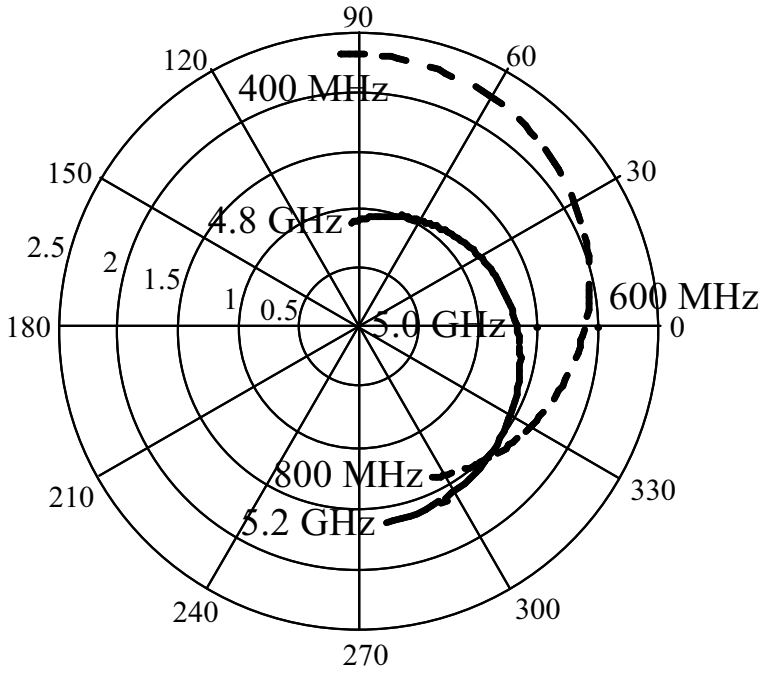


Figure 5.6. Simulated circular function for the unsaturated class-E oscillator. The dashed line shows an oscillation near 600 MHz and solid line shows an oscillation near 5 GHz.

saturation taken into account. Only the frequency ranges where the oscillation conditions are met are shown here. This simulation shows a low-frequency oscillation near 600 MHz which appears to be more compressed than the desired 5-GHz oscillation. The high level of saturation for the 600-MHz mode is verified experimentally by the large number of harmonics produced by this mode, as shown in Fig. 5.7. This low-frequency oscillation is supressed in the circuit by lowering the value of $C_b$ in Fig. 5.1. The measured oscillation frequency of the 5-GHz mode differs less than 3% from simulation.

**5.2.4 Measurements** Fig. 5.8 shows the measured output power and conversion efficiency of the oscillator versus drain current for three different values of $V_{DS}$. The lines on the plot represent the range over which the oscillation remains stable. The plot shows that as the drain current increases, the efficiency decreases while the output power remains the same. There is no advantage, therefore, in

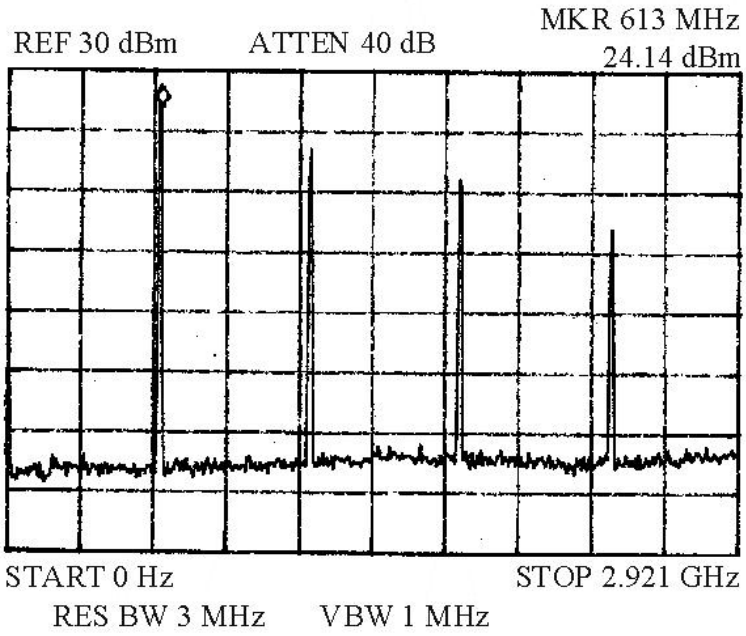


(a)

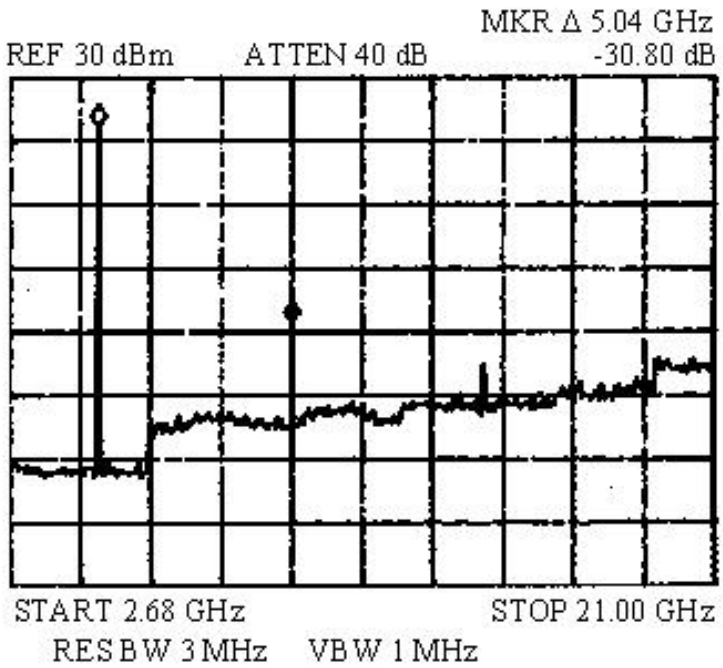


(b)

Figure 5.7. Measured spectrum of the 600-MHz (a) and 5-GHz (b) modes of the class-E oscillator.

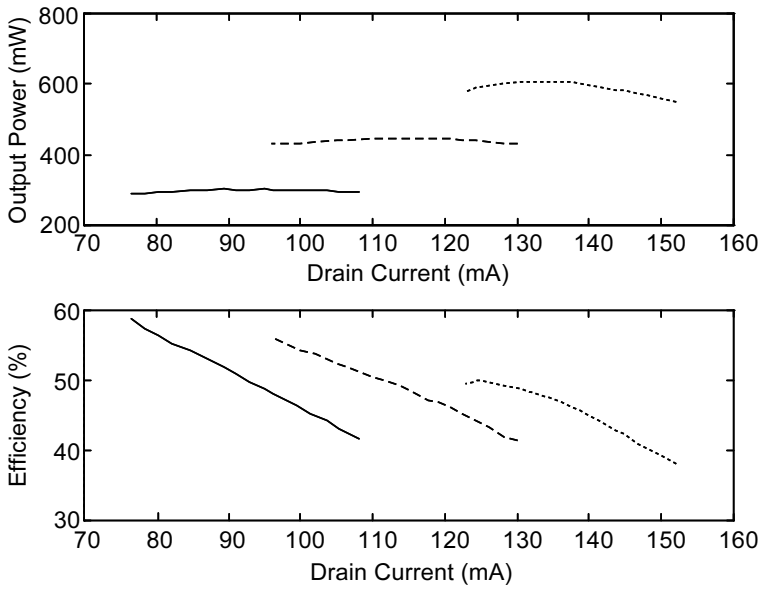


Figure 5.8. Output power and conversion efficiency versus drain current, $I_{DS}$, with $V_{DS} = 6.5\,V$ (solid line), $V_{DS} = 8\,V$ (dashed line) and $V_{DS} = 9.5\,V$ (dotted line) for the 5-GHz class-E oscillator.

raising the drain current above the minimum level. The maximum efficiency is 59% for $V_{DS} = 6.5\,V$ and 300 mW of output power. The maximum output power is 600 mW for $V_{DS} = 9.5\,V$ and 48% conversion efficiency. The oscillation frequency varies less than 1% over the entire biasing range shown here.

Table I compares the class-E amplifier and the oscillator presented here for the same bias point. Neglecting losses, the expected output power of the oscillator is the power added by the amplifier. The expected efficiency is equal to the power-added efficiency of the amplifier at this bias point. As the table shows, the efficiency is lower than the ideal level. Some of the difference is due to losses in the circuit, but most is believed to be caused by the oscillator still operating too far into compression. This can be corrected in the design if the large-signal characteristics of the MESFET are known accurately. These results show the need for good nonlinear models when designing oscillators for high efficiency.

The phase noise was measured to be -70 $\frac{\text{dBc}}{\text{Hz}}$ at a 100 kHz offset. This is too

| | $V_{DS}$ | $I_{DS}$ | Power | Eff |
|---|---|---|---|---|
| Amplifier | 8 V | 93 mA | 27.8 dBm | 72% |
| Ideal Oscillator | 8 V | 93 mA | 27.3 dBm | 72% |
| Measured Oscillator | 8 V | 96 mA | 26.7 dBm | 56% |

Table 5.1. Comparison between class-E amplifier and class-E oscillator. Second row shows ideal oscillator performance based on amplfier measurements. Third row shows measured oscillator data.

high for many communication applications. This figure may be improved by adding a high-Q resonator to the feedback loop.

## 5.3 A Class-E Oscillator Array

The 5-GHz class-E amplifier used above was also successfully integrated into an active antenna array, shown in Fig. 5.9, demonstrating power combining of four elements with an estimated 85% power-combining efficiency [4]. At 5.05 GHz, the class-E power amplifier antenna array delivers a total of 2.4 W of output power with a drain efficiency of 74% and a power-added efficiency of 64%. In this active array, a plane wave is incident on an array of antennas, each one connected to an amplifier input. The outputs of the amplifiers are each connected to an output antenna. The array of output antennas radiates an amplified plane wave [51]. The antennas are second-resonant slot antennas in the microstrip ground plane coupled to the microstrip feed lines. The input and output antennas are orthogonally polarized to provide isolation. In this section, global free-space feedback is used to convert this amplifier array into an oscillator array.

**5.3.1 Feedback Design** To convert this array into an oscillator, it is necessary to introduce positive feedback between the input and output antennas. The signal radiated by the output slot must be reflected and shifted in polarization by 90°. This is accomplished by placing a polarizer a quarter wavelength in front of a mirror. When the polarizer is oriented 45° with respect to the polarization of the

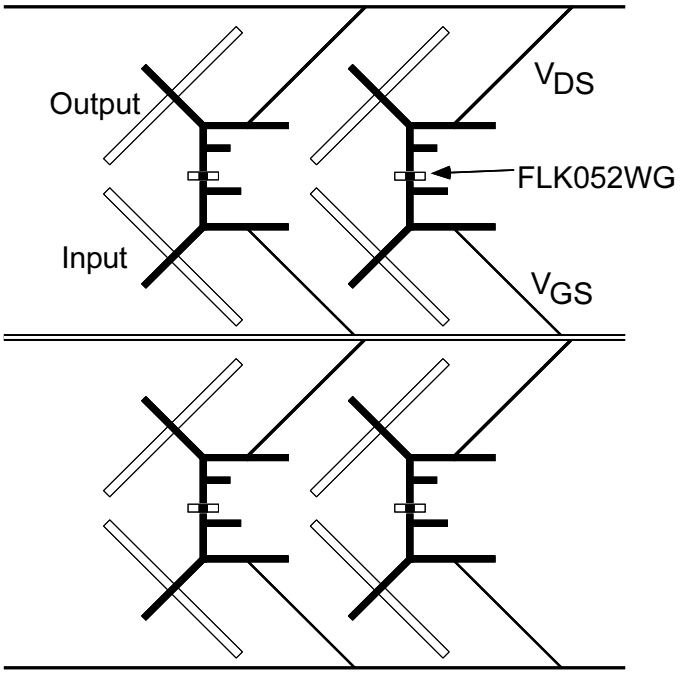


Figure 5.9. The class-E power amplifier antenna array. This 4-element power-combiner demonstrates 2.4 W of output power at 5.05 GHz with 8.8 dB compressed gain, 74% drain efficiency, and 64% power-added efficiency.

output wave, maximum feedback occurs. The polarizer splits the output wave into two orthogonal components. One component is reflected by the polarizer; the second component passes through the polarizer and is reflected by the mirror, but with an additional 180° phase shift. The net result is a reflected wave with polarization normal to the incident wave. By rotating the polarizer away from 45°, the amount of feedback can be reduced if needed. The same approach was used to convert a grid amplifier into a tunable oscillator in [60]. The array with external feedback is shown in Fig. 5.10.

**5.3.2 Measurements** By varying the distance from the array to the "twist reflector", about 3% frequency tunability can be obtained. This is shown in Fig. 5.11 for two configurations: the back side of the array facing the reflector and the front side facing the relector. The slots should radiate slightly more into the dielectric substrate (out the front side), so this configuration should provide more

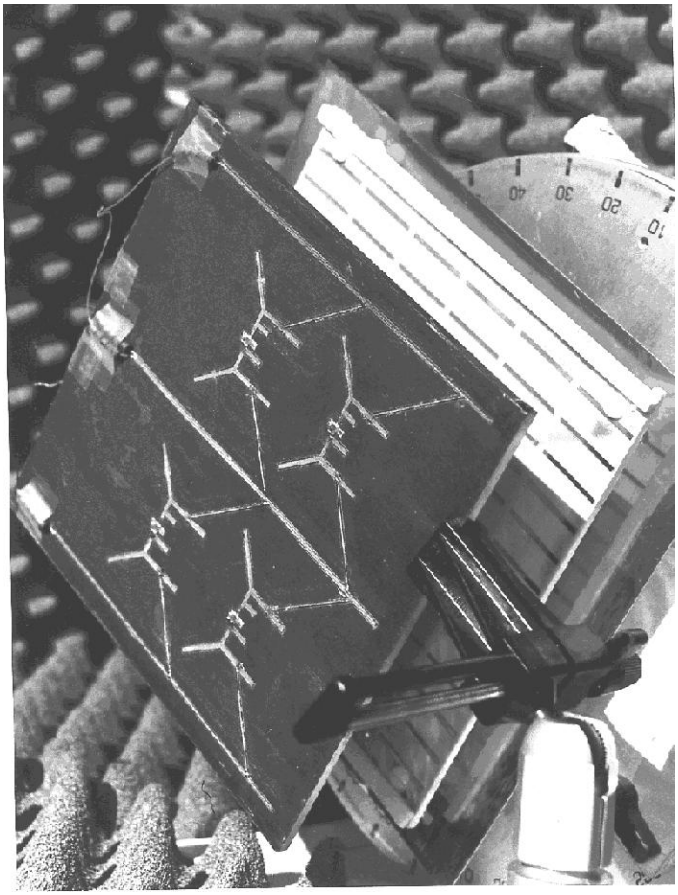

Figure 5.10: The class-E external feedback oscillator array.

feedback. However, this exposes all the amplifier circuitry on the front side to the reflected radiation. More tunability in frequency could be obtained if the distance from the polarizer to the mirror was also varied.

The received power was also measured as a function of the angle between the polarizer and output field. As stated earlier, maximum feedback occurs when this angle is 45°. This is shown in Fig. 5.12 for both configurations. This suggests that radiated power could be further increased if more feedback were added.

At the distance where each configuration radiated maximum power, the power was measured as a function of drain current. This is shown in Fig. 5.13. The drain current was changed by varying the gate voltage. For the backside facing the

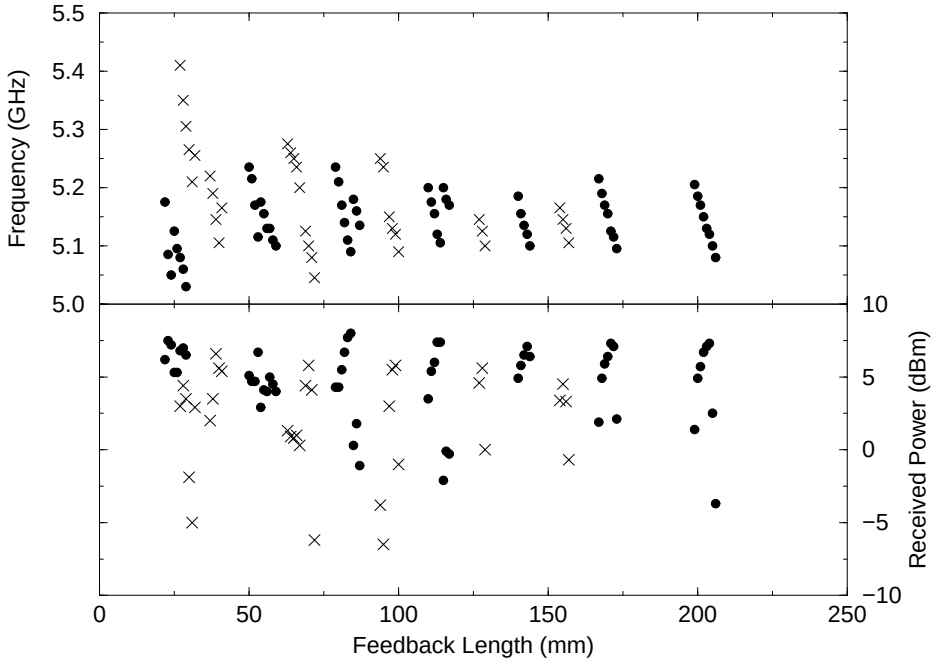


Figure 5.11. Measured oscillation frequency and recived radiated power as a function of the distance from amplifier array to twist reflector for the array back side (circles) and front side (crosses) facing reflector.

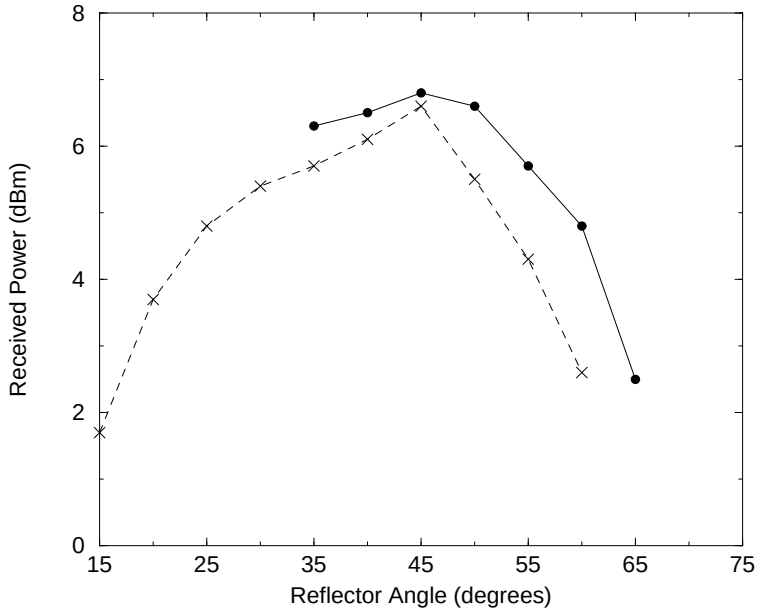


Figure 5.12. Measured recived radiated power as a function of angle of twist reflector with respect to output antennas for the array back side (circles) and front side (crosses) facing reflector.

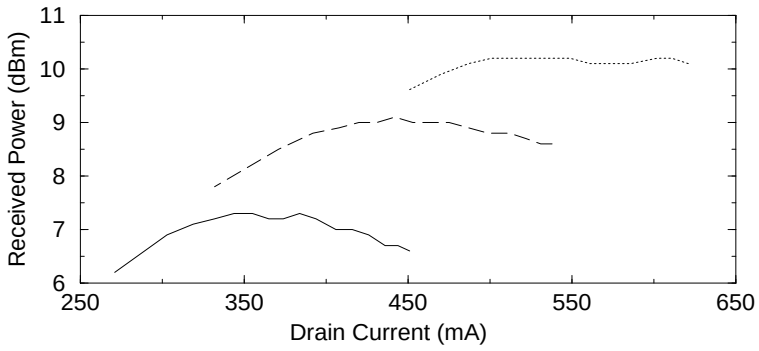


(a)

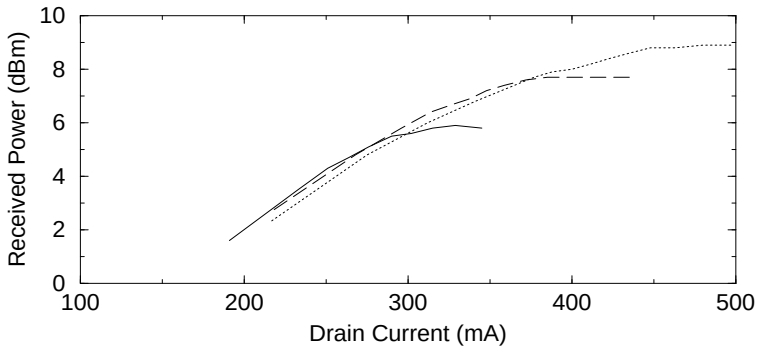


(b)

Figure 5.13. Measured recived radiated power of the free-space oscillator array as a function of drain current for array back side (a) and front side (b) facing reflector. (a) is measured at an array-reflector distance of 87 mm. (b) is measured at an array-reflector distance of 42 mm. $V_{DS}$ is 6.5 V (solid line), 8.0 V (dashed line), and 9.5 V (dotted line).

reflector, the array draws more current than the other configuration and the radiated power reaches a maximum at less than maximum current. This would suggest that this configuration provides more feedback, since the amplifiers draw more current when they are saturated.

The phase noise was measured to be -85 $\frac{\text{dBc}}{\text{Hz}}$ at an offset of 100 kHz. This is lower than the single microstrip oscillator using the same device, because the phase noise components do not add coherently, but the desired mode does.

**5.3.3 Determining Efficiency Through Heat Measurements** Calculating actual radiated power, and therefore efficiency, requires knowledge of the

directive gain of the array. For larger arrays, a typical approximation is to assume that the effective area is equal to the physical area [40]. However, here we have only a 4-element array. Also, as Fig. 5.14 shows, the cross-polarized radiation is quite high. This is due to the reflected feedback power diffracting to the transmit side of the array. And in Fig. 5.15 which shows the calculated array factor, the radiation in the planes 45° to the E- and H-planes there are significant grating lobes. This is because the unitcell spacing in this array is greater than a wavelength in these directions. Therefore, another way is needed to estimate the output power and efficiency of this oscillator array.

The dissipated power in either an amplifier or an oscillator can be expressed as

$$P_{\mathrm{diss}} = (1-\eta)P_{\mathrm{dc}},$$

where $\eta$ is the conversion efficiency for an oscillator or the power-added efficiency for an amplifier.

Therefore, the ratio of the disspated power of one amplifier or oscillator, $P_{\mathrm{diss}_1}$, to another, $P_{\mathrm{diss}_2}$ can be expressed as

$$\frac{P_{\mathrm{diss}_1}}{P_{\mathrm{diss}_2}} = \frac{(1-\eta_1)P_{\mathrm{dc}_1}}{(1-\eta_2)P_{\mathrm{dc}_2}}.$$

From thermodynamic considerations, the dissipated power can also be expressed as the change in heat per unit time, where the change in heat is the change in temperature times the volume and specific heat of the material,

$$P_{\mathrm{diss}} = \frac{\Delta \mathrm{H}}{\Delta \mathrm{t}} = \frac{\mathrm{C_s V \Delta T}}{\Delta \mathrm{t}}.$$

So the ratio of the dissipated power of one amplifier or oscillator to another can be rewritten as

$$\frac{P_{\mathrm{diss}_1}}{P_{\mathrm{diss}_2}} = \frac{C_{\mathrm{s}_1} V_1 \Delta T_1 \Delta \mathrm{t}_2}{C_{\mathrm{s}_2} V_2 \Delta T_2 \Delta \mathrm{t}_1}.$$

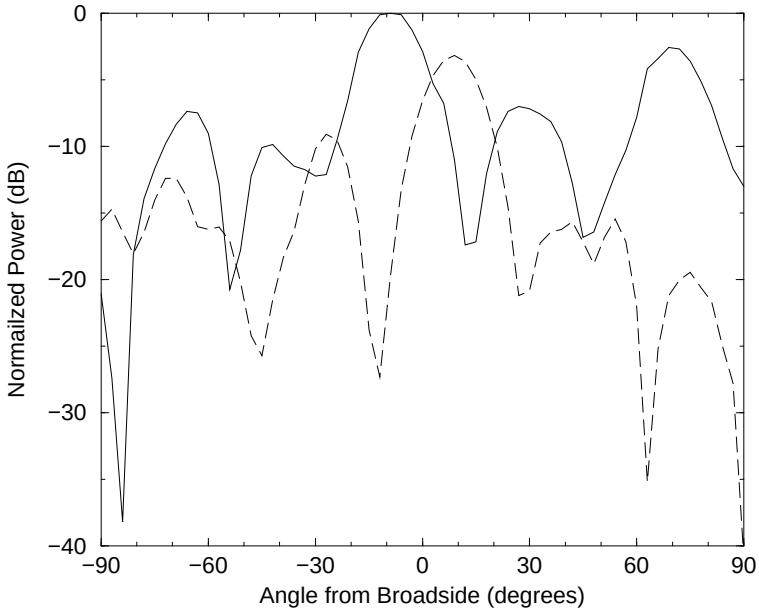


(a)

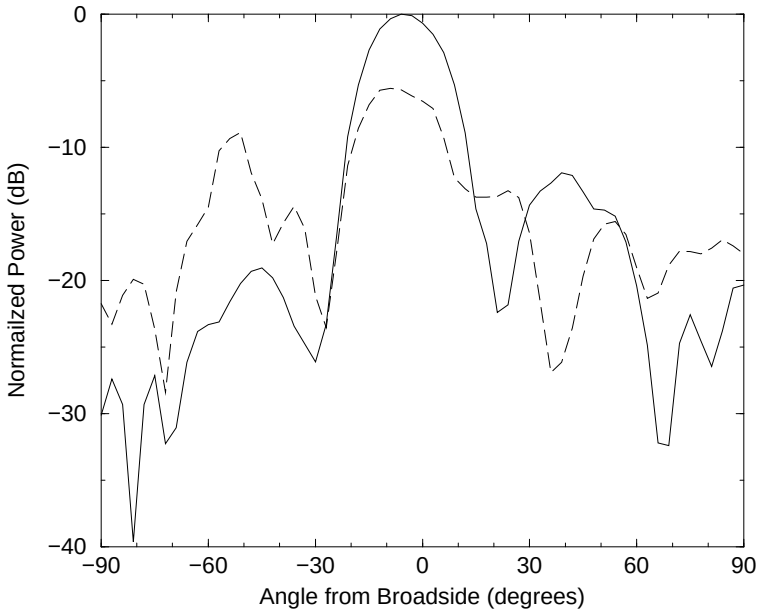


(b)

Figure 5.14. Measured E-plane (a) and H-plane (b) radiation patterns for co-polarized (solid line) and cross-polarized (dashed line) radiation.

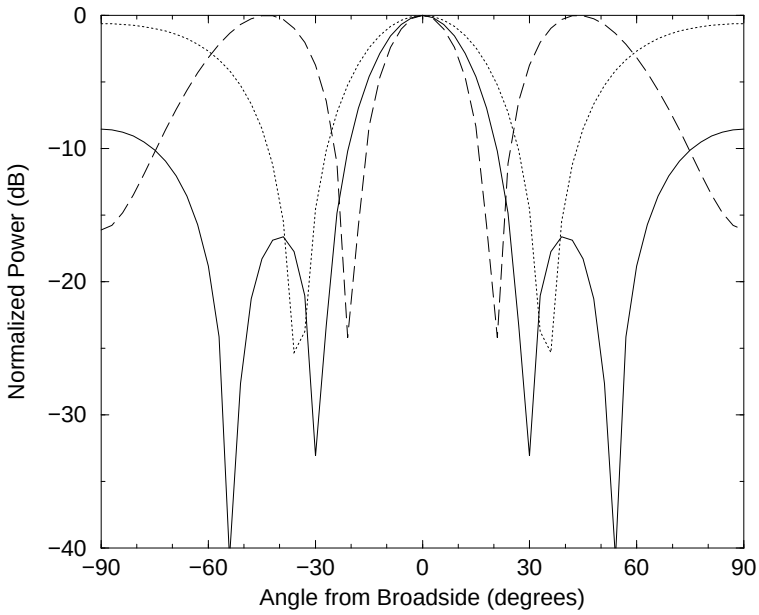


Figure 5.15. Calculated array factor for E- and H-planes (solid line), and the two 45° planes (dashed and dotted lines).

If the material properties are the same ($C_{s_1} = C_{s_2}$ and $V_1 = V_2$) and the measurements are taken over the same time span ($\Delta t_1 = \Delta t_2$), then the ratio of dissipated powers is simply the ratio of the change in temperature,

$$\frac{P_{\mathrm{diss}_1}}{P_{\mathrm{diss}_2}} = \frac{\Delta T_1}{\Delta T_2} = \frac{(1-\eta_1)P_{\mathrm{dc}_1}}{(1-\eta_2)P_{\mathrm{dc}_2}}.$$

Now the efficiency of the first amplifier or oscillator can be expressed as a function of the measured temperature change, the dc power supplied to each, and the efficiency of the second amplifier or oscillator:

$$\eta_1 = 1 - \frac{\Delta T_1 P_{\mathrm{dc}_2}}{\Delta T_2 P_{\mathrm{dc}_1}}(1-\eta_2).$$

This equation was used to calculate efficiency of some of the amplifiers described in chapter 2 by measuring them at input power levels with vastly different power-added efficiencies. This calculation agreed with electrical measurements within 5%.

Applying this technique to the oscillator array described in this chapter gives a maximum output power of 1.25 W (for $V_{DS}$=8.0 V) with a corresponding conversion efficiency of approximately 40% when the reflector is 87 mm behind the amplifier array. The measured EIRP at this point was 34.7 W.

## 5.4 Conclusion

The class-E approach to obtaining high-efficiency is shown to be applicable to oscillators. A maximum conversion efficiency of 59% is measured with an output power of 300 mW. A quasi-linear design approach is shown to be accurate for predicting oscillation frequency, but nonlinear analysis is necessary when designing oscillators for maximum efficiency. Since the feedback network consists only of a microstrip transmission line, this oscillator is fairly noisy—approximately -70 dBc/Hz for a 100-kHz offset. A high-Q resonator may be added in the feedback network to improve this figure.

A 4-element class-E oscillator array utilizing global feedback was also demonstrated. It produced about 1.25 W output power with 40% conversion efficiency. Spectral purity was better than the single microstrip oscillator. However, diffracted cross-polarized radiation in the transmit direction is a problem. An expression for calculating efficiency in terms of measured temperature change was also derived.

# CHAPTER 6

# CLASS-E MULTIPLIERS

## 6.1 Introduction

Frequency multiplication is commonly used in millimeter-wave transmitter systems [61]–[63]. Including a frequency multiplier allows the oscillator to operate at a submultiple of the output frequency resulting in a cheaper, cleaner, and more stable oscillator. Also, operation of the oscillator and high-power stages at different frequencies reduces the effects of feedback. An amplifier chain is typically required in millimeter-wave systems to compensate for the losses in the multipliers and to achieve the necessary output power. Zulinski showed that class-E multipliers can provide high-efficiency multiplication at HF frequencies [64] by demonstrating a 1.685-to-3.370 MHz class-E doubler with 110 mW output power and 94% drain efficiency at the second harmonic. This doubler, however, had zero conversion gain. Recent microwave multiplier results include a 3-to-6 GHz doubler with 7.7 dBm output power and 7.7 dB conversion gain (efficiency was not reported) [65], an InP-based 762.5-to-3050 MHz multipler with 3.74 dBm output power, 2.74 dB conversion gain, and 8% efficiency [66], and an InP-based 127-to-762 MHz multipler with 6 dBm output power, 5 dB conversion gain, and 11% drain efficiency [66]. The intent here is to show that microwave class-E multipliers using non-ideal switches can have conversion gain with reasonably high efficiency, warranting their use at millimeter waves and reducing the amplification requirements.

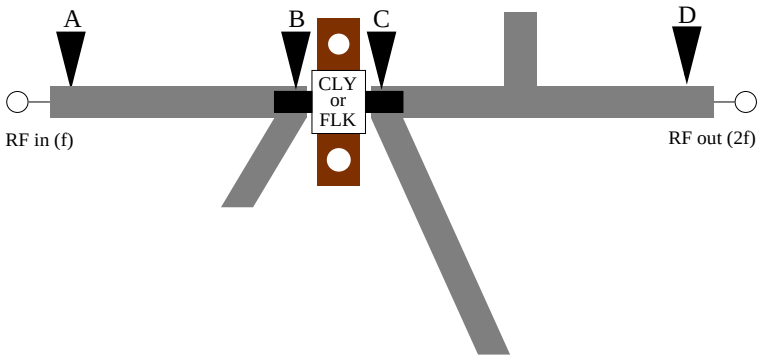


Figure 6.1. General layout of frequency doublers showing locations of photoconductive probing.

In this chapter, a 500 MHz-to-1 GHz frequency doubler and a 2.5 GHz-to-5 GHz frequency doubler are presented. In addition to power and efficiency measurements, time-domain waveforms are measured at various points in the circuit using the photoconductive sampling technique described in Chapter 3.

## 6.2 Class-E Multiplier Design

Fig. 6.1 depicts the general layout of the doubler circuits. The first stub at the output is $\frac{\lambda}{4}$ long at the fundamental frequency, shorting the fundamental and odd harmonics, while passing the second harmonic. The second stub presents the impedance given by Eq. 2.6 to the second harmonic at the drain. Zulinski showed that the load angle for class-E operation is the same at a harmonic as at the fundamental frequency [64]. Ideally, for class-E operation, the rest of the harmonics should be terminated in an open. However, this would require further transmission-line stub matches. The goal here is to see how well these doublers can perform by simply shorting the fundamental and presenting the class-E load impedance to the second harmonic.

The MESFET is biased for class-C operation ($V_{GS}$ below pinchoff) to give a

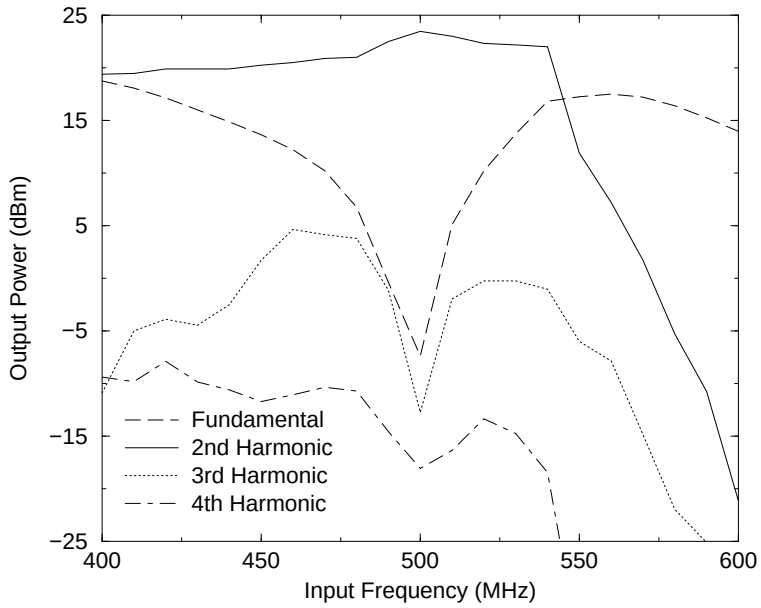


Figure 6.2. Measured output power at the fundamental and first three harmonics versus input frequency for the 1-GHz doubler ($P_{\text{in}}$=15 dBm, $V_{DS}$=5 V, and $I_{DS}$=110 mA).

conduction period below 50%. It can be shown that the conduction period for maximum generation of second harmonic drain current is about 35% [67]. Although it is not done here, it has been shown by Rauscher [68] and Thomas [65] that harmonic tuning at the input can further optimize performance.

### 6.3 1-GHz Doubler

The 1-GHz doubler was fabricated in microstrip using the Siemens CLY5 MESFET. The output powers at the fundamental and first three harmonics were measured as a function of frequency and are shown in Fig. 6.2. Fig. 6.3 shows the measured drain, power-added, and overall efficiencies for the second harmonic as a function of frequency. A 500-MHz, 15-dBm input signal produced 23.5 dBm output power with 35% power-added efficiency at 1 GHz with greater than 30 dB rejection of the unwanted fundamental and harmonic frequencies.

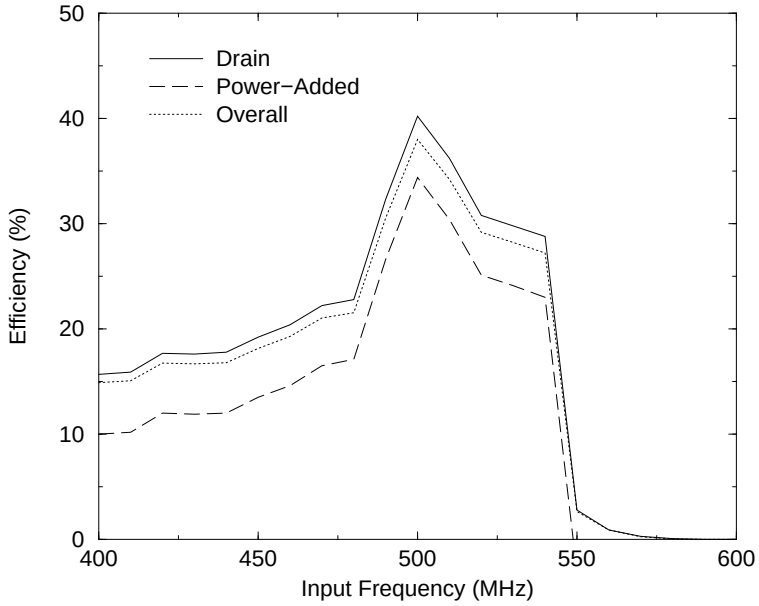


Figure 6.3. Measured second-harmonic drain, power-added, and overall efficiencies versus input frequency for the 1-GHz doubler ($P_{\text{in}}$=15 dBm, $V_{DS}$=5 V, and $I_{DS}$=110 mA). Efficiencies are defined in terms of the output power at the second harmonic.

A five-tone harmonic balance simulation was performed using a Materka nonlinear model for the CLY5 and predicted 24.8 dBm output power, 43% drain efficiency, and 8.8 dB conversion gain. The simulated drain voltage and current waveforms in Fig. 6.4 exhibit characteristics resembling class-E operation; the slope of the current waveform is steeper on the falling edge than on the rising edge.

To perform the photoconductive sampling waveform measurements [32], the doubler was tuned to 480 MHz-960 MHz. Time-domain measurements are shown in Fig. 6.5. As shown, at both points **A** and **B**, there is significant harmonic content, especially third harmonic. This indicates that third harmonic power is being reflected back to the input. Based on these measurements, an improved design should include third harmonic tuning at the input. At point **D**, a fairly pure sine wave at the second harmonic is seen. At the drain, point **C**, some wave-shaping is seen, but not enough to consider this class-E operation. More harmonic tuning is required at the output.

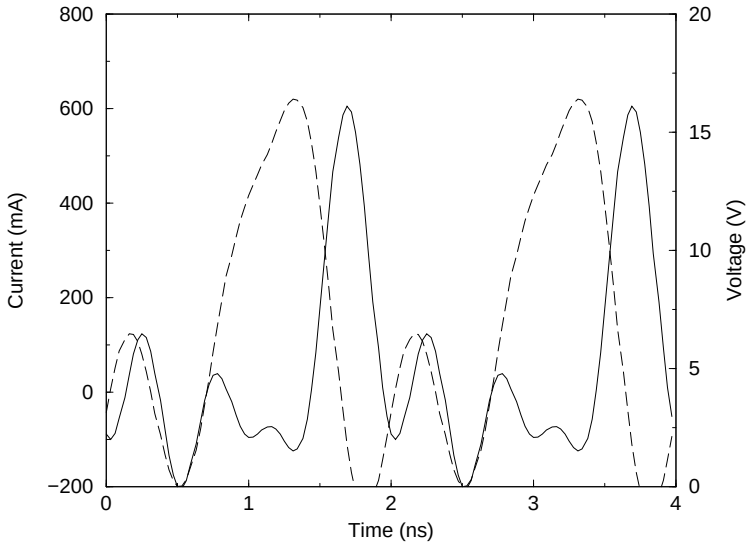


Figure 6.4. Simulated drain voltage (solid line) and current (dashed line) waveforms for the 1-GHz doubler.

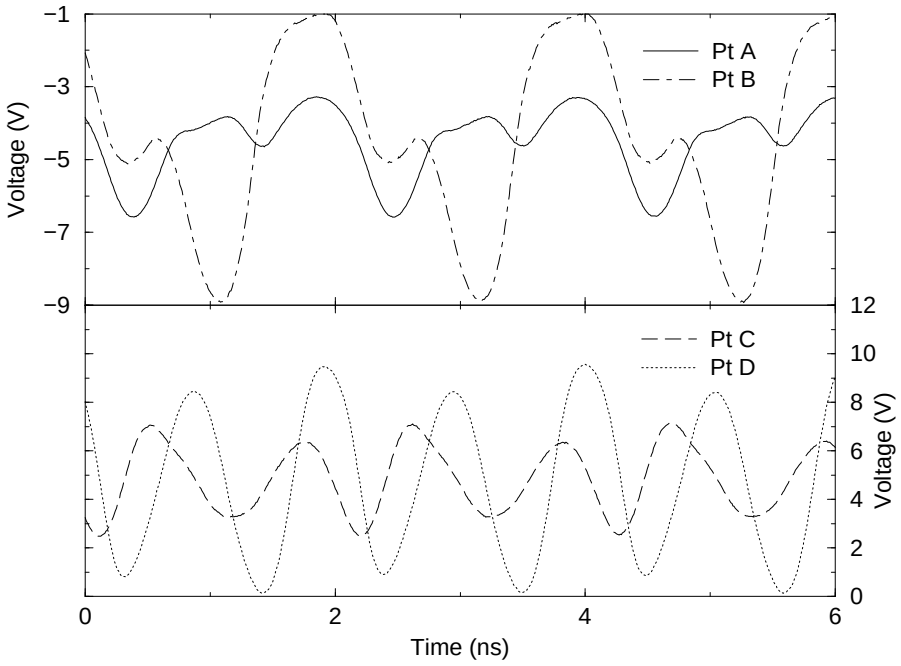


Figure 6.5. Measurements of the time-domain waveforms at points **A**-**D** in the 500 MHz to 1 GHz doubler.

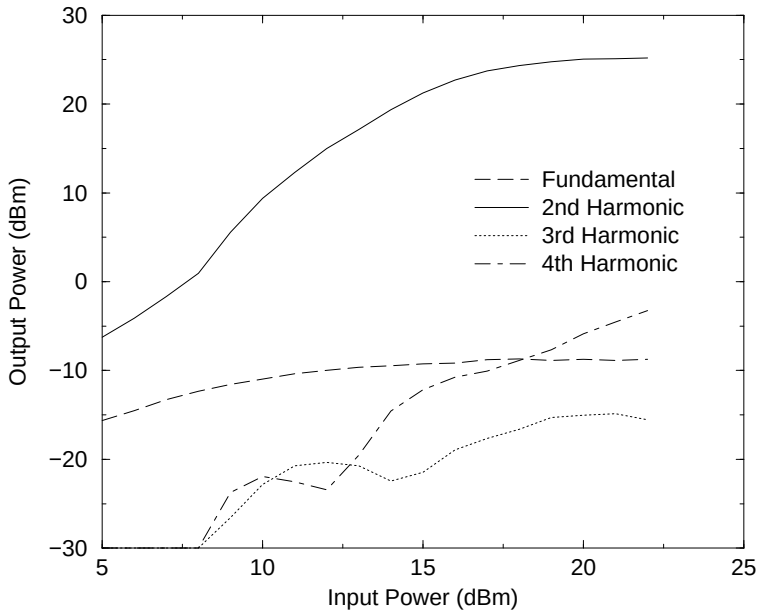


Figure 6.6. Measured output power at the fundamental (2.5 GHz) and first three harmonics versus input power for the 5-GHz doubler ($V_{DS}$=8 V and $I_{DS}$=100 mA).

### 6.4 5-GHz Doubler

A 5-GHz doubler was fabricated in microstrip using the Fujitsu FLK052WG MESFET ($C_{\rm ds}$=0.4 pF). Since frequency sweeps are provided for the 1-GHz doubler, power sweeps are given here for the 5-GHz doubler. Fig. 6.6 shows the output power versus input power at the fundamental and first three harmonics. Fig. 6.7 shows the drain, power-added, and overall efficiencies as a function of input power. A 2.5-GHz, 20-dBm input signal produced 330 mW output power with 5.2 dB conversion gain and 29% power-added efficiency at 5 GHz. For input powers greater than 15 dBm, the rejection of the unwanted frequencies is greater than 30 dB.

To perform the photoconductive waveform measurements, the doubler was tuned to 2.56 GHz-5.12 GHz. Fig. 6.8 shows the time-domain measurements of the 5-GHz doubler. At both input points, significant harmonic content is seen, showing the need for harmonic tuning at the input. At point **C**, fourth, sixth, and even eighth harmonics are seen in the waveform. With higher order harmonic tuning

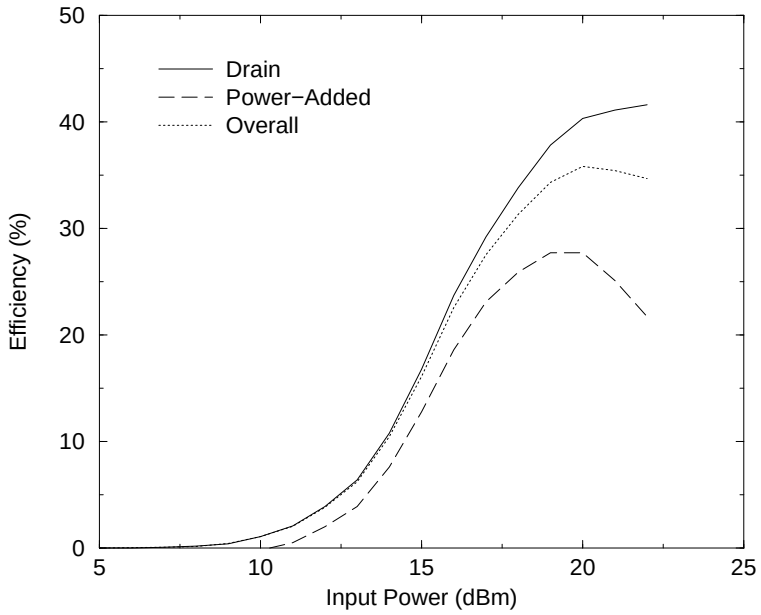


Figure 6.7. Measured second-harmonic (5.0 GHz) drain, power-added, and overall efficiencies versus input power for the 5-GHz doubler ($V_{DS}$=8 V and $I_{DS}$=100 mA). Efficiencies are defined in terms of output power at the second harmonic.

at the device output, class-E operation at the doubled frequency may indeed be approached. At point **D**, the waveform has cleaned up significantly.

This 5-GHz doubler exhibited similar properties as the 1-GHz doubler using a MESFET with a $f_T$ approximately 5 times higher. This shows that this concept can be scaled to millimeter-wave frequencies. For example, to make a 30-GHz doubler with similar capabilities, a HEMT with a $f_T$ in excess of 100 GHz should be used.

## 6.5 Conclusions

These results show that high-efficiency microwave doublers can be made by simply shorting the fundamental frequency at the output and presenting the class-E load impedance to the second harmonic. These FET multipliers can have good efficiency, power, and conversion gain. Using MESFETs or HEMTs with higher $f_T$s would allow this concept to be applied to millimeter-wave doublers.

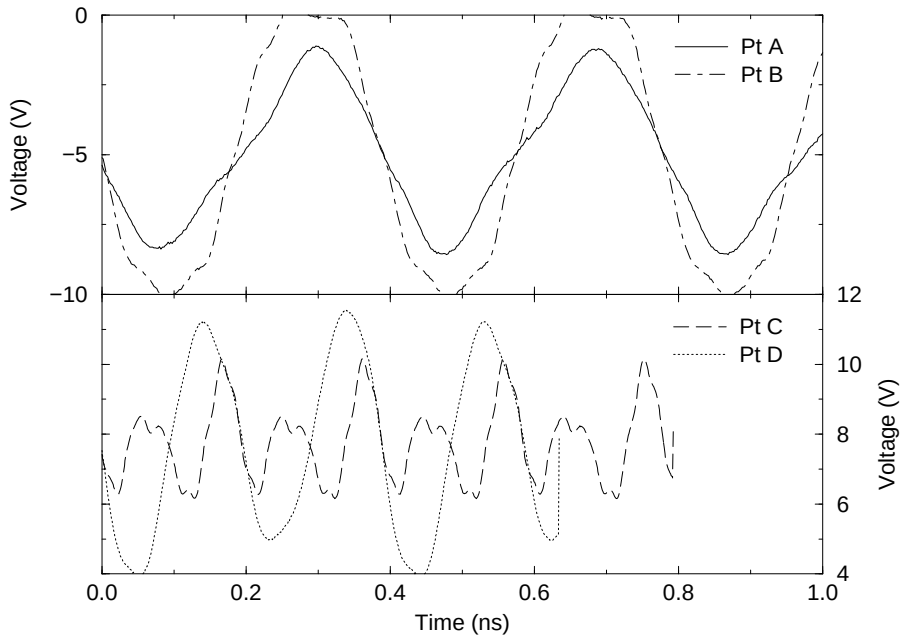


Figure 6.8. Measured time-domain waveforms at points **A**-**D** in the 2.5 GHz to 5.0 GHz doubler.

The photoconductive sampling waveform measurement technique is shown to be valuable for design and analysis of microwave frequency multipliers. By viewing the harmonic content in the time-domain waveforms, it can be seen at which points in the circuits further harmonic tuning should be applied.

# CHAPTER 7

# CONCLUSIONS AND FUTURE WORK

## 7.1 Conclusions

The main goal of this thesis has been to apply switched-mode power amplifier techniques to microwave frequenices. In addition to amplifiers, high-efficiency oscillators and multipliers were also designed and measured. Spatial power combining of high-efficiency microwave power amplifiers and oscillators was also investigated.

An overview of the different types of switched-mode power amplifiers was presented in chapter 2 along with their applicability to microwaves. Design examples at 0.5, 2.5, 8.0, and 10.0 GHz were presented with measurements for class-E and F amplifiers. The 500-MHz class-F amplifier gave 850 mW output power, 15.3 dB gain, and 75% power-added efficiency (PAE). The 8.4-GHz class-F amplifier gave 685 mW output power, 7.4 dB gain, and 59% PAE. This was compared to a 8.35-GHz class-E amplifier built using a four-times larger device. A two-stage 10-GHz class-E amplifier built using unpackaged chip MESFETs gave 210 mW output power, 13.2 dB gain, and 37% PAE.

A technique for measuring the waveforms at microwave frequencies using photoconductive sampling was described in chapter 3. This technique was used to measure waveforms of the 8-GHz class-E and F amplifiers. Measurements of the voltage waveform at the drain of the class-F amplifier showed an approximate square wave, confirming class-F operation. Voltage measurements at the drain of the class-E amplifier showed similar form to the ideal class-E waveform.

To achieve larger powers at microwave and millimter-wave frequencies, the powers of several transistors need to be efficiently combined. Chapter 4 investigated different approaches to this problem, with examples, converging on spatial power combining. Numerical comparisons are performed for the different methods. 9-element passive and active arrays operating at X band were designed, fabricated, and measured. A 36-element active array was also built and measured. The measured EIRP was 230 W and 2.63 kW for the 9-element and 36-element active arrays respectively. Based on the measured drop in combining efficiency from the 9-element to the 36-element combiner, it was shown that spatial power combining is an attractive option for combining hundreds of elements into a plane wave output.

Microwave switched-mode power amplifier design techniques can also be used for oscillator design. This was done in chapter 5. A 5-GHz class-E amplifier was converted into a 5-GHz class-E oscillator using a branch-line coupler and tunable delay line. This circuit produced 300 mW output power with 59% conversion efficiency when the bias is tuned for maximum efficiency and 600 mW with 48% conversion efficiency when biased for maximum power. A 4-element free-space oscillator array was also designed and built using global free-space feedback and produced 34.7 W EIRP. An equation was derived to calculate the efficiency of this oscillator array based on measured temperature change. Based on this calculation, the oscillator array gave 1.25 W output power with 40% conversion efficiency. This type of indirect efficiency measurement is useful in general for active antennas and arrays, where absolute radiated power is difficult to measure precisely and is usually estimated from the EIRP and pattern measurements.

In chapter 7, the class-E concept is applied to frequency doublers. Specifically, a 500 MHz to 1 GHz doubler and a 2.5 GHz to 5 GHz doubler were designed and built by shorting the fundamental frequency at the drain of the device and presenting the class-E load impedance to the second harmonic. The 1-GHz doubler produced

220 mW output power with 8.5 dB conversion gain and 35% power-added efficiency. The 5-GHz doubler produced 330 mW output power with 5.2 dB conversion gain and 29% power-added efficiency. Rejection of fundamental and unwanted harmonic frequency components was greater than 30 dB for both doublers. Photoconductive sampling of the time-domain waveforms was also performed in these multipliers and enabled the determination of how further harmonic tuning at the input and output could most improve performance.

## 7.2 Future Work

**7.2.1 Ka-Band Switched-Mode Circuits** Using the newest high-frequency HEMTs described in chapter 1, it would be possible to make high-efficiency switched-mode circuits like the ones presented in this thesis at freqeuncies up to and including Ka band (26-40 GHz). At these higher frequencies, much more care needs to be given to parasitics, substrate mode considerations, etc. If a device is used with a very high $f_{max}$ (>100 GHz), care needs to be taken to ensure stability in the entire range up to $f_{max}$, which is not trivial.

Regarding high-efficiency multipliers, it would be interesting to determine the cost savings, if any, when a low-frequency microwave oscillator is used and upconverted to millimeter-wave frequencies versus simply making an oscillator and power amplifier at the millimeter-wave output frequency.

**7.2.2 Mutual Coupling in Antenna Arrays** As described in chapter 4, mutual coupling of antenna elements in spatial power combining arrays can have significant effects. These effects are not fully understood and simulation tools require too much computing power to give insight presently. Several arrays should be built with varying spacing and the s-parameters and radiation patterns measured to give insight into the adjustments needed to make these arrays as efficienct as possible.

### 7.2.3 High-Efficiency Amplifiers for Digital Communications

Digital modulation schemes require linear as well as high-efficiency amplification. Digital signals have a broad distribution of power levels. As shown in the measurements in this thesis, class-E and class-F amplifiers only have high efficiencies when the amplifiers are heavily compressed. It is desired to have an amplifier that has high efficiency over a wide dynamic range. This can be done by using the fact that output power is dependent on drain bias. By lowering the drain bias, lower output power can be obtained with still high efficiency. This is the basis of the Kahn technique [69], where the envelope of the input signal is detected and used to control the drain bias. This technique has been applied up to L band [70]. It is possible to use these techniques with the X-band amplifiers described in this thesis.

BIBLIOGRAPHY


[1] R. A. York and Z. B. Popovic, eds., **Active and Quasi-Optical Arrays for Solid-State Power Combining**. New York: John Wiley, 1997.

[2] T. B. Mader and Z. B. Popović, "The transmission line class-e amplifier," **IEEE Microwave and Guided Wave Lett.**, vol. 5, pp. 290–292, Sept. 1995.

[3] T. B. Mader, E. Bryerton, M. Marković, M. Forman, and Z. B. Popović, "Switched-mode high-efficiency microwave power amplifiers in a free-space power-combiner array," **IEEE Trans. Microwave Theory Tech.**, vol. 46, pp. 1391–1398, Oct. 1998.

[4] T. B. Mader, **Quasi-Optical Class-E Power Amplifiers**. PhD thesis, Univ. of Colorado, Boulder, CO, 1995.

[5] H.-F. Chau, G. Wilcox, W. Chen, M. Tutt, and T. Henderson, "High-power high-efficiency X-band AlGaAs/GaAs heterojunction bipolar transistors with undercut collectors," **IEEE Microwave and Guided Wave Lett.**, vol. 7, pp. 288–290, Sept. 1997.

[6] K. Riepe, H. Leier, U. Seiler, A. Marten, and H. Sledzik, "High-efficiency GaInP/GaAs HBT MMIC power amplifier with up to 9 W output power at 10 GHz," **IEEE Microwave and Guided Wave Lett.**, vol. 6, pp. 22–24, Jan. 1996.

[7] R. S. Virk, M. Y. Chen, C. Nguyen, T. Liu, M. Matloubian, and D. B. Rensch, "A high-performance AlInAs/InGaAs/InP DHBT K-band power cell," **IEEE Microwave and Guided Wave Lett.**, vol. 7, pp. 323–325, Oct. 1997.

[8] H.-F. Chau, H.-Q. Tserng, and E. A. Beam, III, "Ka-band power performance of InP/InGaAs/InP double heterojunction bipolar transistors," **IEEE Microwave and Guided Wave Lett.**, vol. 6, pp. 129–131, Mar. 1996.

[9] M. Zaknoune, O. Schuler, S. Piotrowicz, F. Mollot, D. Theron, and Y. Crosnier, "High-power V-band $Ga_{0.51}In_{0.49}P/In_{0.2}Ga_{0.8}As$ pseudomorphic HEMT grown by gas source molecular beam epitaxy," **IEEE Microwave and Guided Wave Lett.**, vol. 9, pp. 28–30, Jan. 1999.

[10] S.-W. Chen, P. M. Smith, S.-M. J. Liu, W. F. Kopp, and T. J. Rogers, "A 60-GHz high-efficiency monolithic power amplifier using 0.1-$\mu$m PHEMTs," **IEEE Microwave and Guided Wave Lett.**, vol. 5, pp. 201–203, June 1995.

[11] Y. C. Chen, D. L. Ingram, R. Lai, M. Barsky, R. Grunbacher, T. Block, H. C. Yen, and D. C. Streit, "A 95-GHz InP HEMT MMIC amplifier with 427 mw power output," **IEEE Microwave and Guided Wave Lett.**, vol. 8, pp. 399–401, Nov. 1998.

[12] P. M. Smith, S.-M. J. Liu, M.-Y. Kao, P. Ho, S. C. Wang, K. H. G. Duh, S. T. Fu, and P. C. Chao, "W-band high efficiency InP-based power HEMT with 600 GHz $f_{max}$," **IEEE Microwave and Guided Wave Lett.**, vol. 5, pp. 230–232, July 1995.

[13] H. L. Krauss, C. W. Bostian, and F. H. Raab, **Solid-State Radio Engineering**. New York: Wiley, 1980.

[14] S.-A. El-Hamansy, "Design of high-efficiency rf class-d power amplifier," **IEEE Trans. Power Elect.**, vol. 9, pp. 297–308, May 1994.

[15] N. O. Sokal and A. D. Sokal, "Class e–a new class of high-efficiency tuned single-ended switching power amplifiers," **IEEE J. Solid-State Circuits**, vol. SC-10, pp. 168–176, June 1975.

[16] "High-efficiency tuned switching power amplifiers." U.S. Patent 3,919,656. Nov. 11, 1975.

[17] F. H. Raab, "Idealized operation of the class-e tuned power amplifier," **IEEE Trans. Circuits Syst.**, vol. CAS-24, pp. 725–735, Dec. 1977.

[18] F. H. Raab, "Effect of circuit variations on the class e tuned power amplifier," **IEEE J. Solid-State Circuits**, vol. SC-13, pp. 239–247, Apr. 1978.

[19] F. H. Raab, "Suboptimum operation of class-e power amplifiers," in **Proc. RF Technology Expo 89**, (Santa Clara, CA), pp. 85–98, Feb. 1989.

[20] M. K. Kazimierczuk and K. Puczko, "Exact analysis of class e tuned power amplifier at any q and switch duty cycle," **IEEE Trans. Circuits Syst.**, vol. CAS-34, pp. 149–159, Feb. 1987.

[21] G. H. Smith and R. E. Zulinski, "An exact analysis of class e amplifiers with finite dc-feed inductance at any output q," **IEEE Trans. Circuits Syst.**, vol. 37, pp. 530–534, Apr. 1990.

[22] B. Molnar, "Basic limitations of waveforms achievable in single-ended switching-mode (class e) power amplifiers," **IEEE J. Solid-State Circuits**, vol. SC-19, pp. 144–146, Feb. 1984.

[23] M. K. Kazimierczuk, "Generalization of conditions for 100-percent efficiency and nonzero output power in power amplifiers and frequency multipliers," **IEEE Trans. Circuits Syst.**, vol. CAS-33, pp. 805–807, Aug. 1986.

[24] V. J. Tyler, "A new high efficiency high power amplifier," **Marconi Rev.**, vol. 21, pp. 96–109, 1958.

[25] S. C. Cripps, "A theory for the prediction of gaas fet load-pull contours," in **1983 IEEE MTT-S Int. Microwave Symp. Dig.**, (Boston, MA), pp. 221–223, June 1983.

[26] S. C. Cripps, "Old-fashioned remedies for GaAsFET power amplifier designs," **IEEE MTT-S Newsletter**, pp. 13–17, summer 1991.

[27] A. Materka and T. Kacprzak, "Computer calculation of large-signal GaAs FET amplifier characteristics," **IEEE Trans. Microwave Theory Tech.**, vol. MTT-33, pp. 129–135, Feb. 1985.

[28] N. O. Sokal and R. Redl, "Power transistor output port model," **RF Design**, pp. 45–53, June 1987.

[29] E. W. Bryerton, M. D. Weiss, and Z. B. Popović, "A 10-ghz high-efficiency lens amplifier array," in **1998 IEEE MTT-S Int. Microwave Symp. Dig.**, (Baltimore, MD), pp. 1461–1464, June 1998.

[30] G. David, K. Yang, M. Crites, J. S. Rieh, L. H. Lu, P. Bhattacharaya, L. P. B. Katehi, and J. F. Whitaker, "Photoconductive probing and computer simulation of microwave potentials inside a SiGe MMIC," **Int. Topical Meeting on Silicon Monolithic Integrated Circuits in RF Systens, Ann Arbor**, Sept. 1998.

[31] G. Davis, T.-Y. Yun, M. H. Crites, J. F. Whitaker, T. R. Weatherford, K. Jobe, S. Meyer, M. Bustamante, B. Goyette, S. T. III, and K. R. Elliot, "Absolute potential measurements inside microwave digital ICs using a micromachined photoconductive sampling probe," **IEEE Trans. Microwave Theory Tech.**, vol. 46, pp. 2330–2337, Dec. 1998.

[32] J. F. Whitaker, personal communication.

[33] K. J. Russell, "Microwave power combining techniques," **IEEE Trans. Microwave Theory Tech.**, vol. MTT-27, pp. 472–478, May 1979.

[34] "Microwave semiconductor databook." Fujitsu, 1995. pp. 34-39.

[35] D. Staiman, M. E. Breese, and W. T. Patton, "New technique for combining solid-state sources," **IEEE J. Solid-State Circuits**, vol. SC-3, pp. 238–243, Sept. 1968.

[36] N.-S. Cheng, A. Alexanian, M. G. Case, and R. A. York, "20 watt spatial power combiner in waveguide," in **1998 IEEE MTT-S Int. Microwave Symp. Dig.**, (Baltimore, MD), pp. 1457–1460, June 1998.

[37] M. Forman, T. Marshall, and Z. Popović, "Two ka-band quasi-optical amplifier arrays," in **1999 IEEE MTT-S Int. Microwave Symp. Dig.**, (Anaheim, CA), June 1999. in press.

[38] E. A. Sovero, J. B. Hacker, J. A. Higgins, D. S. Deakin, and A. L. Sailer, "A ka-band monolithic quasi-optic amplifier," in **1998 IEEE MTT-S Int. Microwave Symp. Dig.**, (Baltimore, MD), pp. 1453–1456, 1998.

[39] J. T. Delisle, M. A. Gouker, and S. M. Duffy, "45-ghz mmic power combining using a circuit-fed, soatially combined array," **IEEE Microwave and Guided Wave Lett.**, vol. 7, pp. 15–17, Jan. 1997.

[40] M. Gouker, "Toward standard figures-of-merit for spatial and quasi-optical power-combined arrays," **IEEE Trans. Microwave Theory Tech.**, vol. 43, pp. 1614–1617, July 1995.

[41] T. Mader, J. Schoenberg, L. Harmon, and Z. Popović, "Planar MESFET transmission wave amplifier," **IEE Electronic Letters**, vol. 28, pp. 1699–1701, Sept. 1993.

[42] N. Sheth, T. Ivanov, A. Balasubramaniyan, and A. Mortazawi, "A nine HEMT spatial amplifier," in **1994 IEEE MTT-S Int. Microwave Symp. Dig.**, (San Diego, CA), pp. 1239–1242, June 1994.

[43] M. Kim, E. A. Sovero, J. B. Hacker, M. P. De Lisio, J.-C. Chiao, S.-J. Li, D. R. Gagnon, J. J. Rosenberg, and D. B. Rutledge, "A 100-element HBT grid amplifier," **IEEE Trans. Microwave Theory Tech.**, vol. 41, pp. 1762–1771, Oct. 1993.

[44] M. A. Ali, S. C. Ortiz, T. Ivanov, and A. Mortazawi, "Analaysis and measurement of hard-horn feeds for the excitation of quasi-optical amplifiers," **IEEE Trans. Microwave Theory Tech.**, vol. 47, pp. 479–487, Apr. 1999.

[45] T. Ivanov, S. O. A. Mortazawi, E. Schlecht, and J. Hubert, "A passive double-layer microstrip array for the construction of millimeter-wave spatial power combining amplifiers," **IEEE Microwave and Guided Wave Lett.**, vol. 7, pp. 365–367, Nov. 1997.

[46] W. Rotman and R. Turner, "Wide angle microwave lens for line source applications," **IEEE Trans. Ant. and Prop.**, vol. 11, pp. 623–632, Nov. 1963.

[47] D. T. McGrath, "Planar three-dimensional constrained lenses," **IEEE Trans. Ant. and Prop.**, vol. 34, pp. 46–50, Jan. 1986.

[48] J. S. H. Schoenberg, **Quasi-Optical Constrained Lens Amplifiers**. PhD thesis, Univ. of Colorado, Boulder, CO, 1995.

[49] S. Hollung, **Quasi-optical transmit/receive lens amplifier arrays**. PhD thesis, Univ. of Colorado, Boulder, CO, 1998.

[50] Y. Y. Hu, "A method of determining phase centers and its application to electromagnetic horns," **Journal of the Franklin Institute**, vol. 271, pp. 31–39, Jan. 1961.

[51] J. Schoenberg, T. Mader, B. Shaw, and Z. B. Popović, "Quasi-optical antenna array amplifiers," in **1995 IEEE MTT-S Int. Microwave Symp. Dig.**, (Orlando, FL), pp. 605–608, May 1995.

[52] W. A. Shiroma, E. W. Bryerton, S. Hollung, and Z. B. Popović, "A quasi-optical receiver with angle diversity," in **1996 IEEE MTT-S Int. Microwave Symp. Dig.**, (San Francisco, CA), pp. 1131–1134, June 1996.

[53] S. Hollung, A. E. Cox, and Z. B. Popović, "A bi-directional quasi-optical lens amplifier," **IEEE Trans. Microwave Theory Tech.**, vol. 45, pp. 2352–2357, Dec. 1997.

[54] M. Prigent, M. Camiade, G. Pataut, D. Reffet, J. M. Nebus, and J. Obregon, "High efficiency free running class f oscillator," in **1995 IEEE MTT-S Int. Microwave Symp. Dig.**, (Orlando, FL), pp. 1317–1320, May 1995.

[55] J. O. McSpadden, L. Fan, and K. Chang, "High-efficiency Ku-band oscillators," **IEEE Trans. Microwave Theory Tech.**, vol. 46, pp. 1566–1571, Oct. 1998.

[56] E. W. Bryerton, W. A. Shiroma, and Z. B. Popović, "A high-efficiency class-E oscillator," **IEEE Microwave and Guided Wave Lett.**, vol. 6, pp. 441–443, Dec. 1996.

[57] W. A. Shiroma, E. W. Bryerton, and Z. Popović, "Analysis and design of oscillator grids and arrays," in **Analysis and Design of Integrated Circuit-Antenna Modules** (K. C. Gupta and P. Hall, eds.), ch. 8, Wiley, 1999. in press.

[58] R. D. Martinez and R. C. Compton, "A general approach for the *s*-parameter design of oscillators with 1 and 2-port active devices," **IEEE Trans. Microwave Theory Tech.**, vol. 40, pp. 569–574, Mar. 1992.

[59] K. M. Johnson, "Large signal GaAs MESFET oscillator design," **IEEE Trans. Microwave Theory Tech.**, vol. MTT-27, pp. 217–227, Mar. 1979.

[60] M. Kim, E. A. Sovero, J. B. Hacker, M. P. De Lisio, J. J. Rosenberg, and D. B. Rutledge, "A 6.5–11.5 GHz source using a grid amplifier with a twist reflector," **IEEE Trans. Microwave Theory Tech.**, vol. 41, pp. 1772–1774, Oct. 1993.

[61] M. Funabashi, T. Inoue, K. Ohata, K. Maruhashi, K. Hosoya, M. Kuzuhara, K. Karekawa, and Y. Kobayashi, "A 60-GHz MMIC stabilized frequency source composed of a 30-GHz DRO and a doubler," in **1995 IEEE MTT-S Int. Microwave Symp. Dig.**, (Orlando, FL), pp. 71–74, May 1995.

[62] Millimeter-wave opportunities for automotive and radio applications," workshop at *IEEE MTT-S Int. Microwave Symp.*, Denver, CO, June 1997.

[63] T. Saito, T. Ninomiya, O. Isaji, T. Watanabe, H. Suzuki, and N. Okubu, "Automotive FM-CW radar with heterodyne receiver," **IEICE Trans Commun.**, vol. E79-B, pp. 1806–1812, Dec. 1996.

[64] R. E. Zulinski and J. W. Steadman, "Idealized operation of class-e frequency multipliers," **IEEE Trans. Circuits Syst.**, vol. CAS-33, pp. 1209–1218, Dec. 1986.

[65] D. Thomas, Jr. and G. R. Branner, "Optimization of active microwave frequency multiplier performance utilizing harmonic terminating impedances," in **1996 IEEE MTT-S Int. Microwave Symp. Dig.**, (San Francisco, CA), pp. 659–662, June 1996.

[66] H. J. D. L. Santos, D. D. Nardi, K. L. Hargrove, M. Hafizi, and W. E. Stanchina, "High-efficiency InP-based DHBT active frequency multipliers for wireless communications," **IEEE Trans. Microwave Theory Tech.**, vol. 44, pp. 1165–1167, July 1996.

[67] S. A. Maas, **Nonlinear Microwave Circuits**, ch. 10. IEEE Press, 1997.

[68] C. Rauscher, "High-frequency doubler operation of GaAs field-effect transistors," **IEEE Trans. Microwave Theory Tech.**, vol. MTT-31, pp. 462–473, June 1983.

[69] L. R. Kahn, "Single sideband transmission by envelope elimination and restoration," **Proc. IRE**, vol. 40, pp. 803–806, July 1952.

[70] F. H. Raab, B. E. Sigmon, R. G. Myers, and R. M. Jackson, "L-band transmitter using Kahn EER technique," **IEEE Trans. Microwave Theory Tech.**, vol. 46, pp. 2220–2225, Dec. 1998.